Layered double hydroxides and their derived functional nanomaterials for sustainable energy applications

Thesis Submitted to AcSIR

For the Award of the Degree of

DOCTOR OF PHILOSOPHY

in

CHEMICAL SCIENCES

By

Nadeema Ayasha

Registration No. **10CC15J26014**

Under the guidance of

Dr. Sreekumar Kurungot

CSIR-National Chemical Laboratory (CSIR-NCL)

Pune-411008, INDIA.

October 2019

CERTIFICATE

This is to certify that the work incorporated in this Ph.D. thesis entitled **"Layered double hydroxides and their derived functional nanomaterials for sustainable energy applications"** submitted by **Ms. Nadeema Ayasha** to Academy of Scientific and Innovative Research (AcSIR) in fulfillment of the requirements for the award of the Degree of the ***Doctor of Philosophy***, embodies original research work under my supervision at the Physical and Materials Chemistry Division, CSIR-National Chemical Laboratory, Pune-411008, India. I further certify that this work has not been submitted to any other University or Institution in part or full for the award of any degree or diploma. Research material obtained from other sources has been duly acknowledged in the thesis. Any text, illustration, table etc., used in the thesis from other sources, have been duly cited and acknowledged.

It is also certified that this work done by the student, under my supervision, is plagiarism free.

Nadeema Ayasha

(Research Student)

(Reg. No. **10CC15J26014**)

Dr. Sreekumar Kurungot

(Research Supervisor)

Date: 24|10|19

Place: CSIR-NCL, Pune.

DECLARATION

I hereby declare that all the research work embodied in this thesis entitled **"Layered double hydroxides and their derived functional nanomaterials for sustainable energy applications"** submitted to the Academy of Scientific and Innovative Research (AcSIR), New Delhi, for the award of degree of **Doctor of Philosophy** in **Chemical Sciences** is the outcome of experimental investigations carried out by me under the supervision of **Dr. Sreekumar Kurungot**, Principal Scientist, CSIR-National Chemical Laboratory, Pune-411008, India. I affirm that the work incorporated is original and has not been submitted to any other academy, university or institution in part or full for the award of any degree or diploma.

Date: 24/10/19

Nadeema Ayasha

Physical and Materials Chemistry Division

CSIR-National Chemical Laboratory

Pune-411008, India

This dissertation is

dedicated to

My father

Late Mohd. Aslam

Acknowledgment

Ph.D. is like a long journey; a unique experience that takes you through the untraversed path, to conquer the final goal fixed in mind. One can't succeed in this journey without the guidance and support of the research supervisor, friends, and well-wishers. At this juncture of my doctorate, I would like to express my sincere gratitude to everyone who has helped and supported me throughout my research journey directly or indirectly.

The foremost person who comes to my mind while writing this acknowledgment is my father. I was nothing today without his love and support. His joy and proud of my every small success gave me the reason to chase my dreams. There are no words that can explain how grateful it is to be his daughter. I owe everything to him. Moreover, my family is always a source of inspiration and great moral support for me in pursuing my education. I owe a lot to my beloved family, who encouraged and helped me at every stage of my personal and academic life and longed to see this achievement come true. From the bottom of my heart, I feel thankful to my grandparents who always appreciated my small and big accomplishments.

I express my deep and sincere gratitude to my thesis advisor, **Dr. Sreekumar Kurungot***, who has had the patience to allow me my space but the prescience to press me when necessary. He has taught me a lot, not only in the research field but also about living a well-balanced life. I could never wish for a better supervisor. His positive criticism has immensely helped me to improve myself in the professional sphere. I also thank him for providing all the essential research facilities which were necessary for my doctoral work.*

I am grateful to **Prof. A. K. Nangia** *(Director, CSIR-NCL),* **Prof. V. K. Pillai** *and* **Prof. S. Pal** *(Former Directors, CSIR-NCL),* **Dr. Anil Kumar** *(Former Head, Physical and Materials Chemistry Division) and* **Dr. P. A. Joy** *(Head, Physical and Materials Chemistry Division) for giving me this opportunity and providing all necessary infrastructure and facilities to carry out my research work. I would like to acknowledge all the support from the office staff of Physical and Materials Chemistry Division. I am also highly thankful to UGC, New Delhi, India, for the financial assistance.*

I wish to express my sincere thanks to the Doctoral Advisory Committee members, **Dr. Mahesh Kulkarni***,* **Dr. Ulhas K. Kharul** *and* **Dr. Pankaj Poddar***, for providing me their valuable time, suggestions and encouragement throughout my Ph.D. tenure. A special thanks to Dr. Pankaj*

Poddar for providing his invaluable suggestions on every single presentation slide which has helped me to gain knowledge in a broader context. I also feel privileged to have my DAC members like Dr. Kharul, who always notice and encourage my small efforts and achievements.

My senior, Dr. Vishal M. Dhavale needs a special mention. His mentorship at the beginning of my doctorate has indeed helped me to learn and understand my research work. He was the person who taught me the handling of various experimental instruments, techniques, and softwares. I cherish his brotherly behavior inside and outside the lab, which helped me a lot in adjusting in a new state and atmosphere. I thank him for all of it.

I believe this is the appropriate occasion to show my gratefulness to my teachers, Mr. Ashish Srivastava, Mr. Manoj Mishra, Dr. Awasthy, Dr. Sheila Srivastava, Dr. Shobha, Dr. Anita Rai, Dr. Gurmeet Singh and Dr. Joseph Daniel who always encouraged and made me believe in myself to reach here from my HSC to B.Sc. to M.Sc. Here, I would like to specially mention Dr. Gurmeet, who was always my friend-cum teacher and helped me in every possible way to reach NCL and peruse my dream.

I thank and appreciate my seniors Dr. Palaniselvam, Dr. Sreekuttan, Dr. Bihag, Mr. Pandiraj, Dr. Harshitha, Dr. Santosh Singh, Dr. Roby Sony and Dr. Varchaswal Kashyap for always providing me supportive and friendly environment. My colleagues Vidyanand V., Pranav K.G., Rajith I.V., Siddheshwar Bhange, Meena Ghosh, Sachin Kumar, Narugopal Manna, Geeta Kharabe, Swati Dilwale, and Ajmal for their support during my Ph.D. tenure. I also would like to thank the Post Doctorates Dr. Raji, Dr. Gourav Singla, Dr. Debashree Das, and Dr. Shilpa for sharing their experiences which helped me directly or indirectly to shape my research carrier. I would also like to mention Rakhshitha and Dibya Prakash, who carried out their internship under my guidance and helped me in completing a few of my research projects.

During my stay at NCL, I, fortunately, met a few wonderful and cheerful people who later became good friends where Dr. Sandeep Yadav needs a special mention. He was just like a God-gift for me and helped me in all my personal and professional ups and downs. Without him, my life at NCL would have been tasteless. I feel very lucky to find a person like him, who made me passionate for my research as well as personal life. I also express my heartiest gratitude to Dr. Ashwini, Indrapal, Vedi, Mukta, Divya, Pankaj, Umesh, Aslam, Karthika, Smita, Apoorva, Ishwari, Debopriya, Preeti, Gargi and Sanjukta for making my life easy and joyful at NCL. I especially want to thank Pankaj for always helping me during TEM analysis. I

also want to thank my old friends Manish, Narendra, Neeraj, Aman, Aakanksha, Alankrita, Geetanjali, and Aakriti for always being my well-wishers.

I am also grateful to Dr. Guruswamy and Arun Toris for providing me the access to WAXD, which helped me a lot to analyze my samples, hence in the smooth running of my research at NCL. I also want to express my gratitude to Dr. C. P. Vinod, Dr. Arun Venkatnathan (IISER Pune) and Dr. Vaidhyanathan Ramanathan (IISER Pune) for providing their valuable time to evaluate my work during fellowship upgradations.

I am profoundly thankful to the Student Academic Office staff, Chairman Dr. B. L. V. Prasad, AcSIR Chairman Dr. Sunil Joshi, Ms. Purnima Kohle, Mr. P. V. Iyer, Mr. P. K. Purushothaman, Ms. Vaishali, and Ms. Komal for their prompt processing of the documents.

Last but not least, I wish to thank the great scientific community whose achievements are a constant source of inspiration for me. Above all, I extend my gratitude to the Almighty for giving me the wisdom, health, and strength to undertake this research work and enabling me to its completion.

Nadeema Ayasha

List of Abbreviations

Abbreviation	Expansion
GMST	Global mean surface temperature
IPCC	Intergovernmental panel on climate change
GHG	Greenhouse gas
LDH	Layered Double Hydroxide
OER	Oxygen evolution reaction
HER	Hydrogen evolution reaction
ZAB	Zinc-air battery
PEM	Proton exchange membrane
AEM	Anion exchange membrane
MOOH	Metal oxyhydroxide
PGM	Precious group metal
Non-PGM	Non-precious group metal
2D	Two-dimensional
GO	Graphene oxide
rGO	Reduced-graphene oxide
NGr/NG	Nitrogen-doped graphene
CNT	Carbon nanotube
MWCNT	Multi-walled carbon nanotube
CQD	Carbon quantum dot
NF	Nickel foam

TMPs	Transition metal phosphides
TMNs	Transition metal nitrides
TMDs	Transition metal dichalcogenides
WOR	Water oxidation reaction
ORR	Oxygen reduction reaction
CO_2RR	Carbon dioxide reduction reaction
WOEs	Water oxidation electrocatalysts
BET	Brunauer-Emmett-Teller
PXRD	Powder X-ray diffraction
WAXD	Wide-angle X-ray diffraction
TGA	Thermo-gravimetric analysis
FESEM	Field-emission scanning electron microscopy
TEM	Transmission electron microscopy
SAED	Selected area electron diffraction pattern
XPS	X-ray photoelectron microscopy
C_{dl}	Double layer capacitance
RF	Roughness factor
ECSA	Electrochemical surface area
CV	Cyclic voltammetry
LSV	Linear sweep voltammetry
CA	Chronoamperometry
RDE	Rotating disc electrode
RRDE	Rotating ring disc electrode

RHE	Reversible hydrogen electrode
R_{ct}	Charge transfer resistance
UOR	Urea oxidation reaction
ATTM	Ammonium tetrathiomolybdate
FTIR	Fourier-transform infrared spectroscopy
HAADF-STEM	High-angle annular dark-field-scanning transmission electron microscopy
EDS	Energy-dispersive X-ray spectroscopy
CP	Chronopotentiometry
OCV	Open circuit voltage

Table of Contents

Preface

Chapter 1

Electrocatalytic Hydrogen Generation: From Layered double Hydroxide Tuning to Deployment for Hydrogen Generation Applications

Chapter 2

ϒ-NiOOH-Enriched NiZn Double Hydroxide Nanosheets/Nitrogen-Doped Graphene Composite for Catalyzing the Water Oxidation Half-Cell

Chapter 3

NiZn Double Hydroxide-Derived Nickel Selenide/Nitrogen Doped Graphene Composite to Catalyze the Overall Water Electrolysis

3.1: Introduction

3.2. Experimental section

3.2.1. Synthesis of graphene oxide (GO) and nitrogen-doped graphene (NGr)

3.2.2. Synthesis of ZnNi-LDH/NGr

3.2.3. Conversion of ZnNi/NGr to porous β-Ni(OH)$_2$/NGr

3.2.4. Conversion of porous β-Ni(OH)$_2$/NGr to porous NiSe/NGr

3.2.5. Synthesis of α-Ni(OH)$_x$/NGr

3.2.6. Conversion of α-Ni(OH)$_x$/NGr to β-Ni(OH)$_2$/NGr and its selenization

3.2.7. Direct conversion of ZnNi-LDH/NGr to ZnNiSe/NGr

3.3. Results and Discussion

3.3.1. Structure and morphology of the catalyst

3.3.1.1. X-ray diffraction analysis

3.3.1.2. Brunauer-Emmett-Teller (BET) analysis

3.3.1.3. Thermo-gravimetric analysis

3.3.1.4. Raman analysis

3.3.1.5. Field-emission scanning electron microscopy analysis

3.3.1.6. Transmission electron microscopy analysis

3.3.1.7. X-ray photoelectron spectroscopy analysis

3.3.2. Electrochemical analysis

3.3.2.1. Electrocatalytic performance towards water oxidation

Chapter 4

$[MoS_4]^{2-}$-Intercalated NiCo Layered Double Hydroxide Nanospikes/Ni Foam to Generate Cheaper H_2 Directly from Urea-Rich Wastewater

Chapter 5

Co@CoAl-LDH/NG Composite-Catalyzed Dual-Mode Al-Based Battery for Simultaneous H_2 Production and Electricity Generation

Chapter 6

Preface

This thesis deals with the synthesis of layered double hydroxide-based functional nanomaterials for their applications in electrochemical hydrogen generation *via* water splitting. Water electrolysis involves two half-cell reactions, where, on one electrode, water gets oxidized, and on the other electrode, it gets reduced to liberate H_2. The two half-cell reactions are kinetically sluggish and require robust catalysts to overall improve the energy-efficiency of hydrogen generation. The present thesis is an effort to contribute in this field and the work components are illustrated in six chapters. The first chapter introduces the evolution and importance of layered double hydroxide (LDH) chemistry toward catalyzing various electrochemical reactions with a special emphasis on catalyzing water electrolysis. It also comprises the importance and current scenario of hydrogen economy. Second to fifth chapters are working chapters narrating our approach to the synthesis and property tuning of LDH toward catalyzing various electrochemical reactions involved in cost-effective hydrogen generation. The working chapters are broadly categorized in two sections. The first section comprises initial two working chapters with the special focus on the replacement of noble-metal-based water electrolyzing catalysts with low-cost, earth abundant metals-based robust catalyst systems. The major outcome of these two chapters is to contribute toward reducing the H_2-generating station installation cost. The other two working chapters build another section which focuses to reduce the energy expense for generating hydrogen from water by replacing the water oxidation half-cell with readily oxidizable species. The last chapter of the thesis includes the summery of the research work performed in the above-mentioned four working chapters along with the future outline.

Chapter 1 first introduces the current energy scenario and need of the alternate energy resources. Subsequently, it describes the current status of hydrogen economy including the major sources of hydrogen production, their limitations and environmental impact. Followed by this, the chapter gives a brief discussion on the alternate and environmentally safer ways of hydrogen generation, where, one of the promising sources is found to be water. Hence, the working principle of water splitting along with its various types is briefly introduced. In the next section, special focus has been directed toward electrochemical water splitting owing to its superiorities over the other water splitting pathways. A good deal of importance is given toward improving

the overall energy-efficiency of hydrogen generation. One of the major focuses of this thesis is to contribute toward reducing the capital cost of water-sourced hydrogen generation. This includes the replacement of the state-of-art scarce-metal-based catalysts with low-cost robust catalysts as well the replacement of the energy-uphill water oxidation half-cell with readily oxidizable species such as urea, alcohols and electropositive metals. This introductory chapter also illuminates on our interesting work on the simultaneous hydrogen generation and electricity production. In the next section, a special focus toward the current status of electrocatalyst designing as well as the future prospects is discussed. In the area of electrocatalyst development, this thesis focusses on the property tuning of LDH toward electrochemical hydrogen generation. Hence, a good number of recent works on property tuning of LDH toward designing multifunctional electrocatalytic materials are briefly discussed. Finally, this chapter ends with a discussion on the scope and objectives of this dissertation.

Chapter 2 focuses only on catalyzing the water oxidation half-cell since the overall energy efficiency of water-sourced H_2 generation is controlled by this half-cell. With this work, our aim is to replace the high-cost, scarce-metal-based catalysts with readily available active metals. The work discusses a single-step solvothermal process to synthesize an active electrocatalyst for water oxidation (WOR) in alkaline medium. The adopted synthesis strategy results into the anchoring of ϒ-NiOOH phase-enriched NiZn double hydroxide nanosheets over N-doped graphene. The designed catalyst possesses thin, porous and open layered structure, which makes the system more efficient and accessible for the better water oxidation potential. Moreover, we experimentally demonstrated that the incorporation of Zn provides an easy approach to get plenty of exposed ϒ-NiOOH phase to make the system more viable for WOR with a small overpotential of ~290 mV at 10 mA cm^{-2} and a Tafel slope of ~44 mV decade^{-1}. In addition to that, the oxophilic nature of Zn assisted to improve the long-term stability of the catalyst system.

Chapter 3 illustrates our work targeted to reducing the electrolyzer installation cost both by utilizing low-cost active metals as well as by eliminating the cost of designing two different materials. The work introduces a self-templating method for the design of porous, edge-site-rich hybrid nanomaterial *via* the selective etching of the layered double hydroxide precursors that contain an amphoteric metal by alkali treatment followed by the vapor phase selenization. The

obtained hexagonal nickel selenide nanoplates anchored over nitrogen-doped graphene showed highly efficient and robust WOR electrocatalysis. It demonstrates a low overpotential of ~311 mV to achieve the benchmark 10 mA cm^{-2} water oxidation current density in 1 M KOH. When we fabricated an alkaline water electrolyzer, it enabled high-performing overall water splitting with a low overpotential of 460 mV from the theoretical voltage of 1.23 V to generate sufficient amounts of H$_2$ and O$_2$ by achieving a current density of 10 mA cm^{-2}. The catalyst has also displayed outstanding electrochemical stability toward all the employed reactions.

With **Chapter 4**, our aim is to further reduce the required energy for the H$_2$ generation from water, and hence to contribute toward reducing the per kg H$_2$ cost. This chapter describes a strategy of substituting the energy-uphill water oxidation half-cell with readily oxidizable urea-rich urine to construct a ground-breaking bridge, combining the energy-efficient hydrogen generation and environmental protection. Designing of a robust multifunctional electrocatalyst is desirable for the widespread implementation of this waste to fuel technology. In this context, here, we propose a simple tuning of the electrocatalytically favorable characteristics of NiCo layered double hydroxide by introducing [MoS$_4$]$^{2-}$ in its interlayer space. The [MoS$_4$]$^{2-}$ insertion as well as its effect on the electronic structure tuning is thoroughly studied *via* X-ray photoelectron spectroscopy in combination with electrochemical analysis. This insertion induces overall electronic structure tuning of the hydroxide layer in such a way that, the designed catalyst exhibits favorable kinetics toward all the required reactions of hydrogen generation. That is why, our homemade catalyst, when utilized both as a cathode and anode to fabricate a urea electrolyzer, it requires a mere ~1.37 V cell potential to generate sufficient H$_2$ by reaching the benchmark current density of 10 mA cm^{-2} in 1 M KOH/0.33 M urea along with long-lasting catalytic efficiency. Other indispensable reason of selecting [MoS$_4$]$^{2-}$ is its high-valent nature making the catalyst highly selective and insensitive to common catalyst-poisoning toxins of urine. This is experimentally supported by performing the real urine electrolysis, where the nanospike-covered Ni foam-based catalyst shows similar performance to that of synthetic urea, offering its industrial value.

Chapter 5 aims to not only to replace the energy-consuming water oxidation with readily oxidizable metal but also to generate electricity. The motivation of this work was originated

while testing a home-made metal-air battery which involves the oxidation of an electropositive metal on the anode and reduction of O_2 from air on the cathode. The cell thus theoretically generates 2.71 V. While performing the test, accidently we pumped N_2 in place of O_2, and found that even in absence of O_2, the circuit is completed and some voltage is generating. And, with the support of literatures as well as experiments, we found that, in absence of O_2, water gets reduced and liberates H_2. Hence, in this chapter, we propose the fabrication and demonstration of a dual-mode Al-based battery to generate H_2 and electricity simultaneously. However, to improve the overall energy-efficiency of the device, development of a robust bifunctional catalyst is required, which can catalyze both O_2 reduction reaction (ORR) as well as H_2O reduction (hydrogen evolution reaction, HER). Taking this into account, here we tuned the physicochemical LDH property and synthesized a bifunctional Co@CoAl-LDH/NG electrocatalyst to catalyze both ORR and HER. The designed catalyst was characterized properly by employing various material characterization techniques, *e.g.,* X-ray diffraction analysis, high-resolution transmission electron microscopy, X-ray photoelectron spectroscopy, etc. The homemade catalyst when employed as the cathode both in the presence and absence of O_2, it worked quite efficiently and performed comparable to the similar devices based on the commercial Pt-based catalyst. At a discharge current density of 5 mA cm^{-2}, the catalyst exhibited an average voltage of ~0.95 V both in the presence and absence of O_2, respectively. The H_2 generated was quantified with gas chromatography.

Finally, **Chapter 6** summarizes the significant observations and outcomes of each working chapter of the present thesis. The chapter starts with a brief introductory paragraph of the work focus along with the strategy which we have adopted to align all the working chapters. Afterward, a brief overview and key points of all the working chapters are summed up one by one. The last part is dedicated to the future scope of the ideas and approaches adopted in this dissertation toward the other electrochemical systems, for example, batteries and fuel cells.

Chapter 1

Electrocatalytic Hydrogen Generation: From Layered Double Hydroxide Property Tuning to Deployment for Hydrogen Generation Applications

This thesis deals with the synthesis and property tuning of layered double hydroxide-based functional nanomaterials for their applications in electrochemical hydrogen generation *via* water splitting. Water electrolysis involves two half-cell reactions, where on one electrode water gets oxidized and on the other electrode it gets reduced to liberate H_2. The two half-cell reactions are kinetically sluggish and require robust catalysts to reduce the overall energy required for hydrogen generation. The present thesis is an effort to contribute in this field and the work components are illustrated in six chapters. The first chapter introduces the evolution and importance of layered double hydroxide (LDH) chemistry toward catalysing various electrochemical reactions with a special emphasis on catalysing the reactions involved in electrochemical hydrogen generation. It also comprises the importance and current scenario of hydrogen economy. Second to fifth chapters are working chapters narrating our approach to the synthesis and property tuning of LDHs toward catalysing various electrochemical reactions involved in cost-effective hydrogen generation. The working chapters are broadly categorized in two sections. The first section comprises initial two working chapters with the special focus on the replacement of noble-metal-based water electrolyzing catalysts with low-cost, earth abundant metals-based robust catalyst systems. The major outcome of these two chapters is to contribute toward reducing the H_2-generating station installation cost. The other two working chapters build another section which focuses to reduce the energy expense for generating hydrogen from water by replacing the water oxidation half-cell with readily oxidizable species. The last chapter of the thesis includes the summery of research work performed in the above-mentioned four working chapters along with the future outline.

1.1. Problem statement

The industrial revolution began in the latter half of the 18th century and triggered enormous goods and machine manufacturing.[1,2] This revolution also involved the use of new energy sources such as coal, the steam engine, petroleum and the internal-combustion engines.[3] Starting from the 19th century, fossil fuel, mainly coal and petroleum became the major source of energy generation and have been continuously burnt to release the stored energy for various purposes ranging from electricity generation to transportation to industrial and household purposes.[1] During the combustion process, fossil fuel releases a variety of toxic particulates and emissions including carbon dioxide, nitrogen oxides, sulphur dioxides, etc.[1] These emissions have caused severe environmental and health risks through acid rain, smog, poor air quality, and global warming.[4] Among which, global warming, caused by the greenhouse effect of the released CO_2, is currently one of the biggest threats to our planet.[5] Based on the Intergovernmental Panel on Climate Change (IPCC) report, the global climate has changed relative to its pre-industrial period and recorded a global mean surface temperature (GMST) increment by 0.87 ^{o}C during 2006–2015.[6] This increased GMST has already caused multiple observed climatic changes and if it is left uncontrolled or unchecked, the continuous GHGs emissions may cause GMST to increase by another 4 ^{o}C or more by 2100.[6] And, in the current IPCC report, it is projected with high confidence that the any GMST increment above 1.5 ^{o}C could be long-lasting and irreversible.

Hence, there is an urgent need to regulate the potential vectors of GMST overshoot. And, one of the major regulation policies includes the cutting down of CO_2 and other greenhouse gas (GHG) emissions by minimizing our fossil fuel dependence and promoting the development of environmentally benign alternative energy sources.[4] In spite of its adverse environmental impact, the increasing energy demand and depleting fossil fuel reservoirs are other global energy concerns which are knocking at the door of scientific community to introduce feasible approaches for the development of sustainable energy conversion and storage energy devices. In this regards, major focus has been directed toward harvesting various available renewable energies such as solar, wind, hydro, geothermal, biomass, etc.[7] However, the intermittency and localized nature of these renewable energy colonies are again questioning the global energy security. Hence, the development of energy devices which can store such an irregular energy supply is another essential part of future energy security. In this context, immense research

efforts have been dedicated to design energy storage devices, for example batteries and supercapacitors. However, such kind of energy-storage devices may have their own limitations while looking for huge energy storage as well as their widespread installations.

Considering this, the energy storage in the simplest chemical form of hydrogen from water has come into picture which not only mitigates the issues associated with energy storage devices but also provides the highest gravimetric energy density to all the known fuels.[1,2,7] Thus, hydrogen generation provides an overall solution to both store the intermittent renewable energy as well as provide sustainable source when generated from the plentiful water. Interestingly, hydrogen not only acts as a fuel but also provides us a better option as a versatile energy carrier to that of electricity.[1] Hence, the whole system of production, storage, and energy delivery in the chemical form of H_2 introduce the concept of 'hydrogen economy' which is having the potential to replace the current 'hydrocarbon economy'.[8] However, a general question which can come in anyone's mind is the amount of water required for hydrogen generation since we have limited supply of fresh household water and for the better energy efficiency, water splitting requires clean water. This is very nicely and quantitatively explained by Professor John A. Turner, where he compares the amount of water usage in various major sectors of U.S.[8] According to the survey and calculation Dr. Turner mentioned, about 100 billion gallons of water per year is required to generate H_2 for some 230 million fuel cell vehicle, which is nearly 1/3 amount of water required for gasoline production.[8] In this way, hydrogen economy can be a promising alternative for the current hydrocarbon economy.

1.2.   Brief history of hydrogen economy

In 1874, it was Jules Verne who first envisaged that the energy supply through fossil fuel is finite and proposed the possibilities of hydrogen derived from water as the future sustainable energy source through the statement "water will be the coal of the future".[9] Later on, in the 1930s Rudolf Erren also suggested the hydrogen generated from water electrolysis could be a promising transportation fuel.[10] Similarly, Francis Bacon suggested that hydrogen can also be a good energy storage system.[11] Apart from that, J. O'M. Bockris, in 1972, envisaged that hydrogen can provide us a cost-effective energy carrier.[12] The hydrogen economy would also produce enough fresh water for household purposes. Hence, the hydrogen produced through water will be abundant and copiously distributed to the entire world without any national barriers

and will constitute a future energy system which requires only technology not any political access. However, J. O'M. Bockris stated some more difficulties while switching to hydrogen economy, (i) conservatism to conventional fossil fuel, (ii) lack of enough education in electrochemical field and (iii) the public's fear of H_2.[12] Hence, for a successful implementation of hydrogen economy, the abovementioned difficulties need to be addressed.

1.3.   Current status of hydrogen economy

As already mentioned in the previous sections, the acceleration toward hydrogen economy is not due to any affection with hydrogen but because of the hope of beating the current hydrocarbon economy in terms of fuel cost, providing greater efficiency and less environmental damage. However, if the hydrogen is produced from fossil fuel reforming, then it will be of no significance to replace heat engine with hydrogen engines. Now, if we look at the major H_2 production sources, nearly ~96% of H_2 is currently supplied through fossil fuel and water-sourced H_2 contribute a mere 4% (Figure 1). Hence, before advancing the hydrogen engine-based vehicle technology, our goal should be to work for the wide-spread implementation of water-sourced H_2 generation plants. The major hurdle to increase the global contribution of water-sourced H_2 includes its practically achievable energy-efficiency as well as the plant installation cost.
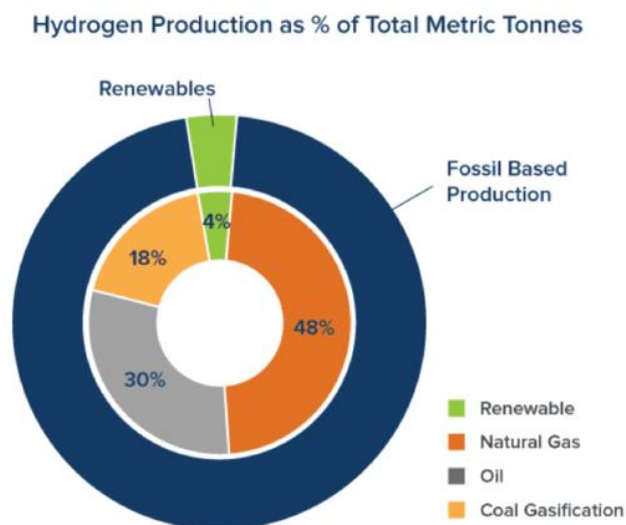
Figure 1. Pie chart for contribution of various sources toward global hydrogen production.[13]

Now, if we talk about the energy efficiency of the two hydrogen generation sources, both fossil fuel reformers ($C_nH_m + [O] \rightarrow CO_x + H_2$) as well as water electrolyzers ($2H_2O + (energy) \rightarrow 2H_2 + O_2$) provide nearly equal and 60–70% energy efficiency.[8] However, the H_2 produced through reformers are cheaper than that of water-sourced H_2. This price disparity is because of the higher capital cost, lower life-time, and higher maintenance cost of the water-sourced H_2 production plants. Thus, there is an urgent need to identify the possible ways to overcome the above-mentioned hurdles and build water-sourced H_2 production systems with lower capital cost. First of all, to practically access the per kg H_2 price variations, it is essential to survey some currently available H_2-production industries. For example, according to the 2015 California Energy Commission report, the average H_2 fuelling station installation cost *via* on-site water electrolysis technology ranges form 3–4 $ million (Figure 2).[14] Whereas with fossil fuel reforming technology the station installation cost ranges from 1.5–2 $ million. Accordingly, the water-sourced per kg H_2 costs in the range of 20–30 $ which is nearly double to that produced through methane reforming, *i.e.,* 10–15 $/kg. Hence, to increase the H_2 production contribution through water splitting, extensive research is needed to reduce both station installations cost as well as per kg H_2 production cost.

Station Developer	Station Technology	Total Station Cost ($ million)	Levelized Cost ($/kg)
FirstElement	Fossil Fuel-sourced	2.05	13.00
Linde	Fossil Fuel-sourced	2.78	9.90
HyGen	On-Site Electrolysis	3.25	24.00
Air Liquide	Fossil Fuel-sourced	3.26	13.80
ITM Power	On-Site Electrolysis and Fossil Fuel-sourced	2.73	22.70
H2 Frontier	On-Site Electrolysis	4.61	33.30
HTEC	On-Site Electrolysis and Fossil Fuel-sourced	3.25	17.90
Ontario CNG	On-Site Electrolysis	2.51	18.30

Figure 2. Summary of few hydrogen fueling stations and technologies funded by California energy commission (2015 Report).[14]

1.4.   Scenario of hydrogen production in India

In India, research on the development of hydrogen energy has started in 1976 and includes almost all the areas of relevance to the deployment of hydrogen as an energy vector.[15] These deployment included H_2 generation from water by electrochemical, photochemical, and biophotochemical water electrolysis, its storage as liquefied H_2 and metal hydrides, its end utilization as thermal and engine fuel. It was Shri AMM Murugappa Chettiar Research Centre (MCRC), Chennai, who has first demonstrated H_2 generation from distillery waste in batch-scale.[16] Later on, the pilot plant was able to generate up to 18,000 litres H_2 per h. Chlor-alkali industries are one of the major source of hydrogen production in India.[16] Current focus in India includes to work both on research level as well as on scaling-up of all the possible technologies of hydrogen generation. It also includes the work toward setting-up hydrogen purification unit, compression system to fill cylinders, and on-board application of hydrogen in vehicles.

1.5.   Water splitting and its types

To reduce the water-sourced hydrogen cost, first of all, it is important to know the fundamentals and various possible pathways of water splitting reaction. Hence, the upcoming sub-sections are devoted to explain the mechanism of various possible pathways of hydrogen production from water.

Water splitting is a process which involves the H–O–H bond breaking into its chemical components, *i.e.,* hydrogen and oxygen molecules (Figure 3). Owing to its thermodynamically unfavorable characteristics, water splitting always needs external source of energy.[17]

$$H_2O \text{ (l)} \rightarrow H_2 \text{ (g)} + \tfrac{1}{2} O_2 \text{ (g)} \qquad \Delta G° = +237 \text{ kJ/mol}$$
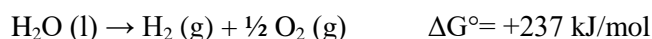
Depending upon the nature of the supplied energy source, water splitting can be classified in various types:[18]

1.5.1. Photochemical water splitting:[17] When light or photochemical radiations are the energy source to induce water splitting, the reaction is called photochemical or photocatalytic water splitting.[18] It is one of the promising options for hydrogen production by directly harvesting the renewable energy, *i.e.,* sunlight. A similar version of water splitting also occurs in photosynthesis where plants take water, sunlight and CO_2 from atmosphere to first convert into H_2 and O_2.[1] Plants then use hydrogen to manufacture carbohydrates and emit oxygen to the
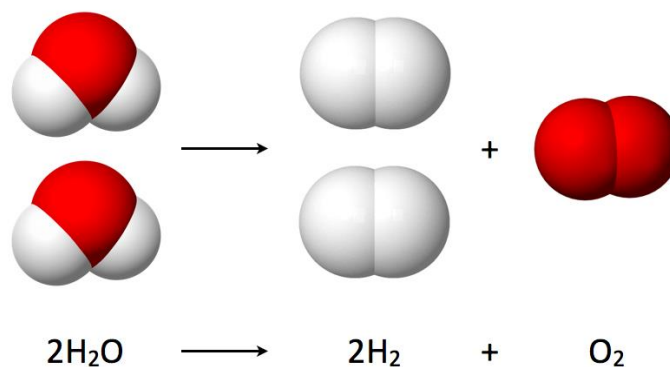
Figure 3. Schematic representation of breaking of water a molecule into its constituents. (Source: https://en.wikipedia.org/wiki/Water_splitting#/media/File:Electrolysis_of_Water.png)

atmosphere. Hence, photosynthesis offers a stunning opportunity to approach the photocatalytic hydrogen generation problem. And, by fully understanding the molecular structure and functions of nature's efficient manufacturing process, artificial materials can be discovered. Based on a number of fundamental studies, the most important criteria for solar-driven water splitting is found to be the electronic band gap alignment of the photosensitive materials with the redox potential of water. Hence, photocatalytic water splitting offers the potential for a cleaner pathway of CO_2-free hydrogen production. Over the years, significant progress has been made by an increasing number of research groups; however, many aspects of the function of photocatalysts are still unclear and need further improvements in the photocatalyst development. Further efforts concerning the designing of novel co-catalysts are highly demanding to provide additional breakthroughs for the overall realization of cost-effective H_2 production. In spite of this, photocatalytic hydrogen generation pathway suffers from the intermittency and localized nature of the solar energy, restricting its global implementations.

1.5.2. Thermochemical water splitting:[19] In thermochemical water splitting or thermolysis, water splits into its constituents by thermal energy provided through very high temperature ranging from 500–3000 $^{\circ}$C.[19] The water dissociation through thermolysis produces a number of reaction products, mostly H, H_2, O, O_2 and OH. The heat is generally supplied through concentrated solar power or waste heat of nuclear power stations. The thermal energy provided through concentrated solar power provides hydrogen generation pathway in a renewable and safer manner. However, the limitation lies in the efficiency and high temperature

durability of the materials employed. High cost of the concentrating mirror systems also inhibits the widespread implementation of this technology. In addition, nuclear power-driven thermolysis also offers the opportunity to generate hydrogen with negligible greenhouse gas emissions. However, the risks associated with the nuclear power plants as well as their radioactive waste hinder its large-scale development.

1.5.3. Electrochemical water splitting:[20,21] Electrochemical water splitting or water electrolysis involves the passage of electric current through water to induce its dissociation into H_2 and O_2. On one electrode, water oxidizes and releases oxygen molecules and electrons; these electrons then travel through the outer circuit to reach the cathode. On the cathode side, these electrons then reduce water to liberate hydrogen (Figure 4). Theoretically water electrolysis requires 1.23 V; however, it always requires higher voltage to overcome various reaction barriers. The unit for water electrolysis is called electrolyzer and its size can range from a small laboratory setup to appliance-size equipment for commercial hydrogen production to large-scale, central production facility. As compared to photolysis, electrolysis of water offers the freedom to club it with variable renewable energy sources. Moreover, the working principle of electrolysis is simpler than photolysis. Furthermore, water electrolysis is much safer than high temperature thermolysis. In brief, water electrolysis is found to be the feasible hydrogen generation technology as compared to photolysis and thermolysis. Despite the above-mentioned superiorities, water electrolysis also suffers from numerous challenges where intensive research focus is needed to reduce its capital cost as well as to improve its energy efficiency.

Hydrogen generation through water electrolysis is the major focus of the present thesis. Hence, water electrolysis is further elaborated in the upcoming sections.

1.6.   Water electrolyzer

1.6.1. Major components of water electrolyzer: In an engineering point of view, water electrolyzer is a very simple device consisting of two electrodes (cathode and anode) kept in two separate chambers separated by a liquid or solid electrolyte (Figure 4). In case of liquid electrolyte, the two chambers are connected through a separator which allows the electrolyte flow but stops the two product gas mixing.
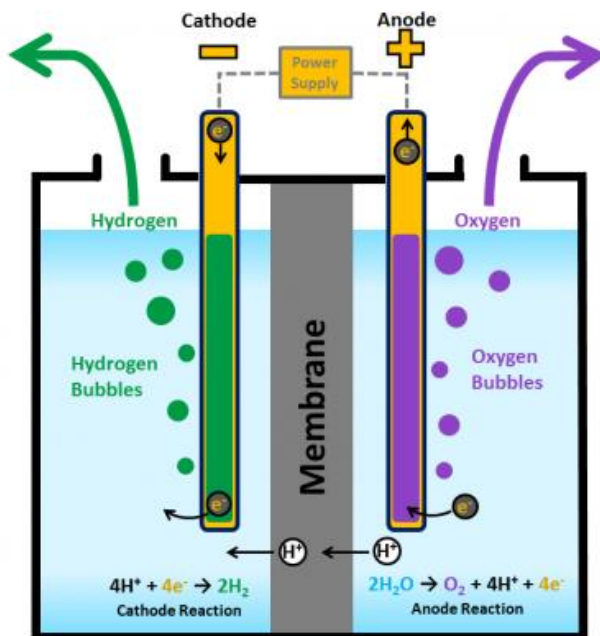
Figure 4. Schematic illustrations of the water electrolyzer component and its working principle.[22]

1.6.2. Working principle: Water electrolysis is an electrochemical reaction, which requires electrical energy to split the water into hydrogen and oxygen.

$$H_2O \text{ (l)} \rightarrow H_2 \text{ (g)} + \tfrac{1}{2} O_2 \text{ (g)} \qquad \Delta E° = 1.23 \text{ V } vs. \text{ RHE}$$

In water electrolyzer, water gets oxidized at anode to generate oxygen molecules (Oxygen Evolution Reaction, OER) and, at the cathode, water gets reduced to evolve hydrogen molecules (Hydrogen Evolution Reaction, HER).

Anode (Water Oxidation): $\qquad 2H_2O \text{ } (l) \rightarrow O_2 \text{ } (g) + 4 \text{ H}^+ \text{ } (aq) + 4e^- \qquad E^o_{ox} = -1.23 \text{ V}$

Cathode (Water Reduction): $\qquad 4H^+ \text{ } (aq) + 4e^- \rightarrow 2H_2 \text{ } (g) \qquad E^o_{red} = 0.00 \text{ V}$
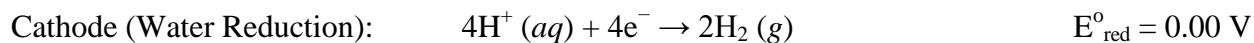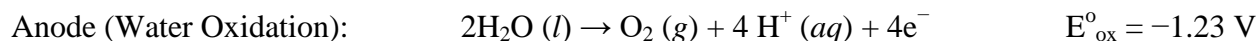
In spite of the essential role of anodic water oxidation to provide electrons and protons for hydrogen generation, it is also an essential counter reaction in CO_2 reduction for providing electrons and protons. Moreover, water oxidation half-cell is also a crucial half-cell reaction in rechargeable Zinc-air battery to redeposit zinc (fuel) during the battery charging.

1.6.3. History of water electrolyzer: Electrolysis was first reported in 1789; later on in 1800, William Nicholson and Anthony Carlisle demonstrated the water electrolysis for the first time in lab.[18] Afterwards it has been widely studied and applied. In initial water electrolysers, alkaline electrolytes were used; later on, water electrolysis was also studied in acidic medium. Some demonstrations were also made with neutral electrolytes, but, the performance was found to be very low. Searching for an electrical and corrosion resistant gas separating membranes was also a challenging task. In place of mere a gas separating membrane, to avoid leakage and corrosion, development of solid electrolyte was also the major concern. First progress in the solid electrolyte membrane was found with proton exchange membrane. However, owing to the stability of only noble metal-based electrocatalysts in harsh acidic conditions, the capital cost of the device was too expensive to be implemented on large scale. Thanks to the alkaline electrolyte, in which most of the low cost earth abundant metal-based catalysts exhibit excellent activity and stability. However, the major hurdle remained is the lack of stable and well performing solid alkaline electrolyte membranes. Nevertheless, owing to the less corrosive nature and lower alkali concentration, currently, alkaline liquid water electrolyzers are the major focus for large-scale applications. Despite that, solid-PEM electrolyzers also have got copious industrial attention to look into the reaction mechanism and designing of low-cost catalytic materials.

1.6.4. Mechanism of the two electrode reactions: At first look, water electrolysis seems to be an easy and problemless way to produce H_2; however, it is not. To facilitate energy-efficient hydrogen generation through electrolysis, a deep understanding of the involved reaction pathways on the electronic and molecular level is essential. One of the major hurdles in this pathway is the variable kinetics of the two electrode reactions at two pH extremes. One of the half-cell reactions, *i.e.,* HER is more facile in acidic medium whereas the anodic OER shows better kinetics in alkaline medium. Hence, to improve the two half-cell reaction kinetics in the same pH medium, a thorough understanding of the mechanism involved is indeed mandatory. Thus, a detailed examination of the theoretical principle and pathways involved during the two half-cell reactions at the two pH extremes is elaborated as follows and also illustrated in Figure 5:
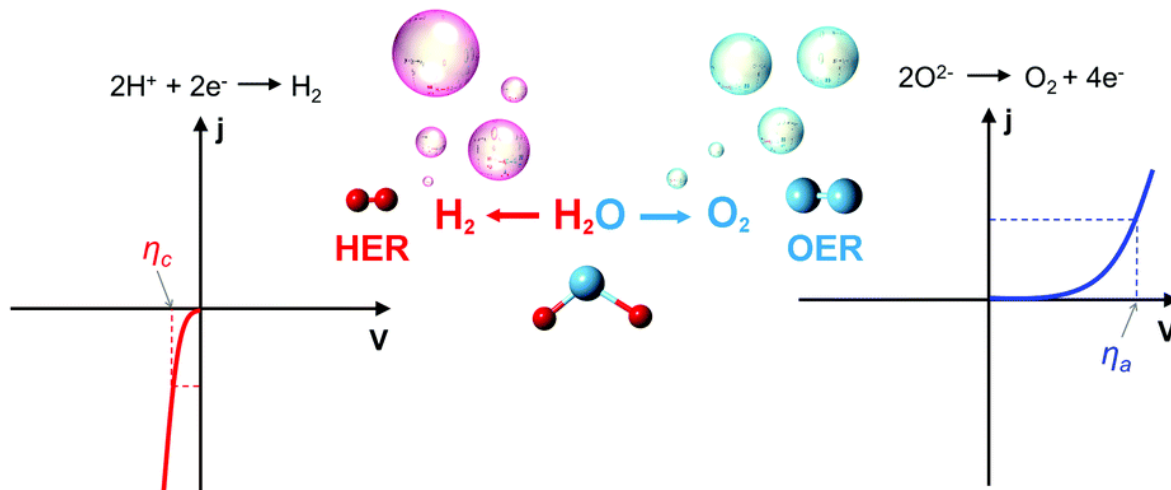
Figure 5. Performance evaluation curves for hydrogen evolution reaction (left) and oxygen evolution (right) where η_c and η_a are the overpotentials for cathode and anode at the same current (j).[23] (Reproduced by permission from Royal Society of Chemistry; Licence no. **4691291149744**)

1.6.4.1. Anodic oxygen evolution reaction: In water electrolyzer, among the two half-cell reactions, anodic water oxidation reaction is found to be more sluggish, owing to its four electron-proton coupled heterogeneous reaction pathway. Moreover, to date no universal OER reaction mechanism is defined and it is found that OER mechanism changes from one type of materials to another type and it is highly pH dependent. Hence, the most-widely proposed OER reaction pathway at the two pH extremes is elaborated here one by one:

In acidic medium: In acidic medium, because of the negligible hydroxyl concentration, the reaction starts with the adsorption and breaking of H–O–H bond.

$$2H_2O\ (l) \rightarrow O_2\ (g) + 4H^+ + 4e^- \qquad @pH = 0 \qquad E^o = 1.23\ V$$

The most probable mechanism of water oxidation under acidic conditions follow the given pathway:[23]

$$M + H_2O\ (l) \rightarrow MOH + H^+ + e^- \tag{1}$$

$$MOH + OH^- \rightarrow MO + H_2O\ (l) + e^- \tag{2}$$

$$2MO \rightarrow 2M + O_2\ (g) \tag{3a}$$

$$MO + H_2O\ (l) \rightarrow MOOH + H^+ + e^- \tag{3b1}$$

$$MOOH + H_2O\ (l) \rightarrow M + O_2\ (g) + H^+ + e^- \tag{3b2}$$
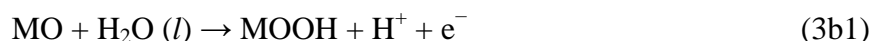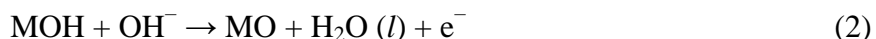
In alkaline medium: In case of alkaline medium, due to the plenty of hydroxyl groups, the water oxidation starts with the OH^- adsorption on the active centers.

$$4\,OH^-\,(aq) \rightarrow 2H_2O\,(l) + 4e^- + O_2\,(g) \qquad @pH = 14 \quad E^o = 0.40\,V$$
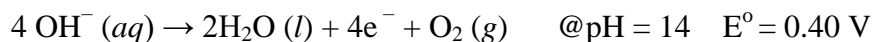
The most accepted reaction pathway of water oxidation under alkaline conditions is:[23]

$$M + OH^- \rightarrow MOH \tag{4}$$
$$MOH + OH^- \rightarrow MO + H_2O\,(l) \tag{5}$$
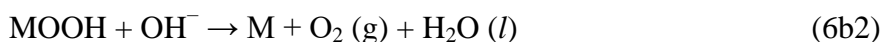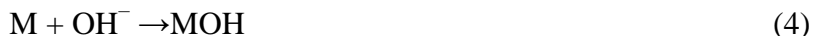$$2MO \rightarrow 2M + O_2\,(g) \tag{6a}$$
$$MO + OH^- \rightarrow MOOH + e^- \tag{6b1}$$
$$MOOH + OH^- \rightarrow M + O_2\,(g) + H_2O\,(l) \tag{6b2}$$

Hence, from the above two as-proposed mechanisms, it can be concluded that OER at the anode for either acid or alkaline conditions show some disparities as well as similarities. The proposed pathways include same intermediates such as MOH and MO. Noticeably, there are two ways to form O_2 from a MO intermediate (Eqn 3a or 3b/6a or 6b). Among which, one is *via* the direct combination of 2MO to produce $O_{2(g)}$ (Eqn 3a or 6a), and the other approach involves the formation of the MOOH intermediate first, (Eqn 3b or 6b) which subsequently decomposes to $O_{2(g)}$. From here, it can be anticipated that, in the case of acidic medium, the direct combination of MO could be the most probable pathway, whereas in case of alkaline medium, due to the plentiful hydroxyl moieties, the MOOH formation pathway could be the preferred step to form the oxygen molecules. In addition, from the plausible reaction pathways at the two pH extremes, it can be anticipated that OER is more favorable in alkaline medium. Since, in case of acidic medium, the reactants are neutral water molecules, which need higher energy to get break and liberate hydroxyl groups for the further reaction proceedings. However, in alkaline medium, there are plentiful hydroxyl moieties which do facilitate the easy water molecule polarization to start the reaction. Moreover, in acidic medium the hydroxyl moieties have very short life-time which again affects the reaction kinetics. Despite these differences, the common consensus is that the overall kinetics of the OER electrocatalysis depends upon the bonding interactions of M–O during the formation of various intermediates, *i.e.,* MOH, MO and MOOH.[23]

1.6.4.2. Cathodic hydrogen evolution: The cathodic hydrogen evolution reaction is a pH dependent two electron transfer reaction. Unlike OER, the HER reaction mechanism is relatively

simpler and is widely proposed to be composed of two out of three microscopic steps (Tafel/Volmer or Heyrovsky/Volmer).[24,21] At the two pH extremes, the as-projected pathways have been proposed with different proton-generating reactants.

In acidic medium: Here, HER is found to be more favorable owing to the proton-rich atmosphere, which directly involves as reactants.

$$4H^+ (aq) + 4e^- \rightarrow 2H_2 (g) \qquad\qquad @pH=0 \quad E^o = 0.00 \text{ V}$$

The three microscopic steps in acidic medium proceed as follows:

A. Volmer reaction (electrochemical hydrogen adsorption):
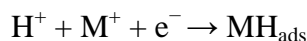
$$H^+ + M^+ + e^- \rightarrow MH_{ads}$$

B. Followed by Heyrovsky reaction (electrochemical desorption):

$$MH_{ads} + H^+ + e^- \rightarrow M + H_2$$

C. Or Tafel reaction (chemical desorption):

$$2MH_{ads} \rightarrow 2M + H_2$$
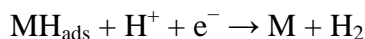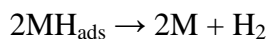
In alkaline media: At higher pH, HER is found to be comparatively sluggish. It is due to the proton-deficient atmosphere, where protons for H_2 generation need an extra step through water dissociation. Hence, in alkaline medium, water dissociation is always a rate-determining step.
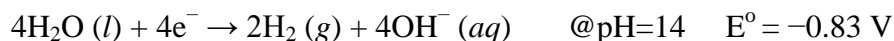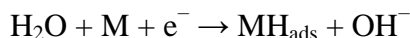
$$4H_2O (l) + 4e^- \rightarrow 2H_2 (g) + 4OH^- (aq) \qquad @pH=14 \quad E^o = -0.83 \text{ V}$$

A. Volmer reaction (electrochemical hydrogen adsorption):

$$H_2O + M + e^- \rightarrow MH_{ads} + OH^-$$

B. Followed by Heyrovsky reaction (electrochemical desorption):

$$MH_{ads} + H_2O + e^- \rightarrow M + OH^- + H_2$$

C. Or Tafel reaction (chemical desorption):

$$2MH_{ads} \rightarrow 2M + H_2$$
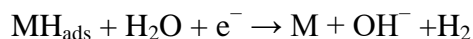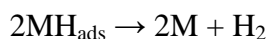
1.6.5. Classification of water electrolyzer

Based on the pH of the electrolyte medium, water electrolyzer can be classified into three major types, *viz.*, alkaline water electrolysis, acidic water electrolysis and high temperature ceramic membranes (solid oxides membranes) water electrolysis.[3] Among which, acidic water electrolyzers employ solid polymer electrolyte membrane in place of liquid electrolyte and are widely employed as solid-state electrolyzers. These electrolyzers are free from any electrolyte leakage issues, produce hydrogen with high purity (>99.99%) and offer possibility to produce at H_2 at high pressure. However, acidic electrolyzers suffer from the high cost and low durability of catalyst materials restricting its wide-spread commercialization. In this regard, alkaline electrolysers are more advantageous due to their less corrosive nature, and low-cost as well as better durability of the catalyst materials. Another water electrolyzer type, *i.e.,* high temperature water electrolysis, employs solid oxide electrolyte and offers advantage over alkaline and PEM electrolysers in terms of higher efficiency and lower capital costs. Solid oxide membranes are prepared from calcium and yttrium stabilised zirconium oxide. The only disadvantage is its operation temperature, *i.e.,* 900–1000 °C, which raises the safety concern. In summary, all the above-mentioned types of water electrolyzers have the potential for large-scale hydrogen production. However, all of them have their own advantages and disadvantages which need further research focus to improve their energy efficiency as well as to reduce the cost.

1.7.   Current status and roadblocks of alkaline water electrolysis[15,16,3]

Among the above-mentioned three technologies, this thesis focuses to contribute toward the advancement in the alkaline water electrolysis, since it is a matured technology and is commercially available in megawatt range. It is also demonstrated with a stack life of <90,000 h and a system life of 20-30 years which is superior than the PEM-based water electrolyzers which showed an average of <20,000 h stack life with an estimated system life of around 10-20 years.[3] Moreover, the currently available PEM water electrolyzers have a H_2 production rate ranging from 0.06 to 75 Nm³/h whereas the alkaline electrolyzers have reached the H_2 production rate of 760 Nm³/h. However, one of the major challenges with these alkaline electrolyzers is related to the unavoidable CO_2 attack responsible for the electrocatalysts poisoning as well as impurity in the hydrogen produced. In an effort to improve the energy efficiency, Bhabha Atomic Research

Centre (BARC), Mumbai, has successfully demonstrated alkaline water electrolyzers with higher current density (4500 A m^{-2}) based on the indigenously manufactured advanced electrolyzers incorporating porous nickel electrodes. In general, the H_2 production through water electrolysis is a highly energy intensive process (4.5-6.5 kWh/Nm^3). And, this high energy consumption is coupled with high capital investment, which is restricting the water electrolysis technology for commercial purpose. Hence, a number of strategies are needed to be designed for bridging the gap through various government plans by combining relevant institutes and industries.

1.8.   Scope of the research

Among the various strategies proposed for the capital cost reduction of water electrolysis technology, boosting the kinetics of the involved electrochemical processes play a key role. Hence, designing of robust multifunctional electrocatalysts is indeed the first step in the water electrolyzer commercialization roadmap because they boost-up the reaction rate and improve energy efficiency and product selectivity of the chemical transformations involved. As it is already mentioned in the previous section, non-noble metal-based materials perform quite efficiently in alkaline electrolyzers. Moreover, over the past years, substantial advancement has been made in the designing of various low-cost robust electrocatalytic materials to catalyze the two involved half-cell reactions. Today's electrocatalysts, however, are not suitable for their large-scale implementation; hence, tremendous research focus is still required to realize their commercial usage. Other brand-new strategies which have started coming into picture to improve the energy efficiency of H_2 generation involve replacing the previously-stated sluggish water oxidation reaction with reactions involving readily oxidizable species. This strategy covers poorly-explored but wide-range of ideas which can be proven to be a better way in near future to perform alkaline water electrolysis for cost-effective H_2 generation. Notwithstanding, the execution of these strategies are also governed by the kinetics of the involved electrochemical reactions. Hence, the knowledge of material property tuning for electrocatalytic material development is of paramount to realize the commercialization of any electrochemical transformation processes. In this context, the up-coming sections discuss about the electrocatalysis of the employed reactions in the two aforementioned strategies.

1.8.1. Electrocatalyst development for alkaline water electrolysis:[21,25] Designing of a robust material to catalyze any particular reaction requires a deep understanding of the reaction mechanism through a combination of theoretical and experimental studies. In this respect, over the period of time, a number of materials have been developed and demonstrated for catalyzing various electrochemical transformations. In general, the catalyst designing strategies should aim to populate active sites and/or improve the intrinsic activity of each active site. Currently, precious group metals are most active catalysts to catalyze both the half-cell reactions of water electrolysis. However, their high cost and scarcity have led to the development of various non-precious group metal-based (non-PGM) electrocatalysts. In fact, Ni and Fe-based catalysts are generally employed in alkaline electrolyzers; however, further performance tuning is still desirable to increase the hydrogen production energy efficiency. In this regard, transition metal chalcogenides, carbides, and phosphides are demonstrated as an alternate to Pt-based materials to catalyze HER. In addition, metal hydroxides are also evidenced to be an important HER catalytic component to boost-up the rate determining water dissociation step. In a similar way, phosphates, oxides, and hydroxides are also proven to be good substitutes to the benchmark Ru/Ir-based commercial catalysts toward OER. To further improve their catalytic property, a number of additional efforts have been put to bridge the performance gap between the Pt-based and non-PGM based catalysts.

Apart from this, enormous efforts have also been paid toward the designing of bifunctional electrocatalysts which can catalyze both the half-cell reactions in the same pH medium. Among the various strategies, it is found that hydroxides play unprecedented role as an effective catalytic component to facilitate both the half-cell reactions in alkaline medium.[26,27,28,29] In this direction, layered double hydroxides (LDHs) have emerged as a very interesting class of materials which can fulfill many essential catalytic requirements, for example, active center dispersion, better metallic hybridizations, open space, shape tuning, and low-cost synthesis.[28,29,30] With these superiorities, this dissertation aims to contribute toward the property tuning of LDHs for the electrocatalytic hydrogen generation which will be elaborated in the following sections.

1.8.2. Strategies to replace the energy-intensive water oxidation half-cell:

Although enormous efforts have been devoted to improve the kinetics of both the half-cell reactions of industrial alkaline water electrolyzers, hydrogen generation still needs a minimum of

1.8–2.0 V.[31] Hence, along with developing efficient electrocatalysts, research focus should also be directed to identify and build alternate strategies for energy-efficient and cost-effective hydrogen generation.[32] In this context, a thorough survey has been performed to find out the possible strategies which have been adopted to generate hydrogen from water by harvesting other form of waste energy. Here, all the possible ways to replace energy-intensive water oxidation can be broadly categorized into three sections:

1.8.2.1. Replacement with waste organics oxidation: This category involves the replacement of water oxidation with organics oxidation which shows lower thermodynamic oxidation potential to make the hydrogen generation energy-efficient.[32] However, these organic molecules should be available as a waste in atmosphere or are cheaper.[31] The water oxidation replacement with readily oxidizable species includes the oxidation of urea, hydrazine, alcohols, or other toxic waste organic compounds, generating as a by-product and enter in our water bodies through one or another type of human activities or as industrial effluents.[33,34,35,36] In this way, this approach may provide dual benefits, *i.e.,* simultaneous low-cost hydrogen generation as well as waste-water treatment. This waste-water treatment otherwise needs additional manpower and energy to realize. Additionally, such wastewater utilization can save the useful household water for H_2 generation, which adds another motivational point to promote this technology since availability of clean and fresh water is also currently emerging as a global issue.

1.8.2.2. Replacement with organics oxidation generating value-added products: This category also involves the replacement of energy-intensive water oxidation with readily-oxidizable organic molecules. However, this category includes the oxidation of those kinds of organic molecules which generates value-added products.[37] Hence, through such kind of strategy, the hydrogen generation can be coupled with various organic transformations, where through electrochemical decoupling the energy involved during the reactant oxidation can be electrochemically harvested.[38] The harvested energy, hence, can be utilized to generate hydrogen along with value-added products. In this way, this strategy also provides essential motivational points for its large-scale implementation.

1.8.2.3. Replacement with electropositive metal oxidation for simultaneous hydrogen and electricity generation: This is another category where the water oxidation

can be replaced with electropositive metals.[39] This is the most appealing strategy since it can also generate electricity along with the hydrogen generation. And, in this category, no external energy source is needed to supply as it is needed in the case of the above-mentioned categories. The electropositive metal gets oxidized and it provides electrons for the cathodic water reduction to liberate H_2.[40] Depending upon the standard reduction potential of the metal and the overpotential of the cathodic reaction, the excess energy can be harvested as electricity. In this case, the energy-efficiency is defined by the stability of the metal in the employed electrolyte and overpotential of the cathodic reaction.

Apart from the above mentioned strategies, there can be many other strategies which would have been reported previously as well as there can be many more strategies which are yet to be explored. And, the exploration of such kind of strategies can take us to increase the water sourced hydrogen production contribution from ~4% to eventually 50% and so forth. Notwithstanding, the given strategies themselves give us the motivation to generate H_2 with much lower applied energy and in more viable manner. However, the viability and energy efficiency of all the mentioned strategies are governed by the kinetics of the involved reactions. Hence, development of robust multifunctional catalysts is again the key parameter for the success of all these strategies. And, as illustrated earlier, the present dissertation aims to tailor the LDH property for designing robust multifunctional electrocatalysts for energy-efficient H_2 generation. In fact, in some of the above-mentioned strategies, designing of the LDH-based electrocatalytic materials is already adopted and the catalytic efficiency is found to be improved. With this, the upcoming sections are now aligned to understand the structure and property tuning of LDH for the electrocatalytic applications.

1.9.   Layered double hydroxides (LDHs)[29,41,30]

Layered double hydroxides (LDHs) are a broad class of two-dimensional (2D) anionic clay materials, predominately comprising of three parts: the two positively charged brucite-like host layers sandwiching the interlayer anions and solvent molecules to balance the excess positive charge. In LDHs, the brucite layers are elucidated to composed of bivalent metal cations (*e.g.,* Co^{2+}, Ni^{2+}, Zn^{2+} and Fe^{2+}) in which a fraction of metal ions gets replaced with isomorphously trivalent metal cations (*e.g.,* Fe^{3+}, Al^{3+}, Mn^{3+} or Ga^{3+}). And, all these metal ions are octahedrally

coordinated by hydroxyl groups in MO_6 configuration, forming the positively charged layer *via* edge sharing. Owing to the incorporation of the trivalent metal cations, the hydroxide layer gets extra positive charge, and to balance this additional positive charge, a number of organic or inorganic anions (*e.g.,* CO_3^{2-}, Cl^-, NO_3^-, and SO_4^{2-}) present in the mother liquor immediately get intercalated. That is how a lamellar structure forms, where all the hydroxyl groups in the brucite layer orient toward the interlayer space region and form hydrogen bonds with the interlayer anion and solvent molecules (Figure 6). Thus, a general molecular formula can be expressed as $[M^{2+}_{1-x}M^{3+}_x(OH)_2][A^{n-}]_{x/n}\cdot zH_2O$, where M^{2+} and M^{3+} represent the divalent and trivalent metal cations, respectively, A^{n-} is the filled interlayer anions, and x ranges from 0.2 to 0.4. Of note, LDHs may also contain M^+ and M^{4+}.
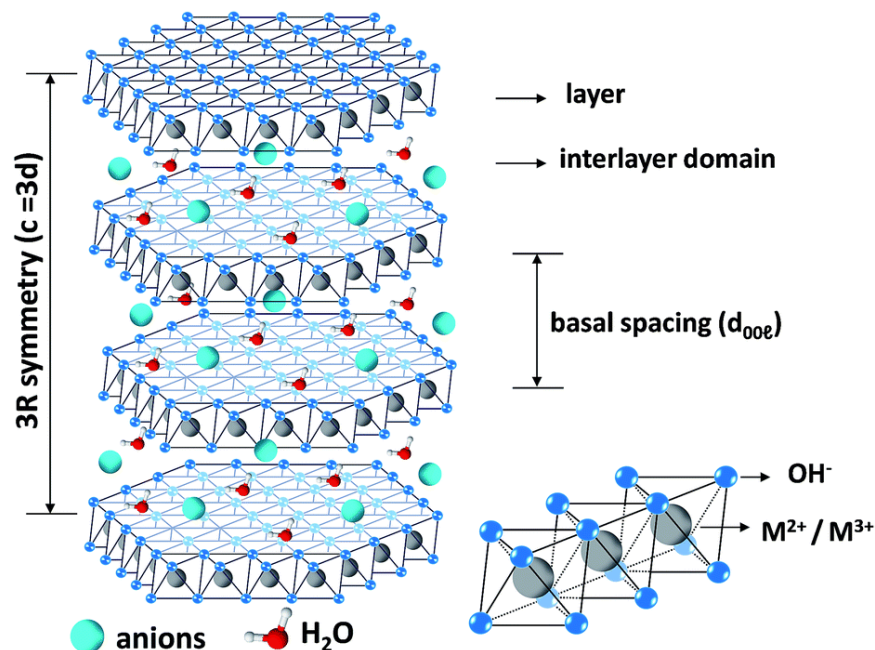
Figure 6. Schematic illustration of layered double hydroxide structure.[42] (Reproduced by permission from Royal Society of Chemistry; Licence no. **4691371059293**)

1.10. Structure-property correlation of LDHs

LDHs are a family of lamellar 2D materials which gained enormous attention to fulfill specific requirements in a wide variety of fields, including as adsorption materials, polymer additives, precursors for functional materials, and in pharmaceutics, photochemistry and electrochemistry.[43] Owing to the 2D lamellar structure with open interlayer structure, easy interlayer ion exchangeability, and simple synthesis processes, LDHs have emerged as promising

candidates for designing multifunctional materials. This section, after a through literature survey, tries to include various possible ways to tune the LDH properties for a wide range of applications. The structure-property correlation strategies of LDHs with a special focus toward their electrocatalytic applications can be summarized in the following sub-sections:

1.10.1. Synthesis and morphological tuning[44,45,30]

As compared to the expensive noble-metal catalysts, LDHs provide the opportunity to design inexpensive and abundant functional materials by simply tailoring their one or more properties *via* low-cost synthesis processes. In principle, the synthetic procedures are relatively simple and cost-effective and, in many cases, the desired product can be obtained in a single step. The most common synthesis methods include co-precipitation, electrodeposition, hydrothermal/solvothermal reaction, or the combined procedures.[29] Among which, the co-precipitation method is the conventional method involving a precipitant, generally strong bases, to a homogenous solution of two or multiple metal ions. This process, however, suffers from the phenomena of particle agglomeration and inhomogeneous particle distribution. To overcome such issues, hydrothermal/solvothermal processes, involving weak bases as precipitates, have got enormous attention and became the most widely applied methods of LDH formation. Moreover, hydro/solvothermal process allows the designing of a wide range of morphology, just, by controlling the reaction parameters, for example, reaction time, temperature, and pH. Another widely adopted synthesis method includes the electrodeposition pathway to induce LDH growth and it is found to be relatively simpler and less time consuming than the aforementioned ones. The electrodeposition process can accomplish the LDH preparation in few minutes on the electrodes; however, it is generally unable to provide a nice control over the morphological uniformity for a large-scale production.

In this context, hydro/solvothermal process provides us a low-cost and large-scale LDH production pathway having a good control over morphology as well as structural homogeneity. The structural or morphological tuning shows a direct relation with the active sites exposure, reactants surface adsorption capability, and the reactant/product transport. Hence, morphological tuning is a crucial factor to influence the activity of the functional materials. For instance, Sun and co-workers have developed single layer nickel–vanadium layer double hydroxide (NiV LDHs) by a simple one-pot hydrothermal method.[46] The 3D structured NiV LDH is composed of

ultrathin nanosheets with a thickness of ~0.9 nm. The as-developed NiV LDH nanosheets having high specific surface area are shown to expose more number of active sites resulting into better OER kinetics. In another report, Jin and co-workers designed a binary Ni–Co hydroxide-based electrocatalyst having a distinctive sandwich-like coaxial structure of the 3D $Ni@[Ni^{(2+/3+)}Co_2(OH)^{6-7}]_x$ nanotube arrays.[47] Here, the Ni nanotube arrays having open end are found to be homogeneously covered with NiCo LDH nanosheets resulting into larger surface area and faster electron transport, which ensured excellent OER activity.

1.10.2. Intrinsic electronic structure tuning

Owing to their unique 2D lamellar structure and excellent physicochemical properties, LDHs provide numerous possible ways of tuning their intrinsic electronic structure to design various types of functional materials. For instance, LDHs provide tunable interlayer space, tunable binary to ternary metal ion composition, uniform metal ion distribution, facile anion exchangeability, feasible metal/non-metal ion doping, defects and vacancy creation suitability. Hence, LDHs can fulfill the demand of designing a large family of functional nanomaterials through their inherent excellent physicochemical properties which are briefly described in the following sections:

1.10.2.1. Cationic doping: The extensive tunability of the types of metal cations as well as their M^{x+}/M^{y+} ratio allow the selection of a broad range of earth-abundant metals to furnish them with distinctive catalytic properties when the active components are suitably incorporated or synergized in the system. In fact, layered triple hydroxides are proven to exhibit better electrocatalytic activity probably owing to the nanostructural rearrangements in terms of morphology, the electronic structures, and electrical conductivity.[28,29] Therefore, cationic doping can be one of the efficient approaches to improve the activity of the functional materials.[48,49,50] For example, Guzm´an-Vargas and co-workers designed Co^{2+} substituted NiFe-LDH electrocatalysts *via* a co-precipitation method with tunable Co^{2+}/Ni^{2+} ratios which exhibited a very low onset overpotential of 265 mV toward OER.[51] Interestingly, Duan group has performed DFT calculations to study the role of cationic doping, *i.e.,* Mn^{4+} into the NiFe LDHs moieties.[52] They found that the cationic doping could narrow the bandgap, improving the electronic conductivity of NiFe LDHs which is reflected over their excellent OER performance. Not only

the ternary metal incorporation into the LDH crystal structure, but the elemental doping in LDH has also been proven as an efficient strategy for designing the functional catalytic materials by tuning their surface chemical environment and coordination valence. Recently, Jin and co-workers studied the effect of Al substitution as well as partial dissolution on ultrathin NiFeAl trinary LDH nanosheets toward alkaline water oxidation.[49] The ultrathin Ni_3FeAl_x-LDH nanosheets exhibited significant performance improvement toward the OER activity compared with that of Ni_3Fe-LDH. And, it is anticipated to be because of the increased number of low-coordinated Ni and Fe atoms after the trivalent Al ion incorporation in the NiFe LDH. In a similar way, Müller and co-workers have also synthesized mixed-metal LDH doped with La^{3+} and Ti^{4+} cations as energy-efficient water oxidation nanocatalysts.[53]

In summary, the cationic doping in the LDH-based materials can be one of the critical strategies for tuning their catalytic properties. Here, the cationic doping can tune the LDH property in many ways: i) it could change the LDH morphology, decrease their thickness and size to nanosheets resulting into surface area increment and hence active site exposure; ii) this could also induce the electrical conductivity enhancement of LDHs, thus accelerating the electron transfer process; and iii) the cationic species doping may tune the surface electronic structure of LDH and also change the surface chemical environment, *i.e.,* the coordination number of the surrounding active atoms and the valence of the element of LDH.

1.10.2.2. Anion exchange and the interlayer space tuning: As it is already described, LDH is made-up of two major subunits, *i.e.,* brucite-like cationic layers and the charge-balancing anions in the interslab space having alternate arrangement. In addition to the metal hydroxide layer, the intercalated anions also play an important role to influence the overall physicochemical property of LDH. Owing to the relatively weaker interlayer bonding interactions, the interlayer space exhibits excellent expanding properties as well as anion exchange. Hence, this unique anion replacement property results into the designing of a huge variety of host-guest assemblies with versatile physical and chemical properties. The importance of interlayer space as well as anion exchange toward electrocatalytic performance tuning of LDH can be broadly considered in two aspects: i) the interlayer distance tuning helps to increase the active surface area accessibility and hence to boost-up the reactants and products diffusion; ii) the nature of intercalated anions may tune the intrinsic catalytic activity of LDH. For example,

Long and co-workers reported the preparation of FeNi–GO LDH from FeNi–CO_3^{2-} LDH by CO_3^{2-} to graphene oxide anion exchange.[54] The graphene oxide intercalation resulted into improved electron transport through the strongly coupled GO, resulting into superior electrocatalytic properties of FeNi–GO hybrids toward OER.

Recently, the effect of intercalated anions on the water oxidation activity is investigated by Zhou *et al.*[55] and Hunter *et al.*[56] *via* detailed electrochemical and XPS characterizations combined with density functional theory calculations. In these studies, they emphasized that interlayer anions play key roles toward tuning the electrocatalytic performance of LDHs. Hunter *et al.* investigated that the Brønsted or Lewis basicity of the intercalated anions play an indispensable role in determining the OER activity. Zhou *et al.* anticipated that the multivalent anions having higher charge make LDH stronger proton acceptors and electron donors than the monovalent anions to reduce the activation barrier for water oxidation. Zeng *et al.* also studied the role of interlayer anions toward improving the urea oxidation kinetics.[57] In addition to the effect of anion intercalation, the interlayer spacing also plays an important role to tune the electrocatalytic properties of LDH. In this regard, Guan and co-workers illustrated the role of interlayer distances (0.78 and 0.95 nm, respectively) in NiFe LDH nanosheets toward water oxidation. And, the performance elucidation reflected that the OER activity improved with the increase in the interlayer spacing.[58]

1.10.2.3. LDH exfoliation: This is another important strategy to populate the active centers as well as to improve the turn-over frequency toward a particular catalytic reaction. In general, LDHs prefer to grow in layer-by-layer manner resulting into thick and bulky patches which generally suffer from low specific surface area and poor electronic conductivity. Such a growth pattern, thereby, severely affects the catalytic activities of LDHs. It is well documented that the 2D nanomaterials with mono or few-atomic layers not only increase the surface area to expose more number of active sites, but also improve the chemical and physical properties.[59] In this context, the delamination of bulk LDHs to ultrathin nanomaterials also results into the development of plenty of edges and corner sites along with the emergence of more dangling bonds, resulting into the active site formation with lower coordination.[60] And, it is widely demonstrated that such kind of edge and corner sites exhibit higher catalytic activities compared with the basal plane sites owing to their better feasibility toward the reactants and active

intermediate adsorption.[61] Recently, room temperature liquid exfoliation of layered materials has emerged as a promising pathway of producing novel single or few-layered 2D materials with drastically improved surface activity. Song and Hu produced monolayer NiFe LDHs, NiCo LDHs, and CoCo LDH nanosheets by room temperature formamide-assisted liquid exfoliation of their bulk counterparts.[62] They demonstrated that the OER performances of single-layered LDH nanosheets were far beyond the bulk LDHs. Moreover, all the monolayer LDH nanosheets exhibited a lower Tafel slope and a higher TOF value, affirming that monolayer nanosheets show higher electronic conductivity and a faster electron transport than the bulk counterparts.

1.10.2.4. Defects and vacancy creation: It is found that the LDH exfoliation process not only populates the active sites or improves the active site accessibility, but it also induces the surface atoms in the ultrathin 2D nanosheets to easily leave the lattice and result into a defective structure. Such a vacancy creation thus helps the disordered structures to lower their surface energy, and hence offers them with better stability.[59] Such a defective and disordered structure in the ultrathin 2D sheets can not only reduce the metal coordination number but it also affects the overall electronic structure, which in turn helps to tune the activity of the designed catalysts.[28,29,59] In this direction, extensive studies are thus performed toward the defect engineering for vacancy creation.[63,64,65,66,67] The defect engineering can be typically divided into three categories: anion vacancies (mostly in the form of oxygen vacancies), cation vacancies (metal ions vacancy) and multivacancies.[28] Recently, a number of studies have been performed which showed that the low coordinated Fe, Ni and Co sites in the disordered structures with vacancy positions were proven to be the active electrocatalytic sites, leading to improved catalytic activity compared to that in perfect structure.[65,68,69] Therefore, the appropriate defects insertion is considered as an effective strategy to tune the surface electronic structure of LDHs, and hence, their intrinsic electrocatalytic activity.

As stated in Figure 7, major methods employed for the vacancy creation in LDHs include plasma etching,[63,65] thermal treatment,[70,71] aqueous chemical treatment[66,72,73] and sonication[67]. In our best knowledge, Yuqin Zou and Shuangyin Wang were the ones who first developed the defective CoFe LDHs *via* a water-plasma-enabled exfoliation strategy.[65] Multi-vacancies (O, Co and Fe vacancies) created during the exfoliation process led to a significant enhancement in the catalytic activity.[65] To further support the above conclusion, they have also reported the

multivacancy creation through Ar plasma-induced exfoliation of bulk CoFe LDH into ultrathin CoFe LDH nanosheets.[63] The as-exfoliated ultrathin CoFe LDH demonstrated a higher electrocatalytic activity owing to the increased surface area, exposed active sites, and edge/corner sites. Apart from this, Yang and co-workers also reported defect-rich ultrathin CoFe LDH nanosheets as bifunctional electrocatalyst for the overall water electrolysis.[74] In this case, the hydrothermally-synthesized bulk CoFe LDH was exfoliated by room-temperature stirring in DMF–ethanol mixture for prolonged duration. The as-exfoliated CoFe LDH exhibited higher electrocatalytic activity toward both the half-cell reactions of water electrolysis which was better than that of bulk CoFe LDH.
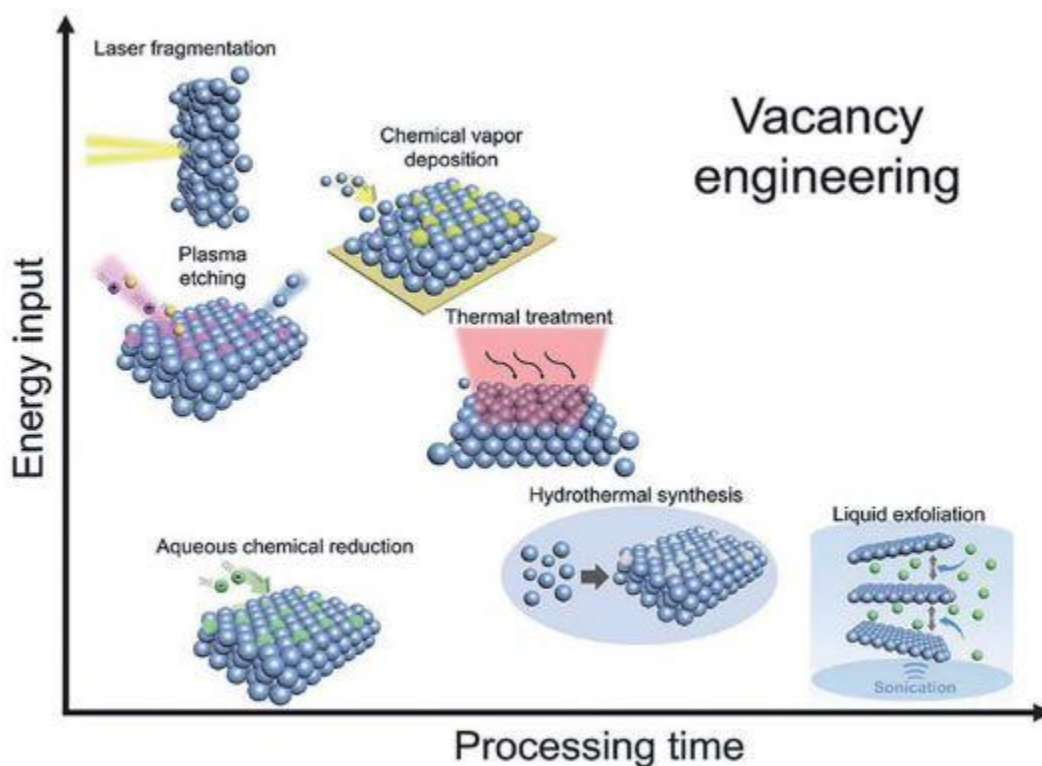
Figure 7. Schematic representation of the methods adopted for vacancy creation in LDHs.[28] (Reproduced by permission from Royal Society of Chemistry; Licence no. **4691371453453**)

Hence, defect introduction and vacancy creation play important roles to tune the electrocatalytic property of LDH by increasing the effective surface area, introducing unsaturated metal active sites with plenty of cationic and anionic vacancies, and improved electronic conductivity.

1.10.3. LDH nanocomposites: Apart from numerous fascinating structural properties, LDHs suffer from poor electronic conductivity which limits their efficiency in the field of electro-chemical energy storage and conversion. However, to solve the poor charge transfer issues, LDHs provide good hybridizing property with a number of conducting substrates, e.g., carbon-based substrates and metallic substrates *via* electrostatic interactions. Various types of carbon morphologies, *e.g.,* 2D graphene,[75,76,77] carbon nanotubes[78,79], and carbon quantum dots[80,81] have been explored to prepare LDH/carbon nanocomposites. Such kind of hybridized composites have been explored in developing various types of electrode materials with superior charge mobility and high surface areas. Among which, LDH hybridization with graphene having a two-dimensional honeycomb-like crystal lattice have been found as a promising pathway owing to its morphological resemblance with LDH providing larger surface anchoring sites for LDH growth and can also induce thin sheet-like LDH growth.[82] For instance, Wang *et al*. developed a hybrid material composed of NiAl-LDH platelets and graphene nanosheets under mild hydrothermal conditions for supercapacitor electrode application.[83] To further improve the LDH dispersion as well as to populate the LDH over graphene surface, Zhang *et al*. reported the anchoring of CoAl-LDH through the defect-induced nucleation and spatially confined growth of nano-sized CoAl LDHs into a mesoporous graphene framework.[84] Interestingly, various types of non-metallic dopants, e.g., nitrogen, sulfur, boron, *etc*. have also been found to facilitate the adsorption and anchoring of the metal cations, and, hence, the confined nucleation and growth of LDH.[85,86]

Another possible way of creating LDH/graphene composite is by using the exfoliated LDH nanosheets as the building blocks to electrostatically assemble with graphene.[87] Actually, graphene oxide (GO) nanosheet is 2D carbon material with numerous oxygenic functional groups that could be well assembled with LDH layers carrying the positive charge via electrostatic attraction in aqueous solution, resulting into hybrid sheets.[54] For example, Jin *et al*. demonstrated the formation of thin-layered CoAl-LDH-nanosheet/graphene oxide composite by assembling one-atom-thick sheets of carboxylated graphene oxide and exfoliated CoAl-LDH for the pseudocapacitance application.[87] Hence, the LDH/graphene composite not only enhances the electrical conductivity but it also offers higher active material dispersion, allowing a larger active metal population to be electrochemically addressable and accessible. Apart from the LDH/graphene composites, Gong and co-workers demonstrated improved OER activity and

stability of NiFe-LDH/MWCNT composites where ultrathin NiFe-LDH nanosheets were directly grown over slightly oxidized multiwalled carbon nanotubes (MWCNTs).[88] Apart from the above-mentioned carbon substrates, carbon quantum dots (CQDs) have been investigated to be fascinating nanocarbon structures with enriched surface functional groups. Notably, owing to the sub-5 nm particle size of CQDs, these carbon morphologies show many distinctive features such as high electronic conductivity, faster electron transfer, and reservoir properties, which can benefit for combining with the LDH-based materials to improve the electrocatalytic activity of the later.[89,90] Recently, Kang and co-workers reported the electrocatalytic property of CQD/NiFe LDH-based hybrid materials toward OER by combining CQDs with a size of about 5 nm with NiFe LDH nanoplates.[81]

Nickel foam (NF) is another extensively employed effective substrate to solve the electronic conductivity issues of LDH due to its high electronic conductivity, abundance, and porous 3D structure.[29] Owing to its open 3D structure, it facilitates proper LDH dispersion, hence exposure of the active sites.[32] It provides strong contact area between LDH and the substrate, and it also accelerates the mass transport during the electrochemical processes. For instance, Grätzel and co-workers directly grew NiFe LDH over NF for electrochemical applications.[91] Huang *et al.* also designed a Ni5Fe LDHs@NF composite where LDH was grown as a 3D hierarchical structure populated with ultrathin nanosheet exposed around the NF and the core of the alloy buried inside. Having this unique structure, the developed electrocatalyst required a low potential of 1.59 V at 10 mA cm^{-2} in 1 M KOH with superior durability during the overall water electrolysis.[92]

1.10.4. LDH derivatives: Over the years, LDHs have gained enormous attention owing to their feasibility to act as active material precursors to develop numerous functional LDH derivatives which can retain their two-dimensional layered structure with larger surface area and higher surface atoms exposure.[45] Therefore, a variety of LDH-based derivatives, for instance, metal hydroxides, oxides, oxyhydroxides, nitrides, phosphides, sulfides, and selenides have been explored in the area of electrochemical catalysis. Among which, some of the interesting efforts are described as follows:

1.10.4.1. Metal hydroxides, oxyhydroxides, and oxides: These are the simplest LDH derivatives with uniform metal distribution and are easy to design with unique physicochemical

properties which otherwise cannot be achieved through direct synthesis. For example, Xie *et al.* developed a single-crystalline β-Ni(OH)$_2$ ultrathin nanomesh with abundant and uniformly-distributed nanopores *via* an *in situ* etching of LDH precursors.[93] They, first exfoliated the NiAl LDH into ultrathin nanosheets and then, the Al constituents of the as-obtained nanosheets were selectively etched by alkali treatment to form porous β-Ni(OH)$_2$ skeleton. In comparison to the directly grown β-Ni(OH)$_2$, the LDH-derived ultrathin nanomesh structure exhibited larger surface area and plenty of active sites, which facilitated the fast charge transfer, better ion permeability, easy gas release and structural buffer for volume change during the OER process. In another report, Jin and co-workers also reported the designing of a porous β-Ni(OH)$_2$ as a robust water oxidation electrocatalyst by following a similar method.[94] The hydrothermally synthesized thin NiGa LDH nanoplates were subjected to alkaline treatment which induced the Ga^{3+} ions removal from the LDH nanostructures. The obtained porous β-Ni(OH)$_2$ nanosheet exhibited improved OER property as compared to the bulk NiGa LDH precursor and the directly synthesized β-Ni(OH)$_2$ microplates.

1.10.4.2. LDH-derived nitride/phosphide electrocatalysts: Owing to the limited electrical conductivity of hydroxides and oxides, in recent past, transition metal phosphides (TMPs) and nitrides (TMNs) have been extensively investigated in the field of electrochemistry. Both metal phosphides and nitrides show metallic nature, leading to many desired features such as high corrosion resistance and better electronic conductivity which can better promote the electron transfer during the catalytic oxidation and reduction of water. As it is already explained, in comparison to the direct phosphide or nitride synthesis, use of LDH precursors can add a number of functional components such as 2D structure, better atomic dispersion, exposed active sites and defect creation. Hence, the designing of the LDH-derived phosphides or nitrides can inherit both LDH as well as phosphide/nitride properties. For example, Sun and co-workers reported the low-temperature phosphidation of CoFe hydroxide precursors which resulted into the formation of Fe-doped CoP nanoarray.[95] Moreover, the easy compositional tunability of LDH materials can be taken into account to easily tune the compositional ratio in the final product. For instance, Hu and co-workers have investigated that the LDH-derived bimetallic (Fe$_x$Ni$_{1-x}$)$_2$P nanoarrays act as a robust electrocatalyst for OER in alkaline and neutral media.[96] In a similar way, Wu and co-workers reported the formation of LDH-derived Ni$_3$N nanosheets for the first

time with excellent water oxidation ability. With this work, new avenues for the development of the LDH-derived bimetallic TMNs have been explored.[97] For instance, thermal ammonolysis was adapted to convert ultrathin Ni_3Fe-LDH nanosheets into Ni_3FeN moieties with a particle size of 100 nm and a thickness of about 9 nm which showed excellent overall alkaline water electrolysis activity.[98]

1.10.4.3. LDH-derived bimetal sulfides/selenides: In addition to phosphides and nitrides, transition metal dichalcogenides (TMDs) have also been widely explored as electrocatalytic materials, especially MoS_2.[87,99,100] Although, MoS_2 was found to be a good catalytic material for water reduction, it does not show any activity toward the other water oxidation half-cell. In this respect, many researchers focused to develop OER-active TMDs or bifunctional TMDs by introducing other transition metal dichalcogenides (Fe, Co, and Ni). Recently, Yang and co-workers have successfully achieved the FeNi sulfide ultrathin nanosheets from FeNi LDH precursors which showed exceptionally high HER performance in acidic medium.[101] Apart from this, various types of OER-active bimetallic sulfides are also successfully fabricated from LDH precursors.[102] In recent past, a number of LDH-derived nickel selenides are also developed and demonstrated to be robust bifunctional alkaline water electrocatalytic materials.[94,86,103]

1.11. Objectives of the present work

Based on the above discussion, energy-efficient and water-sourced hydrogen generation can be considered as one of the essential breakthroughs toward shaping the sustainable energy future. However, one of the major roadblocks toward this hydrocarbon to hydrogen economy transition is the sluggish kinetics of the involved water splitting reactions. To combat this hurdle, various precious and non-precious group-metal based catalysts have been developed. Among which, the layered double hydroxides have emerged as promising candidates for designing various functional materials in a cost-effective and eco-friendly manner. In line with this, the present thesis aims to contribute toward the energy-efficient and water-sourced hydrogen production. To realize it, our scope of research involves the physicochemical property tuning of LDHs to design

robust electrocatalytic materials as well as introducing novel and less energy-intensive pathways for low-cost H_2 generation.

1.12. Organization of the present thesis

The scope and aim of the present thesis is broadly illustrated in the second to fifth chapters narrating our approach to the synthesis and property tuning of LDH toward catalyzing various electrochemical reactions involved in the cost-effective hydrogen generation. The working chapters are broadly categorized in two sections. The first section comprises initial two working chapters with the special focus on the replacement of noble-metal-based water electrolyzing catalysts with low-cost, earth abundant metal-based robust catalyst systems. The major outcomes of these two chapters are to contribute toward reducing the H_2 producing station installation cost. The other two working chapters build another section which focuses to reduce the energy expense for generating hydrogen from water by replacing the water oxidation half-cell with readily oxidizable species. The last chapter of the thesis includes the summery of the research work performed in the above-mentioned four working chapters along with the future outline.

Chapter 2 focuses only on catalysing the water oxidation half-cell since the overall energy efficiency of water-sourced H_2 generation is controlled by this half-cell. With this work, our aim is to replace the high-cost, scarce-metal-based catalysts with readily available active metals. The work discusses a single-step solvothermal process to synthesize an active electrocatalyst for water oxidation reaction (WOR) in alkaline medium. The adopted synthesis strategy results into the anchoring of ϒ-NiOOH phase-enriched NiZn double hydroxide nanosheets over N-doped graphene. The designed catalyst possesses thin, porous and open layered structure, which makes the system more efficient and accessible for the better water oxidation potential. Moreover, we experimentally demonstrated that the incorporation of Zn provides an easy approach to get plenty of exposed ϒ-NiOOH phase to make the system viable for WOR with a small overpotential of ~290 mV at 10 mA cm^{-2} and a Tafel slope of ~44 mV decade^{-1}. In addition to that, oxophilic nature of Zn assisted to improve the long-term stability of the catalyst system.

Chapter 3 illustrates our work targeted to reducing the electrolyzer installation cost both by utilizing low-cost active metals as well as by eliminating the cost of designing two different materials. The work introduces a self-templating method for the design of a porous, edge-site-rich hybrid nanomaterial *via* the selective etching of layered double hydroxide precursors that

contain an amphoteric metal by alkali treatment followed by vapour phase selenization. The obtained hexagonal nickel selenide nanoplates anchored over nitrogen-doped graphene showed highly efficient and robust WOR electrocatalysis. It demonstrates a low overpotential of ~311 mV to achieve the benchmark 10 mA cm^{-2} water oxidation current density in 1 M KOH. When we fabricated an alkaline water electrolyzer, it enabled high-performing overall water splitting with a low overpotential of 460 mV from the theoretical voltage of 1.23 V to generate sufficient amounts of H$_2$ and O$_2$ by achieving a current density of 10 mA cm^{-2}. The catalyst has also displayed outstanding electrochemical stability toward all the employed reactions.

Chapter 4 aims to further reduce the energy required for H$_2$ generation from water, and hence to contribute toward reducing the per kg H$_2$ cost. This chapter describes a strategy of substituting the energy-uphill water oxidation half-cell with readily oxidizable urea-rich urine to construct a ground-breaking bridge, combining the energy-efficient hydrogen generation and environmental protection. However, designing of a robust multifunctional electrocatalyst is desirable for the widespread implementation of this waste to fuel technology. In this context, here, we propose a simple tuning of the electrocatalytically favorable characteristics of NiCo layered double hydroxide by introducing [MoS$_4$]$^{2-}$ in its interlayer space. The [MoS$_4$]$^{2-}$ insertion as well as its effect on the electronic structure tuning is thoroughly studied *via* X-ray photoelectron spectroscopy in combination with electrochemical analysis. This insertion induced overall electronic structure tuning of the hydroxide layer is achieved in such a way that, the designed catalyst exhibited favorable kinetics toward all the required reactions of hydrogen generation. This is why, our homemade catalyst, when utilized both as a cathode and anode to fabricate a urea electrolyzer, it required a mere ~1.37 V cell potential to generate sufficient H$_2$ by reaching the benchmark 10 mA cm^{-2} in 1 M KOH/0.33 M urea along with long-lasting catalytic efficiency. Other indispensable reason of selecting [MoS$_4$]$^{2-}$ is its high-valent nature making the catalyst highly selective and insensitive to common catalyst-poisoning toxins of urine. This is experimentally supported by performing the real urine electrolysis, where the nanospike-covered Ni foam-based catalyst showed similar performance to that of the synthetic urea, offering its industrial value.

Chapter 5 not only accounts to replace the energy-consuming water oxidation half-cell with readily oxidizable metals but also to generate electricity. The motivation of this work got originated while testing a home-made metal-air battery which involves oxidation of an

electropositive metal on the anode and reduction of O_2 from air on the cathode. The cell thus theoretically generates 2.71 V. While performing the test, accidently we pumped N_2 in place of O_2, and found that even in absence of O_2, the circuit is completed and some voltage is generating. And, with the support of literatures as well as experiments, we found that in absence of O_2, water gets reduced and liberates H_2. Hence, in this chapter we propose the fabrication and demonstration of a dual-mode Al-based battery to generate H_2 and electricity simultaneously. However, to improve the overall energy-efficiency of the device, development of a robust bifunctional catalyst is required, which can catalyze both O_2 Reduction Reaction (ORR) as well as H_2O reduction reaction (Hydrogen Evolution Reaction, HER). Taking this into account, here we tuned the LDH property and synthesized a bifunctional Co@CoAl-LDH/NGr electrocatalyst to catalyze both ORR and HER. The designed catalyst was characterized properly by employing various material characterization techniques, *e.g.,* X-ray diffraction analysis, high-resolution transmission electron microscopy, X-ray photoelectron spectroscopy, etc. The homemade catalyst when employed as the cathode both in presence and absence of O_2, it worked quite efficiently and performed comparable to the commercial Pt-based catalyst. At a discharge current density of -10 mA cm^{-2}, the catalyst exhibited an average voltage of 0.93 V and 0.79 V in presence and absence of O_2, respectively. The H_2 generated was quantified with gas chromatography.

1.13. References

1   K. W. A. Guy, *Process Saf. Environ. Prot.*, 2000, **78**, 324–327.
2   J. O. Bockris, *Science*, 1972, **176**, 1323.
3   *HYDROGEN PRODUCTION IN INDIA Sub-Committee on Research, Development & Demonstration for Hydrogen Energy and Fuel Cells Steering Committee on Hydrogen Energy and Fuel Cells Ministry of New and Renewable Energy, Government of India, New Delhi*, 2016.
4   B. Obama, *Science,* 2017, **355**, 126–129.
5   I. Staffell, D. Scamman, A. V. Abad, P. Balcombe, P. E. Dodds, P. Ekins, N. Shah and K. R. Ward, *Energy Environ. Sci.*, 2018, **12**, 463–491.
6   AR5 Climate Change 2013: The Physical Science Basis — IPCC, https://www.ipcc.ch/report/ar5/wg1/, (accessed 24 September 2019).
7   Z. W. She, J. Kibsgaard, C. F. Dickens, I. Chorkendorff, J. K. Nørskov and T. F. Jaramillo, *Science,* 2017, **355**, 146–157.
8,   J. A. Turner, *Science*, 2004, **305**, 972–974.
9   The Mysterious Island by Jules Verne. Search eText, Read Online, Study, Discuss., http://www.online-literature.com/verne/mysteriousisland/, (accessed 5 August 2019).
10   P. Hoffmann, *The forever fuel : the story of hydrogen /*, Westview Press, Boulder, Colo. :, 1981.
11   K. W. A. Guy, *Process Saf. Environ. Prot.*, 2000, **78**, 324–327.
12   J. O. Bockris, *Science*, 1972, **176**, 1323.
13   The truth about hydrogen, the latest, trendiest low-carbon solution | GreenBiz, https://www.greenbiz.com/article/truth-about-hydrogen-latest-trendiest-low-carbon-solution, (accessed 24 September 2019).
14   E. G. Brown, *California Energy Commission California Air Resources Board Joint Agency Staff Report on Assembly Bill 8: Assessment of Time and Cost Needed to Attain 100 Hydrogen Refueling Stations in California*, .

15   M. V. C. Sastri, *Int. J. Hydrogen Energy*, 1989, **14**, 507–513.

16   Hydrogen Energy in India | Production techniques and Government policies on Hydrogen energy.- Energy Alternatives India - EAI.in, http://www.eai.in/ref/ae/hyn/hyn.html, (accessed 8 August 2019).

17   A. A. Ismail and D. W. Bahnemann, *Sol. Energy Mater. Sol. Cells*, 2014.

18   Water Splitting - an overview (pdf) | ScienceDirect Topics, https://www.sciencedirect.com/topics/materials-science/water-splitting/pdf, (accessed 6 August 2019).

19   Hydrogen Production: Thermochemical Water Splitting | Department of Energy, https://www.energy.gov/eere/fuelcells/hydrogen-production-thermochemical-water-splitting, (accessed 6 August 2019).

20   Hydrogen Production: Electrolysis | Department of Energy, https://www.energy.gov/eere/fuelcells/hydrogen-production-electrolysis, (accessed 24 September 2019).

21   N. T. Suen, S. F. Hung, Q. Quan, N. Zhang, Y. J. Xu and H. M. Chen, *Chem. Soc. Rev.*, 2017, **46**, 337–365.

22   J. Durst, A. Siebel, C. Simon, F. Hasché, J. Herranz and H. A. Gasteiger, *Energy Environ. Sci.*, 2014, **7**, 2255–2260.

23   Y. Yan, B. Y. Xia, B. Zhao and X. Wang, *J. Mater. Chem. A*, 2016, **4**, 17587–17603.

24   M. I. Jamesh, *J. Power Sources*, 2016, 333, 213–236.

25   R. Subbaraman, D. Tripkovic, D. Strmcnik, K. C. Chang, M. Uchimura, A. P. Paulikas, V. Stamenkovic and N. M. Markovic, *Science*, 2011, **334**, 1256–1260.

26   Z. Liang, H. S. Ahn and A. J. Bard, *J. Am. Chem. Soc.*, 2017, **139**, 4854–4858.

27   Z. Cai, X. Bu, P. Wang, J. C. Ho, J. Yang and X. Wang, *J. Mater. Chem. A*, 2019, **7**, 5069–5089.

28   Y. Wang, D. Yan, S. El Hankari, Y. Zou and S. Wang, *Adv. Sci.*, 2018, **5**, 1800064–1800096.

29   M. Shao, R. Zhang, Z. Li, M. Wei, D. G. Evans and X. Duan, *Chem. Commun.*, 2015, **51**, 15880–15893.

30   B. K. Boggs, R. L. King and G. G. Botte, *Chem. Commun.*, 2009, 4859–4861.

31   A. Nadeema, V. Kashyap, R. Gururaj and S. Kurungot, *ACS Appl. Mater. Interfaces*, 2019, **11**, 25917–25927.

32   J. Jiang, M. Chang and P. Pan, *Environ. Sci. Technol.*, 2008, **42**, 3059–3063.

33   M. Cataldo Hernández, N. Russo, M. Panizza, P. Spinelli and D. Fino, *Diam. Relat. Mater.*, 2014, **44**, 109–116.

34   T. Take, K. Tsurutani and M. Umeda, *J. Power Sources*, 2007, **164**, 9–16.

35   J. Y. Zhang, X. Tian, T. He, S. Zaman, M. Miao, Y. Yan, K. Qi, Z. Dong, H. Liu and B. Y. Xia, *J. Mater. Chem. A*, 2018, **6**, 15653–15658.

36   S. Möhle, M. Zirbes, E. Rodrigo, T. Gieshoff, A. Wiebe and S. R. Waldvogel, *Angew. Chemie Int. Ed.*, 2018, **57**, 6018–6041.

37   Y. Huang, X. Chong, C. Liu, Y. Liang and B. Zhang, *Angew. Chemie - Int. Ed.*, 2018, **57**, 13163–13166.

38   Z. Guo, Y. Wang, Y. Song, C. Li, X. Su, Y. Wang, W. Bin Cai and Y. Xia, *ACS Energy Lett.*, 2017, **2**, 36–44.

39   P. Cai, Y. Li, G. Wang and Z. Wen, *Angew. Chemie - Int. Ed.*, 2018, **57**, 3910–3915.

40   G. Fan, F. Li, D. G. Evans and X. Duan, *Chem. Soc. Rev.*, 2014, **43**, 7040–7066.

41   R. M. M. Santos, J. Tronto, V. Briois and C. V. Santilli, *J. Mater. Chem. A*, 2017, **5**, 9998–10009.

42   K. Fan, H. Chen, Y. Ji, H. Huang, P. M. Claesson, Q. Daniel, B. Philippe, H. Rensmo, F. Li, Y. Luo and L. Sun, *Nat. Commun.*, 2016, **7**, 11981–11990.

43   Z. Zhao, H. Wu, H. He, X. Xu and Y. Jin, *Adv. Funct. Mater.*, 2014, **24**, 4698–4705.

44   X. Long, S. Xiao, Z. Wang, X. Zheng and S. Yang, *Chem. Commun.*, 2015, **51**, 1120–1123.

45   H. Liu, Y. Wang, X. Lu, Y. Hu, G. Zhu, R. Chen, L. Ma, H. Zhu, Z. Tie, J. Liu and Z. Jin, *Nano Energy*, 2017, **35**, 350–357.

46   A.-L. Wang, H. Xu and G.-R. Li, *ACS Energy Lett.*, 2016, **1**, 445–453.

47   A. Guzmán-Vargas, J. Vazquez-Samperio, M. A. Oliver-Tolentino, N. Nava, N. Castillo, M. J. Macías-Hernández and E. Reguera, *J. Mater. Sci.*, 2018, **53**, 4515–4526.

48   Z. Lu, L. Qian, Y. Tian, Y. Li, X. Sun and X. Duan, *Chem. Commun.*, 2016, **52**, 908–911.

49   B. M. Hunter, J. D. Blakemore, M. Deimund, H. B. Gray, J. R. Winkler and A. M. Müller, *J. Am. Chem. Soc.*, 2014, **136**, 13118–13121.

50   X. Long, J. Li, S. Xiao, K. Yan, Z. Wang, H. Chen and S. Yang, *Angew. Chemie Int. Ed.*, 2014, **53**, 7584–7588.

51   D. Zhou, Z. Cai, Y. Bi, W. Tian, M. Luo, Q. Zhang, Q. Xie, J. Wang, Y. Li, Y. Kuang, X. Duan, M. Bajdich, S. Siahrostami and X. Sun, *Nano Res.*, 2018, **11**, 1358–1368.

52   B. M. Hunter, W. Hieringer, J. R. Winkler, H. B. Gray and A. M. Müller, *Energy Environ. Sci.*, 2016, **9**, 1734–1743.

53   M. Zeng, J. Wu, Z. Li, H. Wu, J. Wang, H. Wang, L. He and X. Yang, *ACS Sustain. Chem. Eng.*, 2019, **7**, 4777–4783.

54   X. Li, X. Hao, Z. Wang, A. Abudula and G. Guan, *J. Power Sources*, 2017, **347**, 193–200.

55   Y. Sun, S. Gao, F. Lei and Y. Xie, *Chem. Soc. Rev.*, 2015, **44**, 623–636.

56   Y. Sun, Z. Sun, S. Gao, H. Cheng, Q. Liu, F. Lei, S. Wei and Y. Xie, *Adv. Energy Mater.*, 2014, **4**, 1300611.

57   C. Xia, H. Liang, J. Zhu, U. Schwingenschlögl and H. N. Alshareef, *Adv. Energy Mater.*, 2017, **7**, 1602089.

58   F. Song and X. Hu, *Nat. Commun.*, 2014, **5**, 4477–4486.

59   Y. Wang, Y. Zhang, Z. Liu, C. Xie, S. Feng, D. Liu, M. Shao and S. Wang, *Angew. Chemie Int. Ed.*, 2017, **56**, 5867–5871.

60   J. Woo, S. Y. Yang, Y. J. Sa, W. Y. Choi, M. H. Lee, H. W. Lee, T. J. Shin, T. Y. Kim and S. H. Joo, *Chem. Mater.*, 2018, **30**, 6684-6701.

61   R. Liu, Y. Wang, D. Liu, Y. Zou and S. Wang, *Adv. Mater.*, 2017, **29**, 1701546.

62   Y. Wang, M. Qiao, Y. Li and S. Wang, *Small*, 2018, **14**, 1800136.

63   Y. Zhao, X. Zhang, X. Jia, G. I. N. Waterhouse, R. Shi, X. Zhang, F. Zhan, Y. Tao, L.-Z. Wu, C.-H. Tung, D. O'Hare and T. Zhang, *Adv. Energy Mater.*, 2018, **8**, 1703585.

64   J. Wang, W. Cui, Q. Liu, Z. Xing, A. M. Asiri and X. Sun, *Adv. Mater.*, 2016, **28**, 215–230.

65   A. Bergmann, E. Martinez-Moreno, D. Teschner, P. Chernev, M. Gliech, J. F. de Araújo, T. Reier, H. Dau and P. Strasser, *Nat. Commun.*, 2015, **6**, 8625.

66   D. Zhou, X. Xiong, Z. Cai, N. Han, Y. Jia, Q. Xie, X. Duan, T. Xie, X. Zheng, X. Sun and X. Duan, *Small Methods*, 2018, **2**, 1800083.

67   Y. Zhao, X. Jia, G. Chen, L. Shang, G. I. N. Waterhouse, L.-Z. Wu, C.-H. Tung, D. O'Hare and T. Zhang, *J. Am. Chem. Soc.*, 2016, **138**, 6517–6524.

68   L. Zhuang, L. Ge, Y. Yang, M. Li, Y. Jia, X. Yao and Z. Zhu, *Adv. Mater.*, 2017, **29**, 1606793.

69   W. Cheng, H. Zhang, X. Zhao, H. Su, F. Tang, J. Tian and Q. Liu, *J. Mater. Chem. A*, 2018, **6**, 9420–9427.

70   P. F. Liu, S. Yang, B. Zhang and H. G. Yang, *ACS Appl. Mater. Interfaces*, 2016, **8**, 34474–34481.

71   D. Tang, Y. Han, W. Ji, S. Qiao, X. Zhou, R. Liu, X. Han, H. Huang, Y. Liu and Z. Kang, *Dalt. Trans.*, 2014, **43**, 15119–15125.

72   J. Xu, S. Gai, F. He, N. Niu, P. Gao, Y. Chen and P. Yang, *J. Mater. Chem. A*, 2014, **2**, 1022–1031.

73   X. Wu, L. Jiang, C. Long, T. Wei and Z. Fan, *Adv. Funct. Mater.*, 2015, **25**, 1648–1655.

74   X. Li, J. Shen, W. Sun, X. Hong, R. Wang, X. Zhao and X. Yan, *J. Mater. Chem. A*, 2015, **3**, 13244–13253.

75   B. Yang, Z. Yang, R. Wang and T. Wang, *Electrochim. Acta*, 2013, **111**, 581–587.

76   Y. Wang, Z. Wang, Y. Rui and M. Li, *Biosens. Bioelectron.*, 2015, **64**, 57–62.

77   D. Tang, J. Liu, X. Wu, R. Liu, X. Han, Y. Han, H. Huang, Y. Liu and Z. Kang, *ACS Appl. Mater. Interfaces*, 2014, **6**, 7918–7925.

78   L. Qu, Y. Liu, J.-B. Baek and L. Dai, *ACS Nano*, 2010, **4**, 1321–1326.

79   Z. Gao, J. Wang, Z. Li, W. Yang, B. Wang, M. Hou, Y. He, Q. Liu, T. Mann, P. Yang, M. Zhang and L. Liu, *Chem. Mater.*, 2011, **23**, 3509–3516.

80   L. Zhang, X. Zhang, L. Shen, B. Gao, L. Hao, X. Lu, F. Zhang, B. Ding and C. Yuan, *J. Power Sources*, 2012, **199**, 395–401.

81   A. Nadeema, V. M. Dhavale and S. Kurungot, *Nanoscale*, 2017, **9**, 12590–12600.

82   A. Nadeema, P. S. Walko, R. N. Devi and S. Kurungot, *ACS Appl. Energy Mater.*, 2018, **1**, 5500–5510.

83   L. Wang, D. Wang, X. Y. Dong, Z. J. Zhang, X. F. Pei, X. J. Chen, B. Chen and J. Jin, *Chem. Commun.*, 2011, **47**, 3556.

84   M. Gong, Y. Li, H. Wang, Y. Liang, J. Z. Wu, J. Zhou, J. Wang, T. Regier, F. Wei and H. Dai, *J. Am. Chem. Soc.*, 2013, **135**, 8452–8455.

85   H. Li, Z. Kang, Y. Liu and S.-T. Lee, *J. Mater. Chem.*, 2012, **22**, 24230.

86   Y.-P. Sun, B. Zhou, Y. Lin, W. Wang, K. S. Fernando, P. Pathak, M. J. Meziani, B. A. Harruff, X. Wang, H. Wang, *J. Am. Chem. Soc,* 2006, **128**, 7756–7757.

87   T. F. Jaramillo, K. P. Jorgensen, J. Bonde, J. H. Nielsen, S. Horch and I. Chorkendorff, *Science*, 2007, **317**, 100–102.

88   Y. Zhang, Q. Shao, Y. Pi, J. Guo and X. Huang, *Small*, 2017, **13**, 1700355.

89   X. Long, Z. Wang, S. Xiao, Y. An and S. Yang, *Mater. Today*, 2015, **19**, 213–226.

90   J. Xie, X. Zhang, H. Zhang, J. Zhang, S. Li, R. Wang, B. Pan and Y. Xie, *Adv. Mater.*, 2017, **29**, 1604765.

91   H. Liang, L. Li, F. Meng, L. Dang, J. Zhuo, A. Forticaux, Z. Wang and S. Jin, *Chem. Mater.*, 2015, **27**, 5702–5711.

92   C. Tang, R. Zhang, W. Lu, L. He, X. Jiang, A. M. Asiri and X. Sun, *Adv. Mater.*, 2017, **29**, 1602441.

93   B. Zhang, Y. H. Lui, H. Ni and S. Hu, *Nano Energy*, 2017, **38**, 553–560.

94   K. Xu, P. Chen, X. Li, Y. Tong, H. Ding, X. Wu, W. Chu, Z. Peng, C. Wu and Y. Xie, *J. Am. Chem. Soc.*, 2015, **137**, 4119–4125.

95   X. Jia, Y. Zhao, G. Chen, L. Shang, R. Shi, X. Kang, G. I. N. Waterhouse, L.-Z. Wu, C.-H. Tung and T. Zhang, *Adv. Energy Mater.*, 2016, **6**, 1502585.

96   J. Xie, H. Zhang, S. Li, R. Wang, X. Sun, M. Zhou, J. Zhou, X. W. D. Lou and Y. Xie, *Adv. Mater.*, 2013, **25**, 5807–5813.

98   Y. Li, H. Wang, L. Xie, Y. Liang, G. Hong and H. Dai, *J. Am. Chem. Soc.*, 2011, **133**, 7296–7299.

99   J. Hu, C. Zhang, L. Jiang, H. Lin, Y. An, D. Zhou, M. K. H. Leung and S. Yang, *Joule*, 2017, **1**, 383–393.

100   X. Long, G. Li, Z. Wang, H. Zhu, T. Zhang, S. Xiao, W. Guo and S. Yang, *J. Am. Chem. Soc.,* 2015, 137, 11900-11903.

101   Z. Fang, L. Peng, H. Lv, Y. Zhu, C. Yan, S. Wang, P. Kalyani, X. Wu and G. Yu, *ACS Nano*, 2017, **11**, 9550–9557.

Chapter 2

ϒ-NiOOH-Enriched NiZn Double Hydroxide Nanosheets/ Nitrogen-Doped Graphene Composite for Catalysing the Water Oxidation Half-Cell*

This chapter focuses on catalyzing the water oxidation half-cell since it controls the overall energy efficiency of the water-sourced H_2 generation. With this work, our aim is to replace the high-cost, scarce-metal-based catalysts with readily available active metals. The work discusses a single-step solvothermal process to synthesize an active electrocatalyst for water oxidation reaction (WOR) in alkaline medium. The adopted synthesis strategy results into the anchoring of the ϒ-NiOOH phase-enriched NiZn double hydroxide nanosheets over N-doped graphene. The designed catalyst possesses thin, porous and open layered structure, which makes the system more efficient and accessible for the better
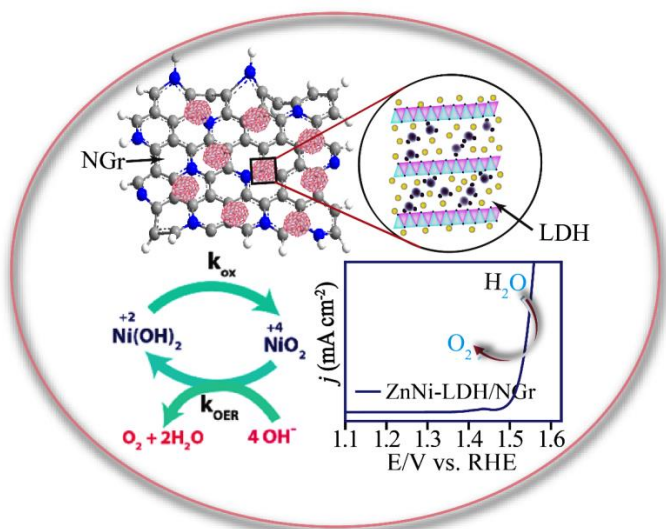
water oxidation potential. Moreover, we experimentally demonstrated that the incorporation of Zn provides an easy approach to get plenty of exposed ϒ-NiOOH phase to make the system more viable for WOR exhibiting a small overpotential of ~290 mV at 10 mA cm^{-2} and a Tafel slope of ~44 mV decade^{-1}. In addition to that, the oxophilic nature of Zn assisted to improve the catalytic stability of the designed system.

2.1.   Introduction

In view of the ever increasing demand for the sustainable energy colonies, there has been a growing thrust on the developing of efficient renewable energy-based devices such as fuel cells and metal-air batteries.[1,2] However, the available technologies need improvement on bridging the still existing gaps between the theoretical and practically achievable efficiencies of these systems.[2,3] On one hand, the hydrogen fuel cell sustainability depends upon the source of hydrogen, and the water oxidation (oxygen evolution reaction, OER) remains the bottleneck to provide energy-efficient water-sourced hydrogen.[1] And, on the other hand, the reversibility as well as the overall energy efficiency of the metal-air battery is largely governed by the kinetics of OER.[4,5] Unfortunately, OER is a multistep proton coupled electron transfer reaction involving the formation of O–O double bond, which makes it more complicated and results into sluggish kinetics.[6] In view of this, development of efficient water oxidation electrocatalysts (WOE) is of paramount importance. Even though oxides of iridium and ruthenium are considered to be the most efficient WOEs, their widespread applications are limited by their high cost and scarcity.[7] To circumvent this issue, a new strategy has been evolved to develop potential oxygen evolution electrocatalysts (OECs) by exploring the earth-abundant materials, especially 3d transition metals with promising activity, diversity and potential stability.

Among the various 3d transition metals, nickel-based materials have been widely investigated as remarkably worthwhile candidates for developing alternative WOEs by virtue of their great availability, low cost, high corrosion resistance, unique redox characteristics and better water oxidation potential.[8-11] In this context, significantly high performance has already been reported over oxides, hydroxides (double hydroxides), mixed metal oxides and alloys of Ni.[12-14] Very recently, it has been proven that, in almost all kind of OER catalysts, the active metal phases are either layered hydroxides, *e.g.,* α-Ni(OH)$_2$, or oxy-hydroxides, *e.g.,* ϒ-NiOOH.[14,15] These active phases are well preserved in layered double hydroxides (LDHs) and the presence of intercalated anions and water provided the favorable open structure to the system.[1,16] These unique characteristics ensure structural stability by effectively preventing structural rearrangements during the electrochemical conditions and concomitantly providing better accessibility of the

reaction components and electrolyte.[16] Irrespective of all these advantages, these NiM-LDHs suffer from low electrical conductivity, a common problem of the hydroxides, limiting their overall performance.[16] This electrical conductivity issue, however, can be practically overcome either by hybridizing NiM-LDHs with a conductive carbon material or by directly growing them on a conductive substrate.

Among all the NiM-double hydroxides, NiFe-LDHs achieved significant attention due to their outstanding performance.[1] However, their widespread application suffer from the complex preparation methods, which mainly originates from the huge solubility product difference between the two metal moieties (Ni(OH)$_2$, K_{sp} = 5.5*10^{-16} and Fe(OH)$_3$, K_{sp} = 2.8*10^{-39}). On the other hand, both Ni and Zn exhibit nearly same solubility product values (Zn(OH)$_2$, K_{sp} = 1.2*10^{-17}), which provide a way for easy and large-scale synthesis of NiZn-double hydroxides to achieve low cost and potentially active OER catalysts. Additionally, a number of reports are available highlighting the stabilization of the specific Ni phases with a particular Ni/Zn ratio in alkaline medium, which aids to improve its electrochemical activity as well as stability.[17,18] Moreover, owing to its oxophilic nature, Zn may help for better adsorption of the reactants as well as easy detachment of the OER product (O$_2$), thereby cleaning the active centres to enhance the catalyst life during the operating conditions.[19,20] Hence, in the quest for developing a cost-effective electrocatalyst with enhanced oxygen evolution activity, herein, we describe a simple strategy to populate OER-active ɤ-NiOOH phase with enhanced stability by doping Zn^{2+} ions in the layered α-Ni(OH)$_2$ crystal structure. This mainly resulted into the synthesis of amorphous NiZn-double hydroxide phases isostructural with α-Ni(OH)$_2$.[21] Taking advantage of the enriched C–N bonds present in N-doped graphene (NGr), electrical conductivity as well as activity of the above system was further tuned by clubbing it with NGr and the catalyst is abbreviated as ZnNi-LDH/NGr in all the upcoming sections.

2.2. Experimental section

2.2.1. Synthesis of graphene oxide and reduced graphene oxide: Graphene oxide (GO) was synthesized by following an improved Hummer's method[21] from natural graphite by giving it harsh oxidizing treatment. For the synthesis of reduced graphene oxide (rGO),

GO flakes were kept into a quartz tube for annealing at 900 ^{o}C in a tubular furnace under argon atmosphere. For the required reduction of GO to rGO, the furnace temperature was maintained for 3 h. In the subsequent process, the furnace was cooled down naturally under the same atmosphere.

2.2.2. Synthesis of N-doped graphene (NGr): 1 g of graphene oxide (GO) was dissolved in adequate DI water by water-bath sonication and overnight stirring. Subsequently, melamine was added in the ratio of 1:5 into the GO-DI water solution and the mixture was continued for 24 h stirring; after that the mixture was heated at 80 ^{o}C with stirring until it was dried completely. The dried GO-melamine powder was subjected for heating at 900 ^{o}C for 3 h under argon atmosphere. Thereafter, the furnace was allowed to cool down naturally in the same atmosphere and NGr was collected.

2.2.3. Synthesis of ZnNi-LDH/NGr: For the synthesis of ZnNi-LDH/NGr, $NiCl_2 \cdot 6H_2O$ and $Zn(CH_3OO)_2 \cdot 2H_2O$ (with a molar ratio of Ni/Zn = 3:1) were first dissolved in methanol and DI-water (3:2) mixture and subsequently urea was added in a molar ratio of 1:5 of the metal ions to urea. Afterward, the as-synthesized NGr was added to the above solution in 1:4 ratio of the metal ions to carbon. After dispersing *via* bath sonication, the mixture was transferred into a 200 mL Teflon lined stainless steel autoclave and heated at 170 ^{o}C for 12 h. Finally, the synthesized sample was washed 3–4 times by centrifugation (at 10,000 rpm for 10 min) using methanol-water mixture and finally the sample was dried at 150 ^{o}C for 12 h. Scheme 1 embodies the elucidation of the processes involved in the synthesis of ZnNi-LDH/NGr electrocatalyst.

2.2.4. Synthesis of NiZn(OH)$_x$/rGO: This sample was prepared by following the same procedure as it was adopted for synthesizing ZnNi-LDH/NGr catalyst just by replacing NGr with rGO.

2.2.5. Synthesis of α-Ni(OH)$_x$/NGr: α-Ni(OH)$_x$/N-rGO was prepared by following the same procedure as it was adopted for synthesizing ZnNi-LDH/NGr without adding the Zn salt and by keeping the urea to metal ions ratio and NGr to metal ions ratio same as it was maintained for synthesizing ZnNi-LDH/NGr.

2.2.6. Synthesis of ZnO/NGr: This sample was prepared by following the same procedure as it was used for ZnNi-LDH/NGr without using any nickel salt.
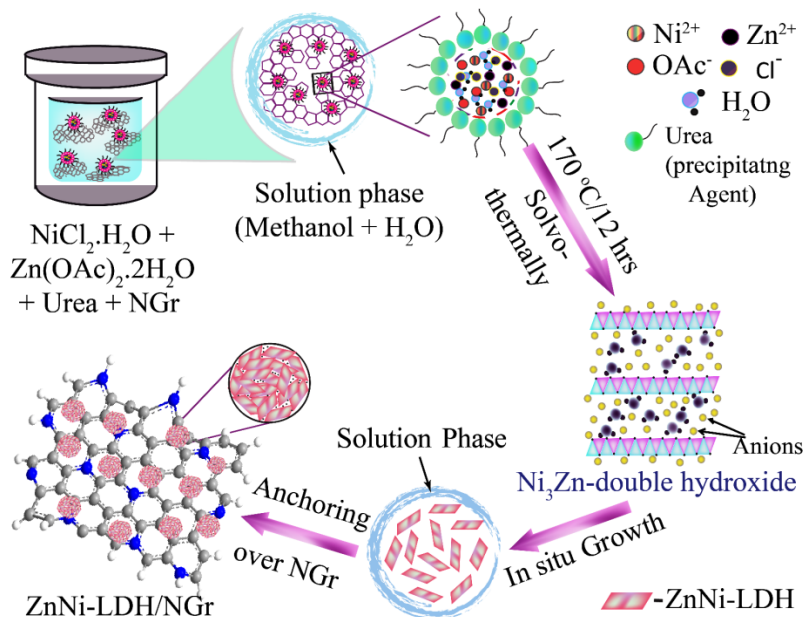
Scheme 1: Schematic illustration of the steps involved in the synthesis of ZnNi-LDH/NGr electrocatalyst by a simple solvothermal method.

2.3. Results and discussion

2.3.1. Structure and morphology of the catalyst

Scheme 1 illustrates the various steps involved in the phase controlled, urea-assisted *in-situ* growth and deposition of ZnNi-LDH nanosheets over NGr (ZnNi-LDH/NGr). Herein, the present work, we specifically adopted the urea-assisted LDH synthesis method since urea has a number of properties which make its use as a precipitating agent much more attractive.[22] The advantage of thermally controlled hydrolysis of urea against sodium hydroxide induces homogenous nucleation and crystallization of the LDH material without any phase separation, leading to the product with good uniformity and crystallinity.[23] NGr with its mesoporous framework and moderate defective sites along with N-doping, make the surface fertile enough to facilitate the adsorption and anchoring of the metal ions. During the precipitation process, the nucleation and growth of ZnNi-LDH nanosheets were not only confined over the NGr framework but also grew in between the sheets of NGr. Additionally, the *in-situ* growth of ZnNi-LDH flakes over the porous and defective region of the NGr scaffold drastically decreases the amount of the

micro as well as mesopores sharing a size range of 1 to 3 nm possessed by the substrate (Figure 1a and Figure 1b). At the same time, the hybrid system acquires mesopores in the pore size range of 3.5 to 25 nm, which is attributed to the formation as well as insertion of ZnNi-LDHs in between the NGr sheets. This architectural fine tuning makes the system highly porous and open, thereby assisting the active sites to be well accessible by the reactants.
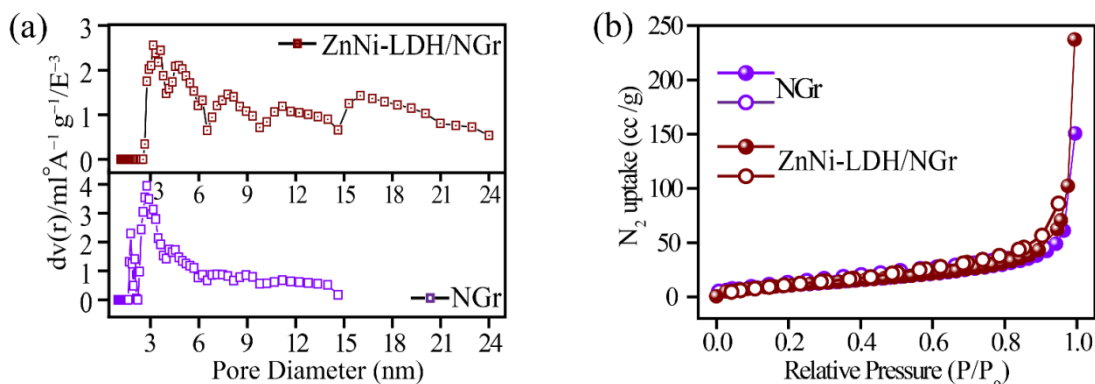

Figure 1: Comparative BET analysis for NGr and ZnNi-LDH/NGr: (a) pore size distribution profile and (b) N_2 adsorption-desorption isotherms.

2.3.1.1. X-ray diffraction analysis

The formation of the well-crystallized ZnNi-LDH/NGr with a set of hydrotalcite-like characteristic (00n) peaks is well indexed in the comparative powder X-ray diffraction (PXRD) patterns (Figure 2). All the LDH-characteristic diffraction peaks with the 2Θ values of 11°, 23°, 34° and 59° corresponding to the (003), (006), (101) and (110) planes, are matching well with the JCPDS Card No. 38-0715 (Figure 2a). [24-26] These peaks confirm the formation of a pure hexagonal α/ϒ Ni-phase, constructed from $[NiO_6]$ co-ordinated octahedra which are connected by sharing their edges.[24-28] PXRD patterns of both ZnNi-LDH/NGr and NGr give a (002) diffraction peak corresponding to the graphitic plane at a 2Θ value of 26.53^o, confirming the successful growth of ZnNi-LDH over NGr during the course of the reaction (Figure 2a).[29] Interlayer spacing of LDH was determined based on the (003) reflection position and for ZnNi-LDH/NGr, the *d*-spacing value was estimated to be 8 Å. Asymmetric nature of the (101) diffraction peak indicated the formation of turbostratic LDH phase (inset of Figure 2a).[1,30] This turbostratic structure

having water as 'amorphous glue' holds the adjacent metal hydroxide layers and provides open structure which helps for the facile intercalation as well as anion exchange to tailor their activity for various applications.[30] Moreover, open structure with intercalated water molecules provides better mass transport as well as good wettability for improved electrocatalysis.
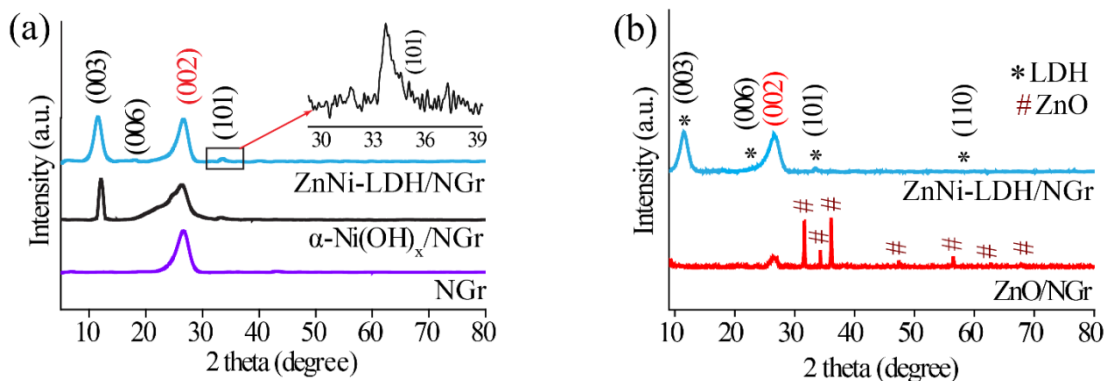

Figure 2: Comparative PXRD patterns: (a) ZnNi-LDH/NGr, α-Ni(OH)$_x$/NGr and NGr, (b) ZnNi-LDH/NGr and ZnO/NGr.

The peak broadening of the (003) diffraction plane infers to a lesser number of the layers in the ZnNi-LDH/NGr as compared to α-Ni(OH)$_x$/NGr, which is a highly desirable characteristics for accomplishing better OER activity (Figure 2a).[31,32] Comparative PXRD patterns of ZnO/N-rGO and ZnNi-LDH/NGr are presented in Figure 2b, which, in the absence of Ni shows the diffraction peaks corresponding to ZnO.[33] Considering the fact that the ZnO phase is absent in ZnNi-LDH/NGr, this result infers the mutual interaction between Ni and Zn towards the synthesized layered double hydroxide with no phase separation. In this way, PXRD pattern of our catalysts confirmed the pivotal role played by Zn to stabilize its counterpart Ni in its higher oxidation state (Ni^{3+} or Υ-NiOOH), leading to the successful formation of the layered double hydroxide structure.

2.3.1.2. Raman analysis

Subsequent to the phase identification of ZnNi-LDH/NGr through PXRD, Raman spectral investigation has been performed to characterize the crystallinity, defects and disorderness in the microstructures of GO, NGr and ZnNi-LDH/NGr (Figure 3a). The spectrum of each sample in the present case displays two main peaks in the range of 1300

and 1600 cm^{-1} due to the lattice distortion which is created by the stokes phonon energy shift caused by laser excitation.[34] The band near 1320 cm^{-1} could be assigned to the defective or partially disordered (D-band) nature of the carbon which includes bonding disorder, vacancies and heteroatom doping in the graphene lattice. The band at around 1580–1600 cm^{-1} could be ascribed to the G-band of carbon and is attributed to the extent of graphitization in the system. To interpret the defect and disorderness, the I_D/I_G ratio is employed and for NGr, it is estimated to be 1.27, which is higher than that of GO (0.91) and is consistent with the higher defect density and few layered structure of NGr resulted from the high temperature annealing process.[34] The I_D/I_G ratio of ZnNi-LDH/NGr is found to be 1.37, which is even higher than that of NGr. This is expected to be caused by the higher defect density in the catalyst and serves as substantiating evidence on the incorporation of the LDH moieties in between the NGr sheets.
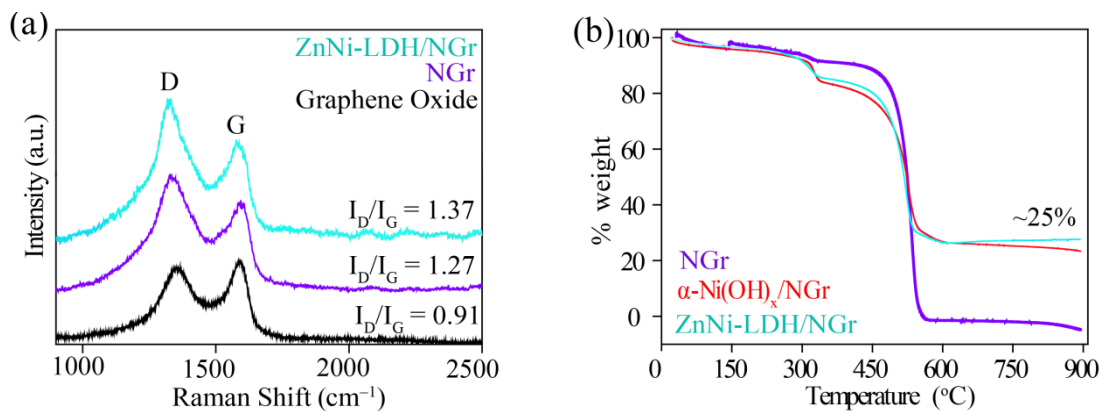
Figure 3: Comparative: (a) Raman spectra and (b) TGA profiles of ZnNi-LDH/NGr with the other control samples.

2.3.1.3. Thermo-gravimetric analysis

Basically, NiM-LDHs are composed of α-Ni(OH)$_2$ doped with other metal ions, where their hydrated layered structure is preserved.[31] One useful method to determine the degree of hydration is thermo-gravimetric analysis (TGA), which monitors the change of the sample's weight as a function of temperature. Water from these intrinsically hydrated α-Ni(OH)$_2$.xH$_2$O polymorphs can be removed only at higher temperatures (250–300 ^{o}C). Figure 3b reveals the thermal decomposition behaviour of α-Ni(OH)$_x$/NGr and ZnNi-LDH/NGr in oxygen atmosphere which particularly displays two endothermic weight loss

processes in both the cases (25–200 ^{o}C and 250–400 ^{o}C).[31] This data strongly supports the presence of α-Ni(OH)$_2$ phase in both the samples. Furthermore, the LDH to NGr ratio in the composite is supported by the TGA data, which clearly indicates an LDH loading of approximately ~25 weight % over NGr (Figure 3b).

2.3.1.4. Field-emission scanning electron microscopy analysis

After confirming the crystallographic phase of synthesized materials and role of Zn to stabilize a particular nickel hydroxide phase in ZnNi-LDH, morphological investigations have been first performed through FESEM technique. The specific aim of FESEM was to investigate the distribution of the LDH-sheets over the NGr framework, which revealed a more or less uniform distribution of numerous LDH-nanosheets over the NGr scaffold (Figure 4). These LDH nanosheets are seemed to be irregular with non-uniform dimensions ranging from 50 to 200 nm and are appeared to be well dispersed. Moreover,
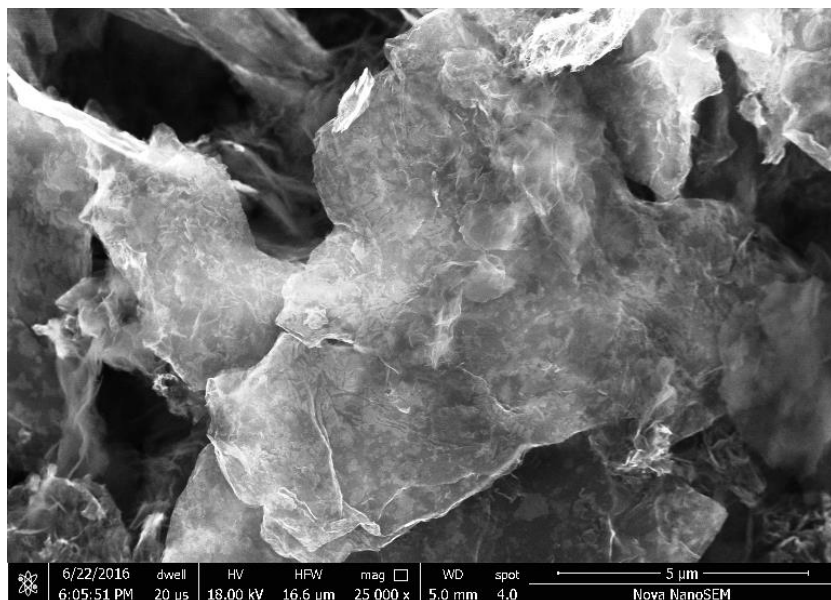

Figure 4: FESEM image of ZnNi-LDH/NGr.

hybridization of LDH with NGr is found to help in preventing the restacking and rumpling of the NGr sheets, which could be inferred from the presence of larger NGr sheets in Figure 4.

## 2.3.1.5. Transmission electron microscopy analysis

Subsequent to the bulk morphological investigations, nanostructural properties of the as-synthesized materials are investigated through the TEM analysis. Figure 5 represents the TEM images of ZnNi-LDH/NGr. Images presented in Figure 5a, and 5b demonstrate a very thin, flexible and transparent sheet-like 2D morphology of the as-synthesized catalyst with micron sized planar patches representing the fundamental features of the sheet-like layered structure. This morphology showed apparent disparity from the NGr sheets and confirming the existence of the layers of LDHs over NGr (Figure 5c). A close inspection of the nature of the growth pattern on ZnNi-LDH/NGr revealed the presence of a number of tiny metallic nanoparticles (NPs) ranging from 5–6 nm in size, which are embedded between the ZnNi-LDH nanosheets and the NGr scaffold (Figure 5d and 5e).[31,32] This has been further confirmed through Figure 5f which revealed that the TEM image recorded after prolonged electron beam exposure resulted into either removal of the thin hydroxide layer *via* dehydration with a concomitant enhanced visibility of the embedded tiny NPs or recrystallization of the thin layers into NPs due to the presence of the OCN^- moieties (intermediate product of the urea decomposition). Presence of the OCN^- moieties can favour the formation of Ni–N bond between Ni^{2+} and OCN^- that could eventually break and leave metallic moieties during the high energy electron beam exposure.[26] Figure 5g and 5h represent the selected area electron diffraction (SAED) pattern of ZnNi-LDH/NGr corresponding to the regions in Figure 5b and 5f, respectively. The SAED pattern in the former one is affirming semi-amorphous nature of the hydroxide material whereas the pattern in the latter one displays crystalline nature of the nano-crystallites.[1,9,35] Interestingly, the planes corresponding to NGr are fade in the SAED pattern of ZnNi-LDH/NGr in comparison to that of bare NGr, again confirming the coverage of NGr with the LDH-sheets (Figure 5g, 5h and inset in Figure 5c).

TEM also served as an efficient tool to differentiate between ZnNi-LDH/NGr and the other controlled samples. In the case of ZnNi-LDH/NGr, the whole morphology is appeared to be thin sheet-like structure compared to the crumbled sheets of 3D hierarchical architecture appeared in the case of α-Ni(OH)$_x$/NGr (Figure 6a). This morphological disparity served as a good evidence on the critical role played by Zn in
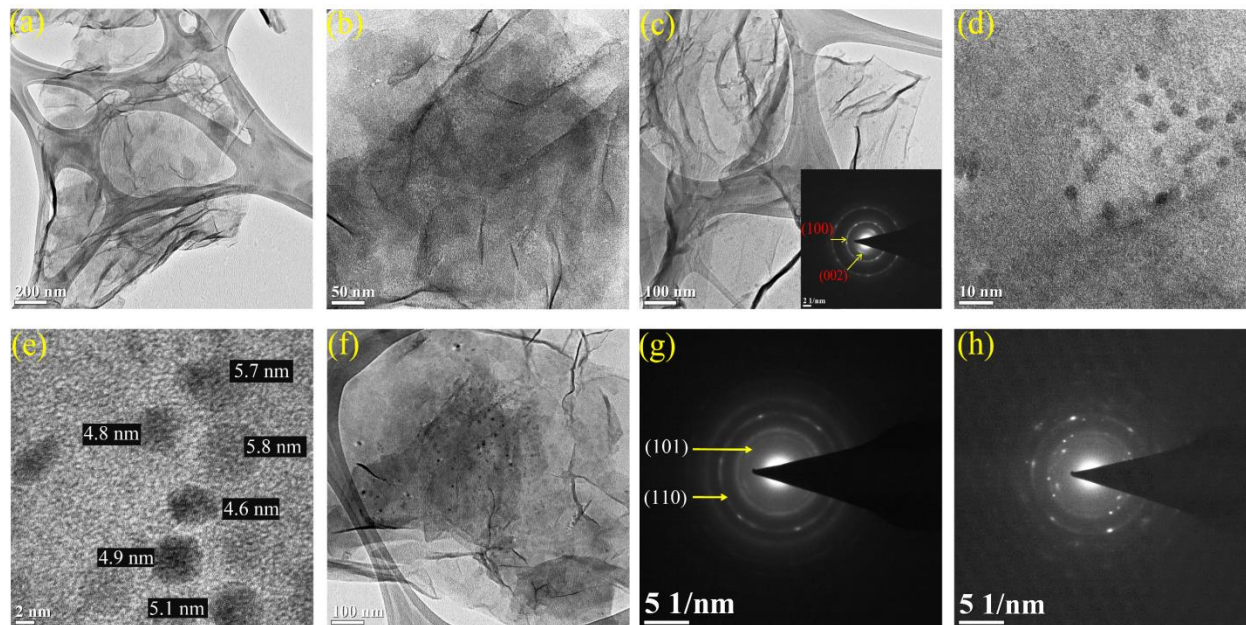
Figure 5: TEM images: (a) and (b) for ZnNi-LDH/NGr at different magnifications, (c) for NGr, (d) and (e) again for ZnNi-LDH/NGr at higher magnification, (f) TEM image for ZnNi-LDH/NGr recorded after prolonged electron beam exposure, (g) and (h) represent the SAED patterns recorded corresponding to the regions in Figure 3b and Figure 3f, respectively.

accomplishing the formation of the well dispersed thin layered sheets. Additionally, TEM is found to be a good characterization technique to find out the role of the LDH support toward the growth of thinner LDH sheets. The unsupported ZnNi-LDH is displaying thick flaky patches in Figure 6b unlike the thin sheet-like morphology of ZnNi-LDH/NGr. Another important conclusion which can be withdrawn from the TEM analysis is that nitrogen doping helps to decorate evenly distributed thin layers of the LDH on the substrate, unlike the reduced graphene oxide (rGO). This can be readily visualized by comparing the TEM images of ZnNi-LDH/NGr (presented in Figure 5) and the TEM image of NiZn(OH)$_x$/rGO in Figure 6c , where the latter one presented irregular and ill-defined morphology compared to a well-controlled and homogeneous distribution achieved in the former case.
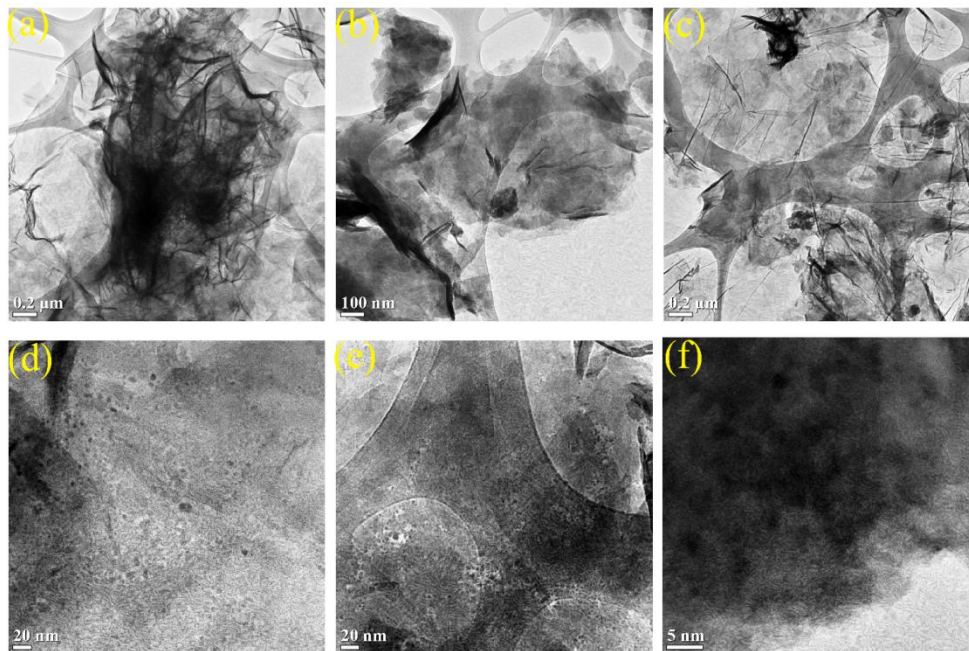
Figure 6: TEM images at lower magnification: (a) α-Ni(OH)$_x$/NGr, (b) ZnNi-LDH and (c) NiZn(OH)$_x$/rGO. Higher magnification TEM images: (d) α-Ni(OH)$_x$/NGr, (e) ZnNi-LDH and (f) NiZn(OH)$_x$/rGO.

Hence, N-doping induces the charge redistribution over the graphene sheet, making the NGr fertile enough for the anchoring of the LDH-nanosheets side by side directly onto the NGr substrate and inhibiting the Ostwald ripening tendency of the LDH-nanosheets. Similar to ZnNi-LDH/NGr, ill-defined nanocrystals are also present in unsupported α-Ni(OH)$_x$/N-rGO (Figure 6d), ZnNi-LDH (Figure 6e), and NiZn(OH)$_x$/rGO (Figure 6f), reflecting the intrinsic structural properties of the LDH compounds.[26,31,32] This novel hybridization of ZnNi-LDH with embedded NiZn NPs adhered on NGr is noteworthy which can help toward its electrochemical catalysis as can be seen in the later sections.

2.3.1.6. X-ray photoelectron spectroscopy analysis

Quantitative chemical state as well as surface composition of the catalyst was studied through X-ray photoelectron spectroscopy (XPS) analysis. Survey spectrum of ZnNi-LDH/NGr confirms the presence of both Ni and Zn with an atomic ratio of 3:1, similar to that of their initial salt concentrations (Figure 7). Atomic percentage of different elements present in the system was determined through the CASAXPS software, which revealed

very high atomic percentage of oxygen in ZnNi-LDH/NGr (25.30%). This higher percentage of oxygen in ZnNi-LDH/NGr is ascribed to the formation of the surface NiOOH moieties as well as layered hydroxides with plenty of intercalated oxygen containing species such as intercalated H_2O, CO_3^{2-}, NH_4^+, N=C=O, adsorbed O_2 *etc.* This aids to the overall wettability of the catalyst, which is a desirable factor for activity enhancement.[35,36]
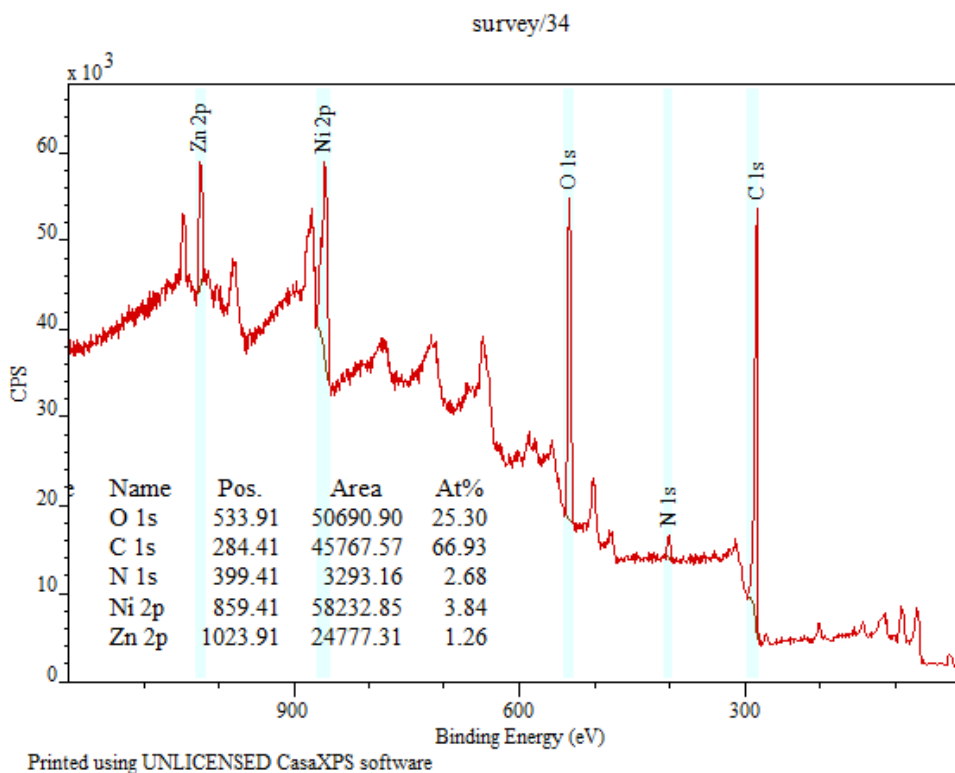
Figure 7: XPS survey spectrum of ZnNi-LDH/NGr showing the atomic percentages of various elements present in the system as determined through the CASAXPS software.

High resolution C 1s, O 1s and N 1s spectra of ZnNi-LDH/NGr was studied by individually deconvoluting the respective spectrum using the XPSPEAK41 software. The C 1s spectrum of ZnNi-LDH/NGr shows the deconvoluted peak positions for C=C (~284.6 eV), C–C (~285 eV), C=N (~286 eV) and C–N/C–O (~289 eV), affirming the N-doping in the graphene as well as the anchoring of ZnNi-LDH over NGr (Figure 8a).[29] In addition to this, ZnNi-LDH/NGr exhibits an extra peak positioned at ~290.7 eV corresponding to the presence of intercalated carbonate moieties in LDH.[37] As compared

to NGr (Figure 8b), the O 1s spectrum of ZnNi-LDH/NGr (Figure 8c) depicted entirely different peak feature and acquired a characteristic peak pattern to those of NiOOH-phase rich compounds. This fitted peak pattern displays a B.E. of 533.4 eV, indicating the presence of the NiOOH type of bonding interactions.[38] It is also comprised of sub-peaks in the B.E. range of (534–537 eV) related to the M–OH interactions, intercalated water and adsorbed O_2 molecules (Figure 8c).[38]
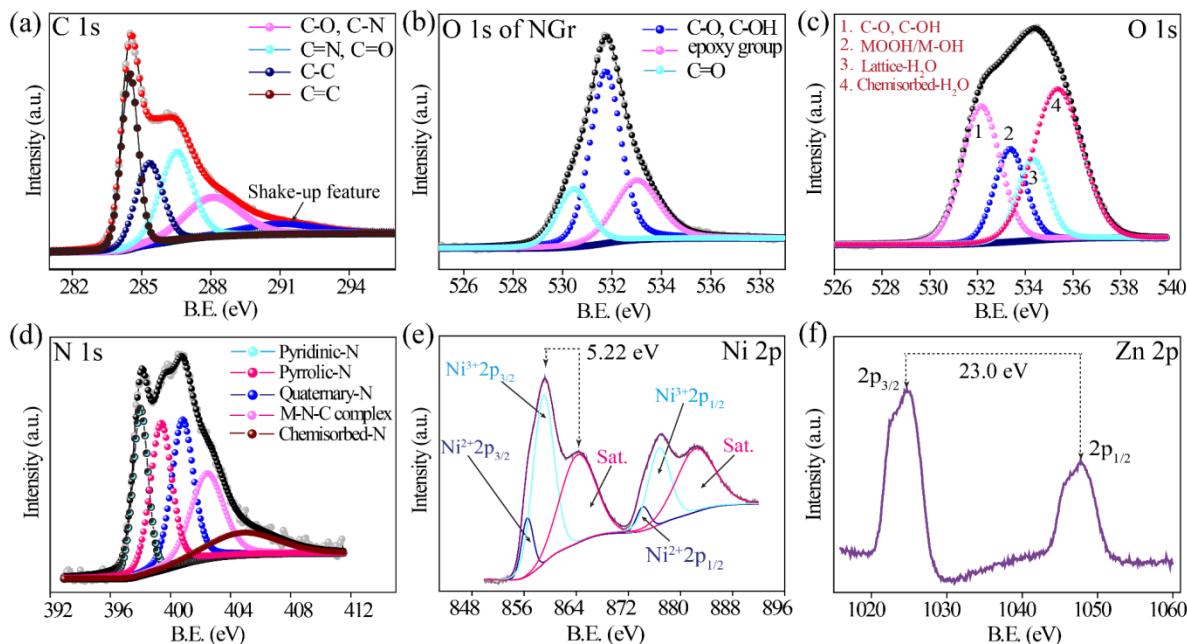
Figure 8: Deconvoluted XPS spectra: (a) C 1s of ZnNi-LDH/NGr, (b) O 1s of NGr; (c) O 1s, (d) N 1s, (e) Ni 2p, and (f) Zn 2p of ZnNi-LDH/NGr.

The N 1s spectrum of ZnNi-LDH/NGr shows a peak feature corresponding to N-doped graphene, consisting of the fitted sub-peaks for pyridinic (~398 eV), pyrrolic (~399.4 eV) and quaternary (~400.8 eV) N-species (Figure 8d).[29] In addition to this, the N 1s spectrum also affirms the presence of the M–N–C type of bonding interactions having a B.E. positioned at ~402.4 eV.[26] The N 1s spectrum also indicates the presence of chemisorbed nitrogen species such as NH_4^+ ions, OCN^- *etc.* in the B.E. range of 402.5–405.7 eV, further supporting the formation of LDH–NGr composite.[26] Thus, the spectral evidences corresponding to the C 1s, O 1s and N 1s signals of ZnNi-LDH/NGr have authenticated the formation of layered double hydroxide with intercalated ions and molecules, and strongly anchored over the NGr sheets *via* M–N–C types of bonding interactions.

Next, peak fitted Ni 2p spectrum of ZnNi-LDH/NGr was analyzed for the elucidation of nature of the Ni-phase as well as its interaction with Zn (Figure 8e). The deconvoluted Ni 2p XPS spectrum confirmed the presence of both Ni^{2+} as well as Ni^{3+} moieties in the system. The appearance of peaks at 859.1 and 876.8 eV suggested the presence of Ni^{3+} ions, majority of which attains the Υ-NiOOH phase.[38,39] Moreover, the presence of the satellite peak as well as higher binding energy shift of Ni 2p main line evidenced the presence of the octahedral stereochemistry, *i.e.,* the $[NiO_6]$ moieties with higher Ni oxidation state.[40,41] The main line to satellite peak difference is helpful to explain the XPS spectra, and for Ni $2p_{3/2}$ level it is 5.2 eV, which is consistent with the reports for the presence of NiOOH moieties.[42] Further, the peaks at 856.6 and 874.3 eV corresponds to the presence of small amount of Ni^{2+} ions from the $Ni(OH)_2$ moieties.[43] Most importantly, the fitted Ni 2p spectrum of ZnNi-LDH/NGr displayed close similarity with that of the Υ-NiOOH phase modelled by Grosvenor *et al.*[44] Figure 8f represents the XPS spectrum in Zn 2p core level region, representing two characteristic Zn $2p_{3/2}$ and Zn $2p_{1/2}$ peaks located at comparatively higher binding energy values of 1024.9 and 1047.8 eV, respectively. The reason for this higher binding energy shift is probably due to the bonding interactions operating between Zn and oxygen (an element with higher electro-negativity), evidencing the formation of Zn–OH type of bonding interactions.[33]

Hence, the XPS analysis observations corroborated the anchoring of ZnNi-LDH over NGr as well as the coverage of ZnNi-LDH/NGr catalyst surface with plenty of Υ-NiOOH phase moieties. This finding also revealed the role of Zn to stabilize Ni in its higher oxidation state and affirmed the presence of Zn in its hydroxide form.

2.3.2. Electrochemical water oxidation catalysis

Taking the advantage of the highly porous, open and semi-crystalline nature of ZnNi-LDH/NGr, we have tested our catalysts for water oxidation reaction (OER) in 1 M KOH, which was thoroughly degassed with N_2. For comparison, 20% RuO_2/C, NGr, α-$Ni(OH)_x$/NGr, ZnO/NGr, $NiZn(OH)_x$/rGO and unsupported ZnNi-LDH coated electrodes were also tested for OER. In general, in a heterogeneous catalyst perspective, it is known that a catalyst with high roughness factor (RF) will be having high amorphousness as well as high surface area but lower catalytic stability.[45,46] However, the case is found to be

different when we consider catalysts for electrochemical gas evolution reactions. In these types of reactions, high electrode surface roughness often results into slow mass transport of reactants (OH^-) into and products (O_2) out of the micro porosity generated in the amorphous catalysts.[45] This in turn affects the accessibility to deeply buried active centres and subsequently, to the overall catalytic performance. It has been experimentally proposed that the OER activity of NiZn-system is primarily limited by its higher roughness factor.[45]

Interestingly, in our system, we could successfully minimize this roughness factor issue by fabricating ZnNi-LDHs as a thin-layered texture over as well as in between the NGr sheets, which resulted into highly porous and open structure. Electrochemical active surface area (ECSA) as well as roughness factor of the catalyst was determined from the electrochemical double layer capacitance (C_{dl}) of the catalytically active surface.[45,46] C_{dl} was determined using scan rate dependent CV measurements in the non-faradaic capacitive region (range is typically of 0.1 V potential window, close to OCV of the system).[45] Figure 9a shows the CV profiles in the potential region of (0.92 to 1.02 V $vs.$ RHE) at different scan rates ranging from 10 mV s^{-1} to 150 mV s^{-1}. The formula for C_{dl} calculation is as follows:[45]

$$C_{dl}= i/\nu \tag{1}$$

where, i stands for the measured cathodic/anodic current and ν is the corresponding scan rate. The plot of i $vs.$ ν at 0.97 V $vs.$ RHE gives a straight line with a slope corresponding to C_{dl} (Figure 9b). The measured C_{dl} from this analysis using Equation 1 is 0.1716 mF. The ratio of C_{dl} to C_s (specific capacitance, which is 26 µF corresponding to the value used for most of the NiM-based systems in alkaline medium[46]) gives a direct measure of the ECSA value, which is 6.6 cm^2 in our case with a very low metal loading of 0.18 mg cm^{-2}. Moreover, the roughness factor (RF) has been evaluated by dividing ECSA with the electrode geometrical surface area (0.19625 cm^2) and is found to be $\approx$ 33.[45] This higher ECSA value and lower RF value suggest the presence of the high density of active sites which is provided by the tiny α-NiZn NPs as well as open turbostratic ZnNi-LDH structures present in the system. Hence, our work tries to minimize the limitations of ECSA and RF associated with the NiZn-system towards OER as mentioned by Jaramillo $et\ al.$[45] This controlled structural and functional modification accomplished in the present

case helps largely on the adsorption of the reactants (OH$^-$ ions) in the layered structure and their efficient oxidation which has been further supported by the modulated redox features as illustrated in the following sections through a set of electrochemical investigations.
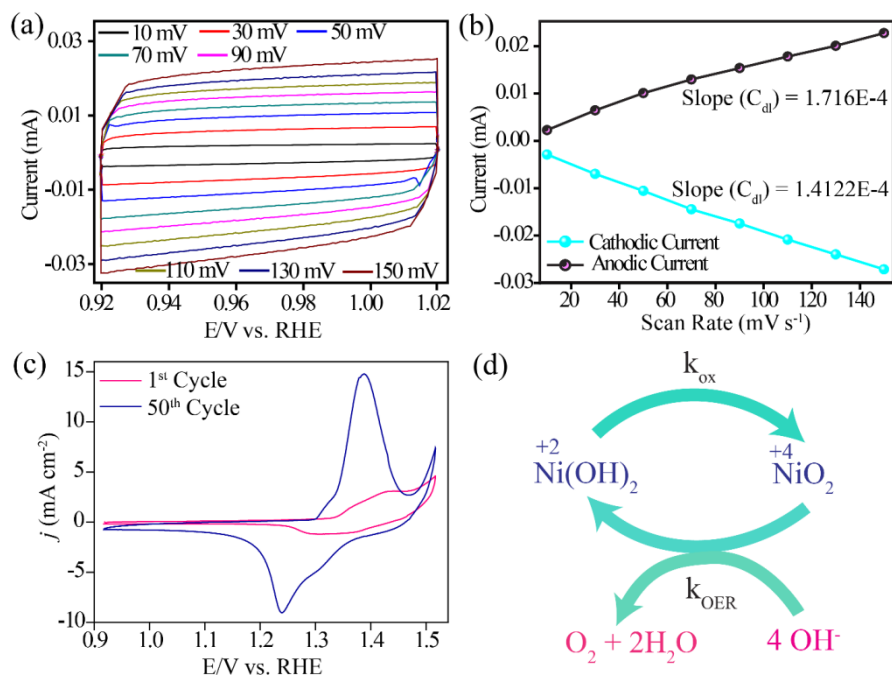

Figure 9: (a) Cyclic voltammograms recorded in the capacitive potential region at different voltage scan rates (mV s^{-1}), (b) plot of cathodic and anodic currents *vs.* potential sweep rate at 0.97 V *vs.* RHE, (c) comparative CV plot for 1st and 50th cycle recorded at a voltage scan rate of 30 mV s^{-1} indicating the electrochemical activation of the system under the potential induced conditions and (d) a general electrochemical water oxidation cycle over the Ni(OH)$_2$ based electrocatalysts with the nickel oxidation rate constant (k$_{ox}$) and OER rate constant (k$_{OER}$).[31]

Electrochemical activation of the catalysts was performed by subjecting the cyclic voltammetric potential cycling (50 cycles) at a scan rate of 30 mV s^{-1} in the potential window of 0.92 to 1.52 V *vs.* RHE in N$_2$ saturated 1 M KOH and Figure 9c depicting the 1st and 50th cycle. The quasi-reversible redox behavior of the cyclic voltammetric (CV) curves was ascribed to the oxidation of hydroxide moieties to the OER active Υ-NiOOH phase and its successive reduction back to the hydroxide-phase.[47,48] Moreover, this redox peak is followed by another oxidation peak corresponding to that of water oxidation

which is more prominent in the 50th cycle.[47,48] Figure 9c represents that with the increasing number of CV cycles, the redox peak amplitude increased and finally approached to a constant current value (50th cycle). This is caused by the activation of the catalyst to the OER active NiOOH-phase on the electrode surface, and it is confirmed by a negative shift both in the redox peak potential and the onset potential corresponding to the OER process.[47] A simplified reaction pathway for the electrochemical water oxidation on the Ni-based LDHs is presented as Figure 9d.

Next, for gaining a quantified information on the OER activity of the catalysts, linear sweep voltammograms (LSVs) were performed at a lower sweep rate of 10 mV s^{-1} in the potential window of 0.92 to 1.62 V (*vs.* RHE). Figure 10a represents the *iR*-corrected LSV profiles of ZnNi-LDH/NGr, α-Ni(OH)$_x$/NGr, NiZn(OH)$_x$/rGO, NGr and 20% RuO$_2$/C. Of note, the water oxidation activity is directly related to the OER current density and the primary figure of merit to evaluate the OER performance is the overpotential at 10 mA cm^{-2} (η_{10}) which is the metric relevant to the solar fuel synthesis.[45,47] The onset potential values (measured at 1 mA cm^{-2}) for ZnNi-LDH/NGr, α-Ni(OH)$_x$/NGr and 20% RuO$_2$/C are 1.48, 1.51 V and 1.447 V respectively, while η_{10} for these catalysts are 290 mV, 330 mV and 306 mV, respectively. Hence, even though the onset potential of 20% RuO$_2$/C is better than that of ZnNi-LDH/NGr, for attaining 10 mA cm^{-2}, our catalyst shows improved performance in 1 M KOH. This corresponds to a reduction in the overpotential by 16 mV, which is possibly caused by the open and highly accessible structure of the homemade catalyst. The more negative onset potential and lower overpotential for ZnNi-LDH/NGr as compared to α-Ni(OH)$_x$/NGr are basically attributable to the formation and even distribution of the thin ZnNi-LDH nanosheets over and in between the NGr sheets containing plenty of OER active sites (ϒ-NiOOH). The comparative OER performances of ZnNi-LDH/NGr (290 mV) and NiZn(OH)$_x$/rGO (360 mV) supports the essential role played by the N-doping in improving the OER performance. As it is visible from Figure 10a, NGr showed negligible performance toward OER.
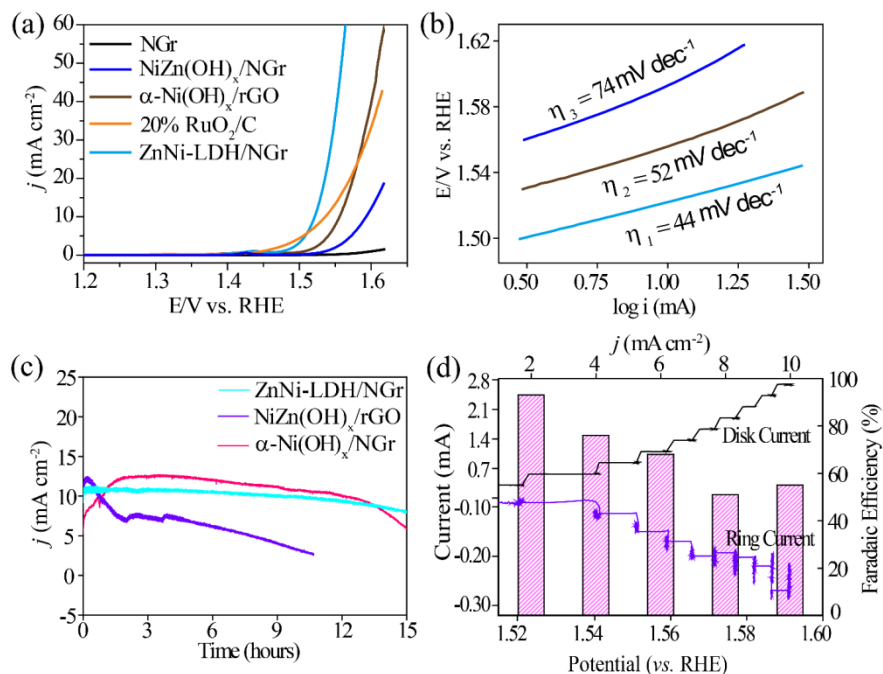
Figure 10: Comparative: (a) LSV polarization plots, (b) Tafel plots, where η_1, η_2 and η_3 represent the Tafel slope values of ZnNi-LDH/NGr, α-Ni(OH)$_x$/NGr and NiZn(OH)$_x$/rGO respectively**,** and (c) chronoamperometric stability data recorded for 15 h. (d) Faradaic efficiency determination of ZnNi-LDH/NGr with RRDE in N$_2$ saturated 1 M KOH at 1600 rpm.

To gain insights into the intrinsic catalytic activity of the catalysts, a more effective technique, *i.e.,* Tafel analysis, has been performed by plotting potential (V) *vs.* log i.[45-49] The measured Tafel slope for ZnNi-LDH/NGr is a mere 44 mV/decade, which is the characteristic of ϒ-NiOOH type active centres indicating excellent intrinsic activity of the catalyst (Figure10b).[48] For α-Ni(OH)$_x$/NGr and NiZn(OH)$_x$/rGO, the Tafel slope values are 52 and 74 mV/decade, illustrating comparatively poor reaction kinetics on these two controlled samples. Further, to inspect the durability aspects of the catalyst, comparative chronoamperometry (CA) measurements were performed for 15 h in 1 M KOH. With a constant applied potential of 1.57 V *vs.* RHE to maintain a current density of 10 mA cm^{-2}, ZnNi-LDH/NGr exhibited substantial stability with ~80% retention in the current density even after continuous 15 h of the test (Figure 10c). The slow decay observed in the current density, however, is attributed to the inactive oxide layer formation as well as leaching out of the sample because of huge O$_2$ evolution resulting from the fast reaction

kinetics. For analysing the electrochemical stability of α-Ni(OH)$_x$/N-rGO and NiZn(OH)$_x$/rGO, the experimental conditions remained the same except the applied potential which is 1.6 V *vs.* RHE (Figure 10c). α-Ni(OH)$_x$/N-rGO displayed a maximum current density of 12 mA cm^{-2} which thereafter showed a continuous current decay, and led to only 60% current retention after 15 h of the test. NiZn(OH)$_x$/rGO also exhibits similar kind of CA behaviour with a continuous current decay and an 11 h of the run resulted into a loss in the current density of about 75%. Thus, with better catalytic stability of ZnNi-LDH/NGr, the CA results evidence the role of both Zn and NGr to improve the electrochemical stability of the catalyst in alkaline media.

Finally, Faradaic efficiency (ε) for O$_2$ production by ZnNi-LDH/NGr was performed using RRDE technique in N$_2$-saturated 1 M KOH at 1600 rpm. During the RRDE measurement, the disk electrode was subjected to a number of one minute current steps varying from 2 to 10 mA cm^{-2} and the resulted potential was measured while the ring electrode was kept at a constant potential of 0.32 V *vs.* RHE throughout the experiment.[45,46] The O$_2$ molecules evolved through water oxidation at the disk electrode will be reduced by 2e$^-$ on the surrounding ring electrode. The corresponding ring and disk current signatures were used to calculate the Faradaic efficiency using the equation presented in Equation 2.[46]

$$\text{Faradaic efficiency } (\varepsilon) = 2 * I_r/I_d * N_{empirical} \qquad (2)$$

where, I$_r$ = limiting current of ring electrode

   I$_d$ = limiting current of disk electrode

The disk and ring currents are plotted against the resulted voltage, which is depicted in Figure 10d. The maximum Faradaic efficiency monitored is ~95% at a current density of 2 mA cm^{-2}. This current density is large enough to ensure O$_2$ evolution, while at the same time; it is sufficiently small to minimize the local un-dissolved O$_2$ saturation which in turn diminishes any possible error involved in the efficiency calculation. At higher current density (10 mA cm^{-2}), the Faradaic efficiency is decreased to ~55% owing to the local un-dissolved O$_2$ saturation and also due to the leaching out of the coated catalyst from the electrode during the bubble evolution. In general, the ε value should be above 90% for an OER catalyst in 1 M KOH.[46] This criteria is best fulfilled by our catalyst with

its ~95% faradaic efficiency at 2 mA cm^{-2}, suggesting the ability of our catalyst to perform OER over other non OER reactions (Cl$_2$ evolution[50], carbon corrosion *etc.*).

2.4.   Conclusion

In brief, we demonstrated the synthesis and stabilization of thin layered Ni–LDH, enriched with the OER active Ni-phase, (ϒ-NiOOH) by the incorporation of a less expensive and redox inactive metal ion *i.e.,* Zn^{2+}. The presence of Zn^{2+} is found to be enhancing the catalytic activity of the system by facilitating the formation of higher oxidation Ni sites in it as Ca^{2+} does in [Mn$_3$CaO$_4$]$^{6+}$, a Photo System II analogous catalyst.[3] Moreover, higher ECSA and lower RF values resulted into remarkable current density improvement as well as activity enhancement towards OER. The oxophilic nature of Zn is also reflected as a contributing factor to accomplish the noteworthy stability displayed by the catalyst. In this way, the present work provided a simple method for the fabrication of a highly efficient and durable water oxidation electrocatalyst with a mere 290 mV overpotential at 10 mA cm^{-2} and a small Tafel slope of 44 mV decade^{-1}, which can be extended to real electrochemical water splitting devices. Furthermore, our studies suggested the promise of designing an effective way to stabilize the active phase (*i.e.*, ϒ-NiOOH) of the most OER proficient non-noble transition metal, *i.e.*, nickel.

2.5.   References

1   X. Yu, M. Zhang, W. Yuan and G. Shi, *J. Mater. Chem. A*, 2015, **3**, 6921-6928.
2   J. O. M. Bockris, *Science*, 1972, **176**, 1323-1323.
3   J. D. Blakemore, R. H. Crabtree and G. W. Brudvig, *Chem. Rev.*, 2015, **115**, 12974-13005.
4   Z.-Q. Liu, H. Cheng, N. Li, T. Y. Ma and Y.-Z. Su, *Adv. Mater.*, 2016, **28**, 3777-3784.
5   G. Fu, Y. Chen, Z. Cui, Y. Li, W. Zhou, S. Xin, Y. Tang and J. B. Goodenough, *Nano Lett.*, 2016, **16**, 6516-6522.
6   I. Katsounaros, S. Cherevko, A. R. Zeradjanin and K. J. J. Mayrhofer, *Angew. Chem. Int. Ed.*, 2014, **53**, 102-121.
7   Y. Lee, J. Suntivich, K. J. May, E. E. Perry and Y. Shao-Horn, *Phys. Chem. Lett.*, 2012, **3**, 399-404.
8   R. Subbaraman, D. Tripkovic, K.-C. Chang, D. Strmcnik, A. P. Paulikas, P. Hirunsit, M. Chan, J. Greeley, V. Stamenkovic and N. M. Markovic, *Nat Mater*, 2012, **11**, 550-557.
9   K. Fan, H. Chen, Y. Ji, H. Huang, P. M. Claesson, Q. Daniel, B. Philippe, H. Rensmo, F. Li, Y. Luo and L. Sun, *Nat. Commun.*, 2016, **7**, 11981.
10   O. Diaz-Morales, I. Ledezma-Yanez, M. T. M. Koper and F. Calle-Vallejo, *ACS Catal.*, 2015, **5**, 5380-5387.
11   J. Qi, W. Zhang, R. Xiang, K. Liu, H.-Y. Wang, M. Chen, Y. Han and R. Cao, *Adv. Sci.*, 2015, **2**, 1500199.
12   X. Li, X. Hao, A. Abudula and G. Guan, *J. Mater. Chem. A*, 2016, **4**, 11973-12000.
13   M. K. Debe, *Nature*, 2012, **486**, 43-51.
14   L. Han, S. Dong and E. Wang, *Adv. Mater.*, 2016, **28**, 9266-9291.
15   B. J. Trześniewski, O. Diaz-Morales, D. A. Vermaas, A. Longo, W. Bras, M. T. M. Koper and W. A. Smith, *J. Am. Chem. Soc.*, 2015, **137**, 15112-15121.
16   G. Fan, F. Li, D. G. Evans and X. Duan, *Chem. Soc. Rev.*, 2014, **43**, 7040-7066.
17   R. S. Jayashree and P. Vishnu Kamath, *J. Appl. Electrochem*, 2001, **31**, 1315-1320.
18   H. Chen, J. M. Wang, Y. L. Zhao, J. Q. Zhang and C. N. Cao, *J Solid State Electrochem*, 2005, **9**, 421-428.

19 D. Tang, Y. Han, W. Ji, S. Qiao, X. Zhou, R. Liu, X. Han, H. Huang, Y. Liu and Z. Kang, *Dalton Trans*, 2014, **43**, 15119-15125.
20 F. Rong, J. Zhao, P. Su, Y. Yao, M. Li, Q. Yang and C. Li, *J. Mater. Chem. A*, 2015, **3**, 4010-4017.
21 D. C. Marcano, D. V. Kosynkin, J. M. Berlin, A. Sinitskii, Z. Sun, A. Slesarev, L. B. Alemany, W. Lu and J. M. Tour, *ACS Nano*, 2010, **4**, 4806-4814.
22 I. Y. Ikhsani, S. J. Santosa and B. Rusdiarso, *Indones.   J. Chem., 2016, 16, 36-44.*
23 U. Costantino, F. Marmottini, M. Nocchetti and R. Vivani, *Eur. J. Inorg. Chem*, 1998, **1998**, 1439-1446.
24 Y. Han, Z.-H. Liu, Z. Yang, Z. Wang, X. Tang, T. Wang, L. Fan and K. Ooi, *Chem. Mater.*, 2008, **20**, 360-363.
25 B. Hu, S.-F. Chen, S.-J. Liu, Q.-S. Wu, W.-T. Yao and S.-H. Yu, *Chem. Eur. J*, 2008, **14**, 8928-8938.
26 X. Ge, C. D. Gu, X. L. Wang and J. P. Tu, *Chem. Commun.*, 2015, **51**, 1004-1007.
27 M. Görlin, P. Chernev, J. Ferreira de Araújo, T. Reier, S. Dresp, B. Paul, R. Krähnert, H. Dau and P. Strasser, *J. Am. Chem. Soc.*, 2016, **138**, 5603-5614.
28 X. Wang, J. Hu, W. Liu, G. Wang, J. An and J. Lian, *J. Mater. Chem. A*, 2015, **3**, 23333-23344.
29 Y. Zhao, R. Nakamura, K. Kamiya, S. Nakanishi and K. Hashimoto, *Nat. Commun.*, 2013, **4**, 2390.
30 D. Tang, J. Liu, X. Wu, R. Liu, X. Han, Y. Han, H. Huang, Y. Liu and Z. Kang, *ACS Appl. Mater. Interfaces*, 2014, **6**, 7918-7925.
31 D. S. Hall, D. J. Lockwood, C. Bock and B. R. MacDougall, *P ROY SOC A-MATH PHY*, 2015, **471**.
32 Y. Zhu, C. Cao, S. Tao, W. Chu, Z. Wu and Y. Li, *Sci. Rep.*, 2014, **4**, 5787.
33 M. R. Arefi, S. Rezaei-Zarchi, *Int. J. Mol. Sci.* 2012, **13**, 4340-4350.
34 H. Wang, T. Maiyalagan and X. Wang, *ACS Catal.*, 2012, **2**, 781-794.
35 L. Poul, N. Jouini and F. Fiévet, *Chem. Mater.*, 2000, **12**, 3123-3132.
36 X. Zhu, C. Tang, H.-F. Wang, Q. Zhang, C. Yang and F. Wei, *J. Mater. Chem. A*, 2015, **3**, 24540-24546.
37 D. Puentes-Camacho, E. F. Velázquez, D. E. Rodríguez-Félix, M. Castillo-Ortega, R. R. Sotelo-Mundo, T. del Castillo-Castro, *Adv. Nat. Sci. Nanosci. Nanotechnol.* 2017, **8**, 045011.
38 X. Li, G.-Q. Han, Y.-R. Liu, B. Dong, W.-H. Hu, X. Shang, Y.-M. Chai and C.-G. Liu, *ACS Appl. Mater. Interfaces*, 2016, **8**, 20057-20066.
39 Z. Wang, J. Li, X. Tian, X. Wang, Y. Yu, K. A. Owusu, L. He and L. Mai, *ACS Appl. Mater. Interfaces*, 2016, **8**, 19386-19392.
40 M. C. Biesinger, B. P. Payne, L. W. M. Lau, A. Gerson and R. S. C. Smart, *Surf. Interface Anal*, 2009, **41**, 324-332.
41 J. Matienzo, L. I. Yin, S. O. Grim and W. E. Swartz, *Inorganic Chemistry*, 1973, **12**, 2762-2769.
42 H. W. Nesbitt, D. Legrand and G. M. Bancroft, *Phys Chem Miner,* 2000, **27**, 357-366.
43 S. Nayak, L. Mohapatra and K. Parida, *J. Mater. Chem. A*, 2015, **3**, 18622-18635.
44 A. P. Grosvenor, M. C. Biesinger, R. St. C. Smart, N. S. McIntyre, *Surf. Sci.*, 2006, **600**, 1771–1779.
45 C. C. L. McCrory, S. Jung, I. M. Ferrer, S. M. Chatman, J. C. Peters and T. F. Jaramillo, *J. Am. Chem. Soc.*, 2015, **137**, 4347-4357.
46 C. C. L. McCrory, S. Jung, J. C. Peters and T. F. Jaramillo, *J. Am. Chem. Soc.*, 2013, **135**, 16977-16987.
47 M. Gong and H. Dai, *Nano Res.*, 2015, **8**, 23-39.
48 M. Gao, W. Sheng, Z. Zhuang, Q. Fang, S. Gu, J. Jiang and Y. Yan, *J. Am. Chem. Soc.*, 2014, **136**, 7077-7084.
49 J.-M. Hu, J.-Q. Zhang and C.-N. Cao, *Int. J. Hydrogen Energy*, 2004, **29**, 791-797.
50 V. Petrykin, K. Macounova, J. Franc, O. Shlyakhtin, M. Klementova, S. Mukerjee and P. Krtil, *Chem. Mater.*, 2011, **23**, 200-207.

Chapter 3

NiZn Double Hydroxide-Derived Nickel Selenide/Nitrogen-Doped Graphene Composite to Catalyze the Overall Water Electrolysis*

The present chapter illustrates the work targeted for reducing the electrolyzer installation cost both by utilizing low-cost active metals as well as by eliminating the cost of designing two different materials. The work introduces a self-templating method for the designing of porous, edge-site-rich hybrid nanomaterials *via* the selective etching of layered double hydroxide precursors that contain an amphoteric metal by alkali treatment followed by vapour phase selenization. The obtained hexagonal nickel selenide nanoplates anchored over nitrogen-doped graphene showed highly efficient and robust water oxidation reaction (WOR) electrocatalysis. It demonstrated a low overpotential of ~311 mV to achieve the benchmark 10 mA cm^{-2} WOR current density in 1 M KOH. When we fabricated an alkaline water electrolyzer, it enabled high-performing overall water splitting with a low overpotential of 460 mV from theoretical voltage of 1.23 V to generate sufficient amounts of H$_2$ and O$_2$ by achieving a current density of 10 mA cm^{-2}. The catalyst has also displayed outstanding electrochemical stability toward all the employed reactions.
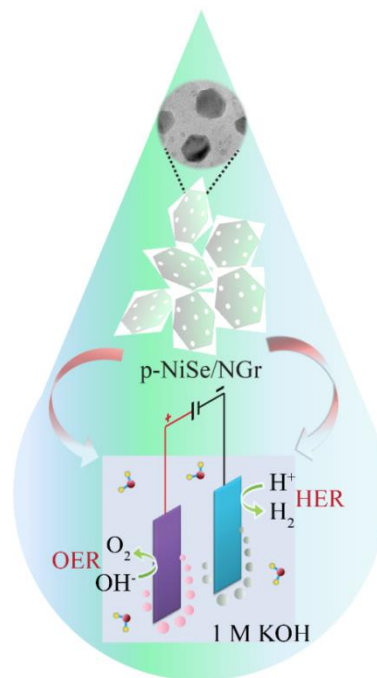
3.1. Introduction

Recently, fuel cells, especially hydrogen fuel cells, have come into the picture as one of the promising choices that can provide green and sustainable energy using hydrogen as the fuel.[1] However, the sustainability as well as eco-friendliness of the fuel cell depends directly on the source of hydrogen.[2,3] To date, fossil fuels are the major source of hydrogen, making the fuel cell technology dependent on the non-renewable fossil fuels and practically defeating its useful purpose.[4,5] One of the promising ways of resolving this issue is to produce hydrogen using an environmentally inoffensive route, where water can be the best solution.[6] Hence, water splitting bestows a promising technology, availing us with on-site/on-demand H_2 producing capability along with its feasibility of coupling with renewable energy sources to mitigate their intermittency and the localized nature.[7] Additionally, in contrast to photochemical water splitting, which solely depends on solar energy, electrochemical water splitting widens the scope for using various kinds of renewable energy sources.[7] In this way, electrochemical water splitting technology opens up the opportunity to generate hydrogen fuel in a greener way to make the fuel cell technology fully sustainable and eco-friendly.[6]

Electrochemical water splitting involves two half-cell reactions: the hydrogen evolution reaction (HER) and the oxygen evolution reaction (OER).[7] However, the unfavorable kinetics of these two electrode reactions are considered as the bottleneck for efficient electrolysis, leading to high overpotential to facilitate the work.[7] Pt and Ru/Ir based catalysts have long been considered as state-of-the-art electrocatalysts; however, their high cost and scarce availability have geared research toward the development of inexpensive and earth-abundant material-based catalysts.[8] Development of cost-effective electrocatalysts for HER in acidic medium and for OER in alkaline medium has already achieved significant success.[9-13] Instead of using different catalytic materials for catalyzing the two half-cell reactions, if both the electrodes employ the same material, the overall material cost can be reduced by avoiding the complicated process of designing the two different catalysts.[6,14] However, the designing of a high-performance bifunctional catalyst that works in a medium having uniform pH is quite challenging. Although some progress has been made in this direction,[14-17] there is still much to be done in the designing and optimization of bifunctional catalysts that can make the electrolyzer more appealing both in terms of cost and energy consumption.

Nickel hydroxides[18] and oxides[19,20,21] are among the best electrolyzer catalysts; however, replacing the oxides with selenides introduces a number of favorable factors which can further enhance the performance of the Ni-based systems.[12,21,22] Great progress has been achieved in the past few years in developing earth-abundant metal chalcogenide-based materials for various electrochemical applications.[14,16,22] For example, Kwak *et al.*[23] demonstrated excellent HER performance of $CoSe_2$ nanocrystals and good OER performance of $NiSe_2$ nanocrystals in alkaline medium. In another report, Liang *et al.*[15] demonstrated the improved HER performance of converted $NiSe_2$ nanosheets from the selenization of β-$Ni(OH)_2$. In a recent study, Haoyi *et al.*[21] demonstrated the enhancement of the catalytic stability of ultrathin nickel diselenide nanowires by decorating them with amorphous nickel oxide nanoparticles for overall water electrolysis.

Hence, by screening the existing transition metal selenide-based HER and OER catalysts, one can conclude that nickel selenide can be a promising candidate as a bifunctional catalyst for alkaline water electrolysis.

To further improve its performance, it is of great importance to engineering its surface configuration by considering two critical requirements; first, enrichment of the active catalytic sites and second, the stability of the active sites during an electrochemical analysis. In this context, we report a 3-step approach to design porous and edge-site-rich hybrid material *via* the selective etching of ZnNi-LDH/NGr precursors that contain an amphoteric metal (zinc) by alkali treatment followed by vapor-phase selenization. Additionally, the use of NGr-supported precursor helped to reduce the aggregation of selenides over NGr resulting in an open and active sites exposed catalyst system. The obtained hexagonal nickel selenide/NGr is found to contain monoclinic selenide phase along with a trace amount of nickel oxide and elemental selenium. Thus, the unique electronic structure of crystalline nickel selenide benefitted with the randomly oriented bonds of the amorphous NiO_x as well as elemental selenium helped for the acceleration of both the HER and OER kinetics along with remarkable electrochemical stability in the strong alkaline medium. In this way, enriching the catalyst surface with abundant active sites, as well as its hybridization with electronically conducting NGr, resulted in favorable electrochemical performance toward the overall alkaline water electrolysis with a low overpotential of 460 mV at 10 mA cm^{-2} for overall alkaline water electrolysis.

3.2. Experimental section

3.2.1. Synthesis of graphene oxide (GO) and nitrogen-doped graphene (NGr): Graphene oxide (GO) was synthesized by adopting improved Hummer's method[24] from natural graphite by subjecting it with harsh oxidizing treatment. For the synthesis of nitrogen-doped graphene (NGr), 1 g of GO was first dissolved in adequate volume of de-ionized (DI) water by water-bath sonication and overnight stirring. Subsequently, melamine was added in the ratio of 1:5 (GO:melamine) into the GO-DI water solution and the mixture was continued for 12 h stirring; afterwards the mixture was heated at 80 ^{o}C with stirring until it was dried completely. The dried GO-melamine powder was subjected for heating at 900 ^{o}C for 3 h under argon atmosphere. Thereafter, the furnace was allowed to cool down naturally in the same atmosphere and the obtained NGr was collected.

3.2.2. Synthesis of ZnNi-LDH/NGr: For the synthesis of ZnNi-LDH/NGr, $NiCl_2 \cdot 6H_2O$ and $Zn(OAc)_2 \cdot 2H_2O$ (with a molar ratio of Ni/Zn = 3:1) were first dissolved in methanol and DI-water (3:2) mixture; subsequently, urea was added in a molar ratio of 1:5 of the metal ions to urea. Afterwards, the as-synthesized NGr was added to the above solution in the ratio of 1:4 of the metal ions to NGr. After dispersing *via* bath sonication, the mixture was poured into a 200 mL Teflon lined stainless steel autoclave and heated at 170 ^{o}C for 12 h. Finally, the synthesized sample was washed 3-4 times by centrifugation at 10,000 rpm for 10 min using methanol-water mixture and finally the sample was dried at 150 ^{o}C for 12 h. The sample is abbreviated as ZnNi/NGr in all the upcoming sections.

3.2.3. Conversion of ZnNi/NGr to porous β-Ni(OH)₂/NGr: The ZnNi/NGr sample was first dispersed in 1 M KOH through water bath sonication as well as stirring. Thereupon, the well dispersed sample was poured into a Teflon-lined stainless steel autoclave and heated at 160 ^{o}C for 20 h. After the reaction, the sample was washed with water thoroughly.

3.2.4. Conversion of porous β-Ni(OH)₂/NGr to porous NiSe/NGr: For the selenization of the porous β-Ni(OH)₂/NGr, we have reductively annealed the β-Ni(OH)₂/NGr in presence of selenium vapours under 10% H_2/argon atmosphere. For this purpose, we took the sample as well as Se powder (in 1:2 ratio of Ni to Se) and grinded it in a mortar-pestle, then kept the sample boat at the middle of the furnace. The furnace was heated at 600 ^{o}C for 3h at the heating rate of 2 ^{o}C per min with a continuous flow of H_2/argon. Thenceforth, the furnace was allowed to cool down to room temperature naturally, and

sample was collected. The selenized sample is designated as p-NiSe/NGr throughout the manuscript.

3.2.5. Synthesis of α-Ni(OH)$_x$/NGr: α-Ni(OH)$_x$/NGr was prepared by using the same procedure adopted for synthesizing ZnNiNGr without adding the Zn salt and by keeping the urea to metal ions ratio and NGr to metal ions ratio same as it was maintained for synthesizing ZnNiNGr.

3.2.6. Conversion of α-Ni(OH)$_x$/NGr to β-Ni(OH)$_2$/NGr and its selenization: The α-Ni(OH)$_x$/NGr was also treated with 1 M KOH in the same way as it was done for the synthesis of porous β-Ni(OH)$_2$/NGr. The KOH treated sample was further selenized in the same manner as it is done for synthesizing p-NiSe/NGr and the obtained sample is designated as β-Ni(OH)$_2$Se/NGr.

3.2.7. Direct conversion of ZnNi-LDH/NGr to ZnNiSe/NGr: The synthesis procedure is same as followed to synthesize p-NiSe/NGr; the only difference is that the ZnNi/NGr was used directly without any KOH treatment. And the product obtained was designated as ZnNiSe/NGr.

3.3. Results and Discussion

3.3.1. Structure and Morphology of the Catalyst

The synthesis route for the preparation of p-NiSe/NGr is represented in Scheme 1. ZnNi-LDH/NGr (abbreviated as ZnNi/NGr) was first synthesized by following the previous report wherein we demonstrated the controlled synthesis of thin layered ZnNi-LDH sheets anchored over NGr.[25] Here, we took the advantage of the thin layers of the LDHs as well as the amphoteric nature of zinc to synthesize porous, hexagonal and thin β-Ni(OH)$_2$ nanoplates by selectively etching the Zn^{2+} ions from the (Zn)Ni-LDH moieties *via* the alkali treatment. The obtained β-Ni(OH)$_2$/NGr was subsequently converted into porous NiSe/NGr (designated as p-NiSe/NGr) *via* the reductive annealing in the presence of selenium powder under 10% H$_2$/Ar atmosphere.
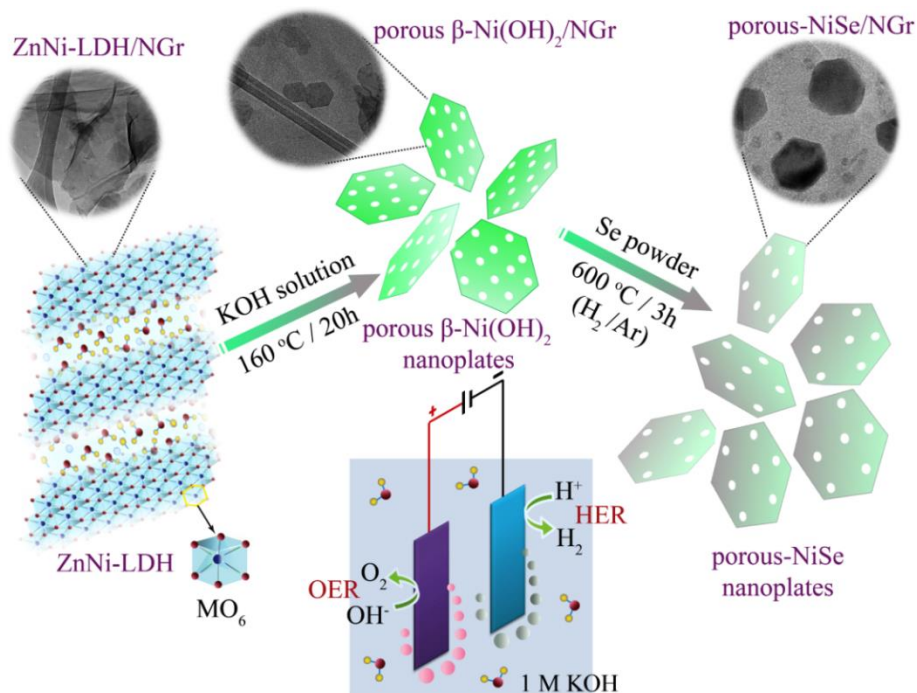
Scheme 1. Representation of the steps involved in the synthesis of porous-NiSe/NGr.

3.3.1.1. X-ray diffraction analysis

First, the crystallinity and phase purity of all the synthesized materials were investigated using X-ray diffraction (XRD) analysis. Figure 1a represents the XRD pattern of ZnNi/NGr, with broad diffraction peaks corresponding to the (003), (006), (101), (012), and (110) planes of α-Ni(OH)$_2$, indicating the formation of the layered double hydroxide (LDH) of nickel and zinc (ICDD Card No. 00-038-0715).[26,27] Basically, α-Ni(OH)$_2$.xH$_2$O is a polymorph consisting of the layers of β-Ni(OH)$_2$ with intercalated water molecules and charge balancing anions which, upon alkali treatment, loses the intercalated species and converts to β-Ni(OH)$_2$.[28] Interestingly, in the case of ZnNiNGr, along with the removal of the intercalated species, alkali treatment induces the selective etching of amphoteric Zn^{2+} ions as well, forming porous β-Ni(OH)$_2$/NGr. Figure 1b shows the diffraction peaks of the alkali-treated sample which can be assigned to the hexagonal β-Ni(OH)$_2$ phase with no remnant LDH peaks[15,18] (ICDD No. 01-073-1520). Of note, the XRD pattern in Figure 1a depicts broad (003) peak that confirms the anchoring of ZnNi-LDH over NGr as thin layers, which is retained in the β-Ni(OH)$_2$/NGr having broad XRD diffraction peaks, with minimum restacking of β-Ni(OH)$_2$ moieties over NGr during the KOH treatment. The vapor-phase selenization of β-Ni(OH)$_2$/NGr gives an XRD pattern that clearly identifies the

presence of pure monoclinic $Ni_{1-x}Se$ (ICDD No. 00-018-0890)[16] where the phase compositions vary from $Ni_{0.83}Se$ to $Ni_{0.75}Se$ depending upon the reaction conditions and the Ni to Se ratio owing to the small electronegativity difference between Ni and Se[29,30] (Figure 1c). The XRD analysis could not recognize the presence of NiO_x moieties and elemental Se indicating their trace amount and highly amorphousness of NiO_x.
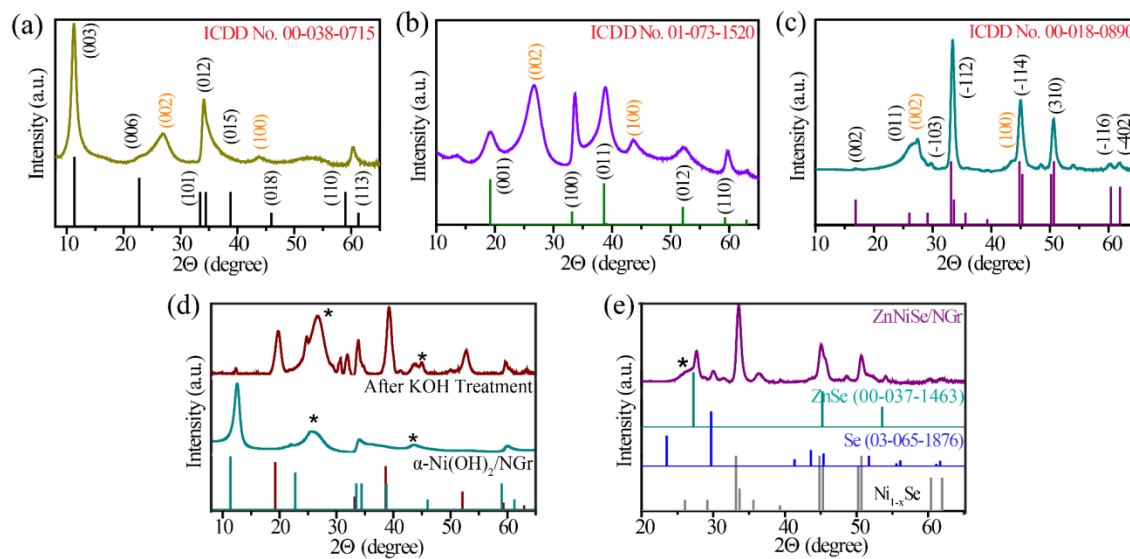

Figure 1. XRD patterns of: (a) ZnNi/NGr, (b) β-Ni(OH)₂/NGr and (c) p-NiSe/NGr. Comparative XRD patterns of: (d) α-Ni(OH)₂/NGr and its alkali treated sample representing incomplete α→β phase conversion and (e) ZnNiSe/NGr.

In contrast, the XRD pattern of alkali-treated α-Ni(OH)₂/NGr showed diffraction planes corresponding to both the Ni(OH)₂ phases, confirming the incomplete α→β phase conversion, presumably due to the absence of zinc which could aid the process (Figure 1d). In addition, the direct ZnNi/NGr selenization (designated as ZnNiSe/NGr in the upcoming sections) presented incomplete selenide formation showing clear diffraction planes corresponding to the metallic selenium and zinc selenide (Figure 1e). In this way, the selenization of alkali-treated ZnNiNGr over the selenization of direct ZnNi/NGr sample as well as the use of ZnNi/NGr over α-Ni(OH)₂/NGr helped us to synthesize the desired nickel selenide. Broad diffraction peaks, characteristic of carbon (002) and (100) planes, are apparently visible in all the XRD patterns indicating the presence of substantial amounts of NGr in the catalyst system.

3.3.1.2. Brunauer-Emmett-Teller (BET) analysis:

Surface porosity as well as specific surface area measurements of p-NiSeNGr and other controlled samples were performed through BET analysis by multilayer N_2 adsorption and desorption technique with the pore sizes being deduced from the desorption branches using the DFT method.
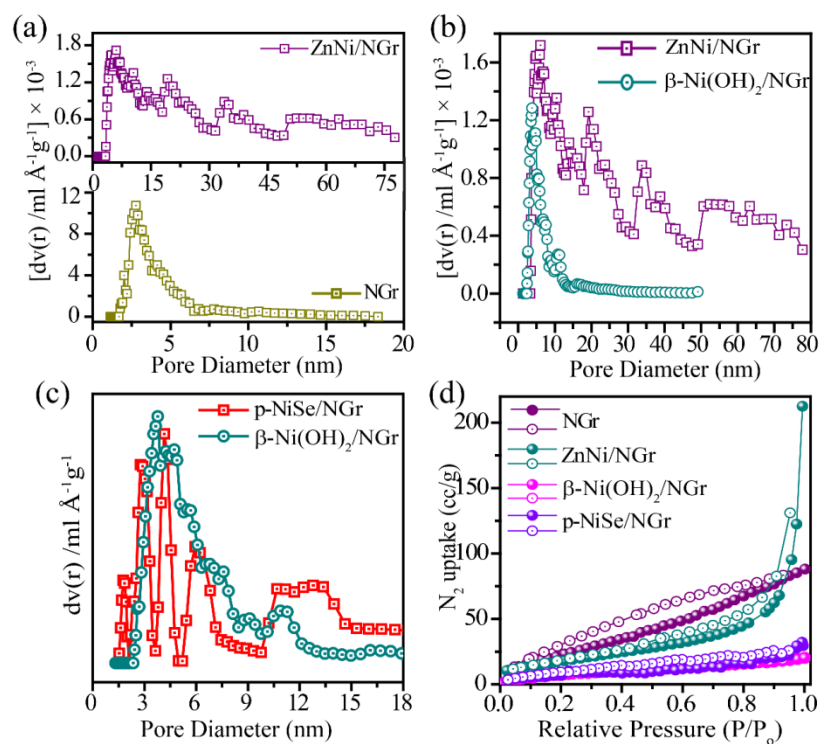

Figure 2: Comparative BET pore size distribution profiles for: (a) NGr and ZnNi/NGr, (b) ZnNi/NGr and β-Ni(OH)$_2$/NGr, (c) β-Ni(OH)$_2$/NGr and p-NiSe/NGr, and (d) comparative N_2 adsorption-desorption isotherms.

The relative pore size distribution of NGr with ZnNi/NGr showed the absence of pores in the size range of 2–5 nm in ZnNi/NGr, revealing the anchoring of LDH sheets over the microporous anchoring sites of NGr (Figure 2a). Moreover, the increase in the pore size of ZnNi/NGr in the size range of 5–35 nm confirms the anchoring of LDH sheets over as well as in between the NGr sheets (Figure 2a).[25] However, this porosity feature of ZnNi/NGr vanished after the alkali treatment which induces the reorganization, aggregation as well as overlapping of the small LDH sheets into hexagonal and porous β-Ni(OH)$_2$ nanoplates having porosity in the size range of 3–12 nm (Figure 2b), which is also retained in the p-NiSe/NGr (Figure 2c). The surface areas

measured for ZnNi/NGr, β-Ni(OH)$_2$/NGr, p-NiSe/NGr and NGr are ~68, ~31, ~35 and ~95 m^2 g^{-1} respectively, showing higher surface area for the sheet-like materials (NGr and ZnNi/NGr) which is apparent (Figure 2d).

3.3.1.3. Thermo-gravimetric analysis

Subsequent to the phase identification as well as porosity measurements, total loading of the selenide over NGr as well as the removal of zinc through KOH treatment was confirmed *via* the thermo-gravimetric analysis (TGA) in an oxygen atmosphere (Figure 3).
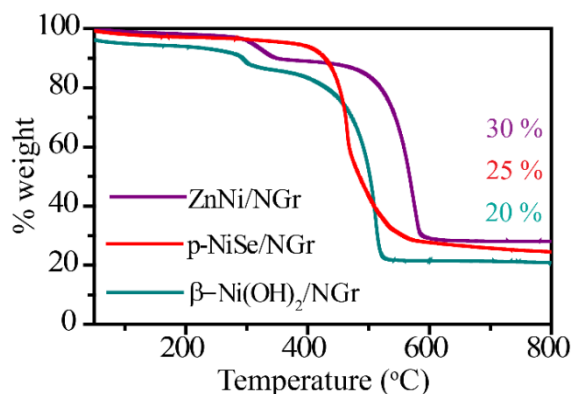

Figure 3. Comparative plots for the TGA profile.

The TGA graph of ZnNi/NGr shows an approximately 30% loading of ZnNi-LDH over NGr, bearing a characteristic endothermic weight loss region of LDH which is mainly within the 250–400 ^{o}C temperature range corresponding to the removal of adsorbed water and intercalated species.[28] The removal of zinc is confirmed by comparing the TGA graph of ZnNi/NGr and β-Ni(OH)$_2$/NGr, where the final metal loading is decreased to 20%. TGA graph of p-NiSe/NGr showed a 5% increment in the loading after selenization with a final metal selenide loading of 25% over the NGr.

3.3.1.4. Raman analysis

The defect density as well as extent of graphitization of all the NGr-based controlled samples was studied through the Raman spectral analysis. In the Raman spectrum, the two vibrational bands (the D band and G band) represent disorderness and extent of graphitization of the carbonaceous material, respectively.[31] The I_D/I_G ratio for NGr is smaller (1.24) than that of

ZnNi/NGr (1.275), revealing the formation of the hybrid material resulting in the increased disorderness (Figure 4a and 4b). This ratio is increased further when Raman analysis was continued for β-Ni(OH)$_2$/NGr (1.32) and p-NiSe/NGr (1.325), affirming the increment in the defect density with the KOH treatment as well as with the thermal selenization process (Figure 4a and 4b). The 495 cm^{-1} peak of ZnNi/NGr corresponds to the lattice mode of α-Ni(OH)$_2$[32] whereas the 542 cm^{-1} peak of β-Ni(OH)$_2$/NGr corresponds to the vibration of the Ni-O stretching mode of β-Ni(OH)$_2$[22], respectively (Figure 4b). After the selenization process, two new Raman bands appeared at 207 cm$^{-1,}$ and 241 cm^{-1} which can be ascribed to the stretching modes of Se-Se pairs (A$_g$ and T$_g$).[11] Another small peak visible at 511 cm^{-1} indicates the surface defects present on the NiSe (Figure 4a).[30]
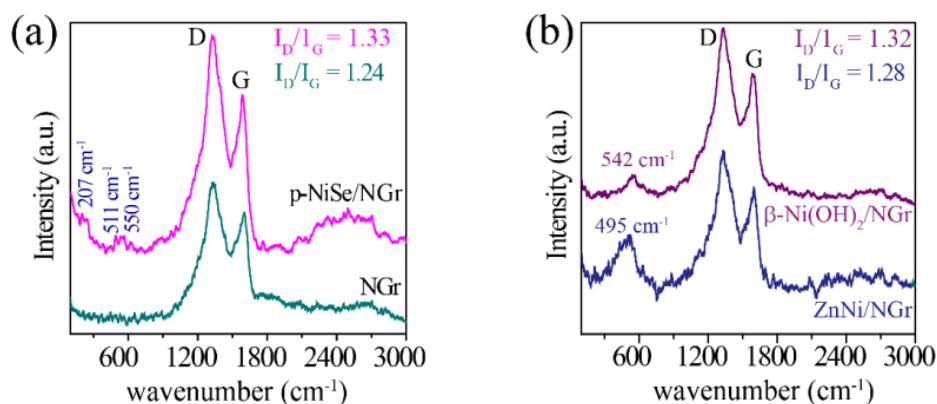

Figure 4. (a) and (b) represent comparative Raman spectra.

3.3.1.5. Field-emission scanning electron microscopy analysis

The bulk morphology of the as-synthesized samples was first examined using scanning electron microscopy (SEM). Figure 5A represents the SEM image of ZnNi/NGr revealing the uniform distribution of thin patches of LDHs over the NGr sheets with no noticeable LDH agglomeration. Inset of Figure 5A, *i.e.,* A(1), depicts the SEM image selected for the elemental mapping and the inset figures A(2), and A(3) show the elemental mapping for nickel and zinc, respectively, indicating the uniform distribution of Ni and Zn throughout the catalyst. The LDH-anchored NGr patches can be clearly distinguished from the NGr matrix by comparing the SEM image of ZnNi/NGr with that of NGr (Figure 5B). The SEM image of p-NiSe/NGr exhibited the presence of ill-defined hexagonal nanoplates embedded in the NGr matrix with favorable dispersion

characteristics (Figure 5C). Inset of the Figure 5C (C(2) and C(3)) represents the elemental mapping images for nickel and selenium revealing homogeneous and overlapping distributions of both the elements over NGr, suggesting selenide formation.
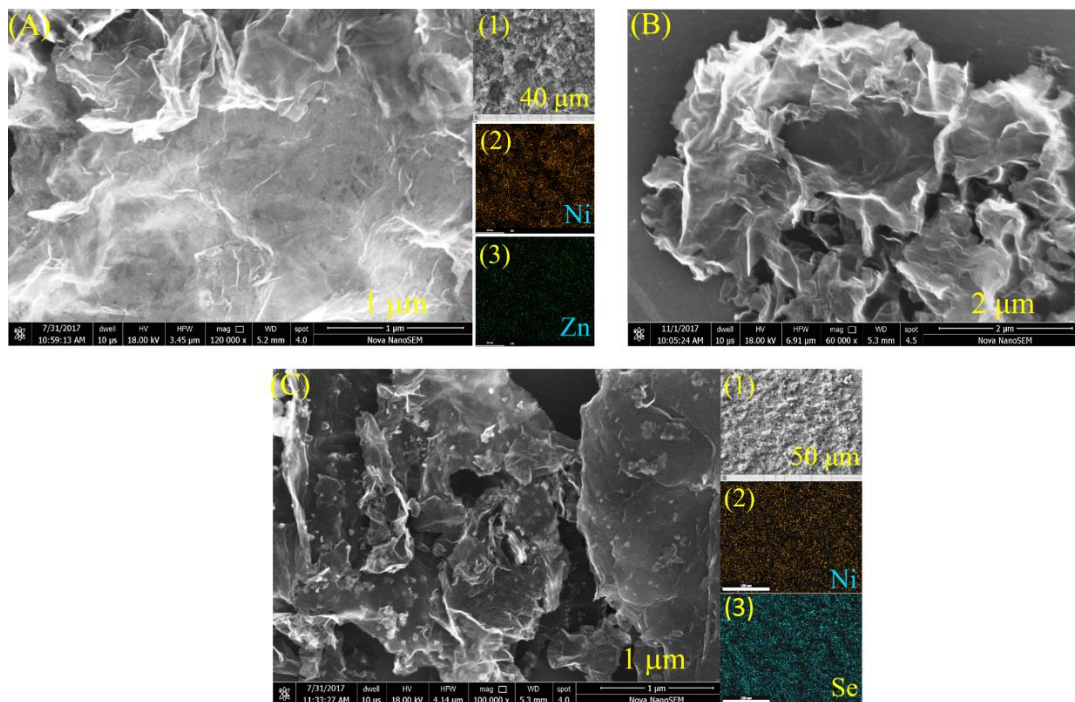

Figure 5. FESEM images of: (A) ZnNi/NGr where the inset image A(1) represents the SEM image selected for the elemental mapping and images A(2) and A(3) are the elemental distribution profiles for Ni and Zn respectively; (B) NGr; (C) p-NiSe/NGr where the inset image C(1) represents the SEM image selected for the elemental mapping and images C(2) and C(3) are the elemental distribution profiles for Ni and Se, respectively.

3.3.1.6. Transmission electron microscopy analysis

To get deep insight into the nanostructure of the as-synthesized materials, detailed characterization was performed using transmission electron microscopy (TEM) (Figure 6). Figure 6a shows the TEM image of ZnNi/NGr having thin, sheet-like structure with negligible agglomeration over NGr and the amorphous quality of the LDH is visible from the corresponding selected area electron diffraction (SAED) pattern having diffused diffraction rings (inset of Figure 6a). After the KOH treatment, thin LDH sheets took on the characteristic hexagonal structure of β-Ni(OH)$_2$ having a porous structure resulting from the Zn etching and

removal of the intercalated anions (β-Ni(OH)$_2$/NGr) (Figure 6b and 6c).[15,18] These porous β-Ni(OH)$_2$ structures have a size range of 50–60 nm and are found to be anchored as well as wrapped in between the NGr sheets. The inset of Figure 6b is the corresponding SAED pattern, showing the polycrystallinity of the material. Thus, a unique, active metal-based porous nanoplatelets have been prepared using a less expensive metal like Zn.
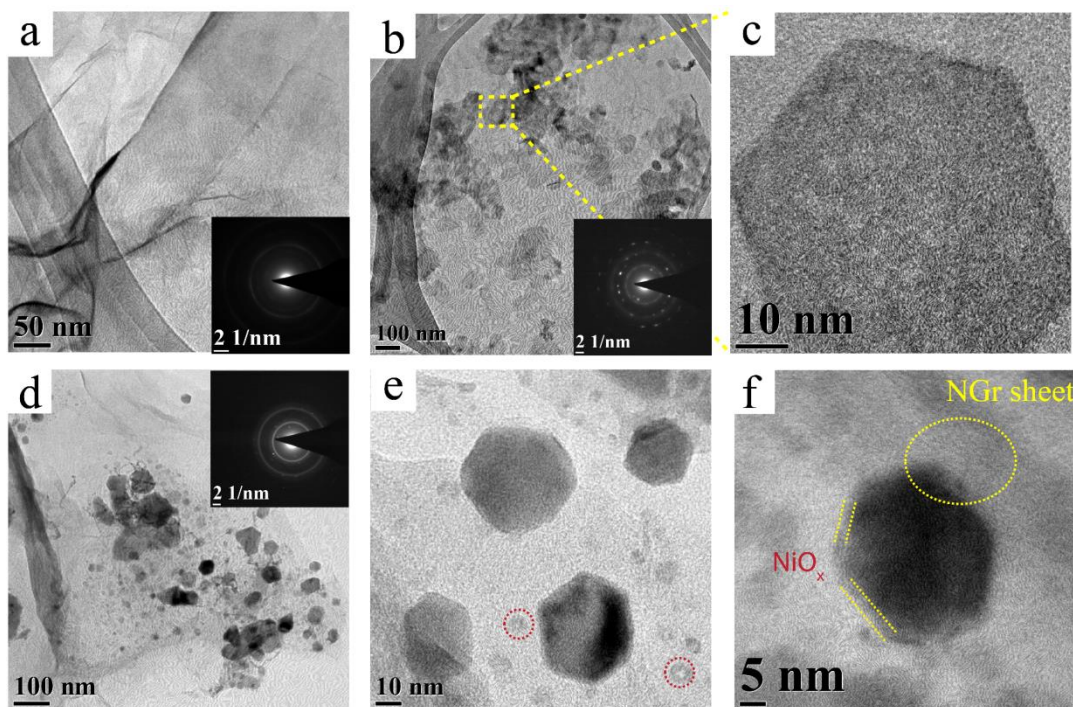
Figure 6. TEM images of: (a) ZnNi/NGr showing thin sheet-like structure over NGr, (b) and (c) for β-Ni(OH)$_2$/NGr at lower and higher magnifications, respectively, showing the hexagonal porous nanostructures embedded in the NGr matrix, (d), (e) and (f) show the TEM images of p-NiSe/NGr at different magnifications and in panel (f) the yellow dotted lines represent the thin NiO$_x$ layers over the hexagonal nickel selenide structure. Insets in the TEM images of all the three samples show their corresponding SAED pattern.

Furthermore, owing to the 20–25% selenide loading in p-NiSe/NGr, its distribution over NGr is not found to be very homogeneous; however, the hexagonal plates were found to be discrete, affirming the open and accessible structure of the thin and hexagonal NiSe nanoplates (Figure 6d and 6e). Some of these NiSe nanoplates are found to be trapped in between the NGr sheets as visible in Figure 6f with a yellow dotted circle. Any clear indication of the NiO$_x$ or elemental

selenium could not be found; however, the ill-defined hollow nanostructures (marked with maroon dotted circles), embedded into the NGr matrix, possibly could be their indications (Figure 6e). The appearance of low-contrast outline around the hexagonal structures (Figure 6f) are found to be an indication of the NiO_x moieties.[21] In this way, the advantage of having thin nanosheets of LDH precursors is reflected in its alkali treated as well as selenized samples with thin, plate-like hexagonal structures that retain their edge sites exposed. Hence, the three-step process outlined above generates open and porous nanostructures rich in edge sites which may act as active sites for electrocatalysis.

3.3.1.7. X-ray photoelectron spectroscopy analysis

We further used X-ray photoelectron spectroscopy to gain an in-depth understanding of the valance and chemical states of the different elements present in the p-NiSe/NGr. The XPS spectra of Ni 2p and Se 3d region are given in Figure 7. The Ni 2p spectrum shows a complex spectral feature with spin-orbit doublets, *i.e.,* Ni $2p_{3/2}$ and Ni $2p_{1/2}$, along with their corresponding satellites (Figure 7a). The deconvoluted Ni 2p spectrum reveals the presence of three different chemical environments for nickel. The deconvoluted doublet peaks located at 854.1 eV and 872.1 eV, along with their satellite peaks at 860.9 eV and 877.9 eV, correspond to Ni $2p_{3/2}$ and Ni $2p_{1/2}$ spin-orbit levels of the nickel oxide[21,33,34], perhaps originating from the heat treatment of nickel hydroxide that was inaccessible to selenization. Other deconvoluted doublet peaks located at 855.9 eV (Ni $2p_{3/2}$) and 874.1 eV (Ni $2p_{1/2}$), having their satellite peaks at 864.1 eV and 880.6 eV, respectively, indicate the presence of Ni^{2+} from the nickel selenide.[16,22,33] Apart from these sub peaks, an additional peak feature at 857.5 eV appear as a small shoulder, presumably due to the surface oxidation of the nickel selenide system.[21]

The deconvoluted XPS spectrum of Se 3d also revealed the presence of three chemical environments for selenium (Figure 7b). The Se 3d deconvoluted doublet peaks positioned at 53.9
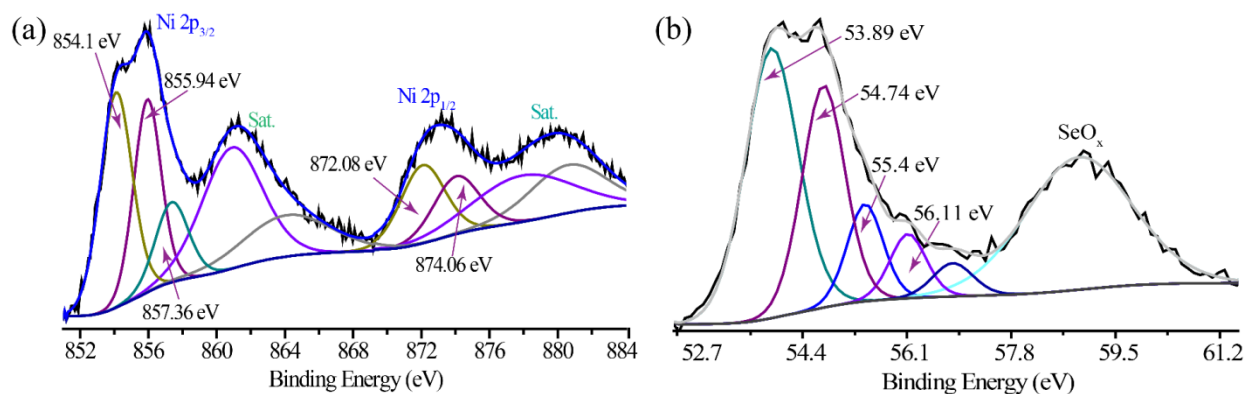
Figure 7. Deconvoluted XPS spectrum of p-NiSe/NGr: (a) Ni 2p region and (b) Se 3d region.

eV and 54.7 eV correspond to the Se $3d_{5/2}$ and Se $3d_{3/2}$ spin-orbit states of the nickel selenide.[11,16,22,33] The another peak doublets at higher binding energies (55.4 eV and 56.1 eV) could be attributed to the Se $3d_{5/2}$ and Se $3d_{3/2}$ states of elemental selenium, respectively. This finding suggested the presence of some elemental selenium on the surface, probably due to the deposition of small amounts of metalloid selenium within the carbon matrix during the selenization process.[11] The broad higher binding energy Se 3d peak at 58.9 eV is likely to be related to the selenium oxide, and this inference is consistent with the previous findings that the surface of metal selenides is prone to oxidation by air.[11,16,33]

In this way, our efforts at material characterizations through XRD, Raman, TEM, and XPS analyses confirm the successful selenization of nickel hydroxide along with the formation of trace amount of amorphous NiO_x and elemental Se. Based on these findings, it is expected that the catalyst system with nickel deficient selenide phase (Monoclinic, $Ni_{1-x}Se$) having embedded NiO_x and elemental selenium, developed in this study, could be a promising electrocatalyst for improving the overall performance of water electrolysis.

3.3.2. Electrochemical analysis

3.3.2.1. Electrocatalytic performance towards water oxidation

The oxygen evolution reaction (OER), following sequential proton-coupled four-electron transfer mechanism, is a thermodynamically as well as kinetically sluggish reaction that forms the perpetual bottleneck for the complete water electrolysis.[13] Interestingly, emerging studies uncover that the transition metal chalcogenides (TMCs) can be easily oxidized in strong alkaline

medium *via* an *in-situ* electrochemical oxidation process, producing nanoporous transition metal oxides (TMOs) which may result into improved water oxidation activity due to their increased active surface area and exposed electroactive sites.[35,36,37] These findings motivated us to study the OER performance of our catalyst along with revealing the structural transformation of the selenide system during the OER analysis.
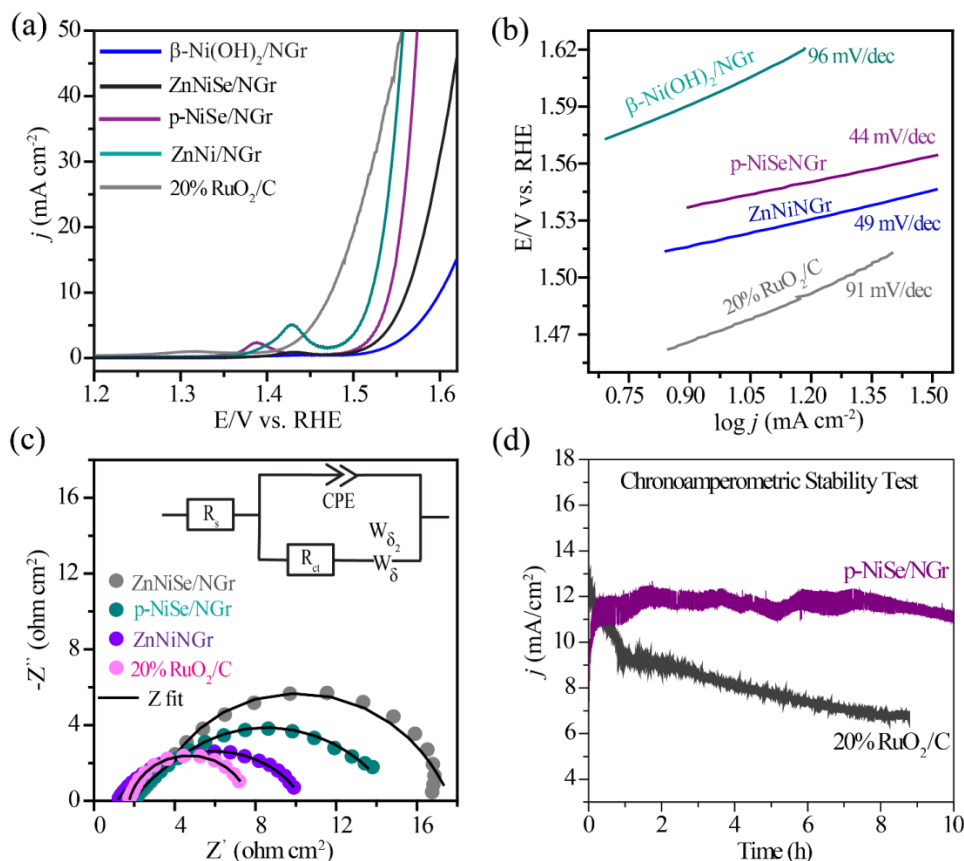
Figure 8. Comparative: (a) OER polarization curves recorded at 10 mV s^{-1} in N$_2$ saturated 1 M KOH, (b) the Tafel slopes corresponding to the conditions depicted in (a), (c) fitted Faradaic impedance spectra in Nyquist form (inset shows the equivalent circuit used), (d) chronoamperometric stability response for 10 h in 1 M KOH.

Figure 8a represents the LSV polarization curves for OER at 10 mV s^{-1} in 1 M KOH under N$_2$ atmosphere. The p-NiSe/NGr showed good OER performance with an overpotential of 311 mV from the thermodynamic water oxidation potential of 1.23 V (*vs.* RHE) to drag a 10 mA cm^{-2} current density (equivalent to the 10% solar to fuel conversion efficiency under one sun illumination, η_{10}) whereas the η_{10} value obtained for ZnNiSe/NGr and β-Ni(OH)$_2$/NGr are 330

mV and 370 mV, respectively. Although the η_{10} obtained for p-NiSe/NGr (311 mV) is little higher than that of ZnNi/NGr (290 mV) and 20% RuO$_2$/C (240 mV), the Tafel analysis (Figure 8b) revealed the comparable reaction kinetics of p-NiSe/NGr (44 mV decade^{-1}) with ZnNi/NGr (49 mV decade^{-1}). This could be probably attributed to the improved electronic properties of selenides over hydroxides. The kinetics of 20% RuO$_2$/C (91 mV decade^{-1}) is found to be lower than the above two described samples as given in Figure 8b.

The faster Faradaic process on the catalysts is also supported by the low R_{ct} value obtained during the Faradaic impedance analysis performed at 1.55 V *vs.* RHE (Figure 8c). The variation tendency of the R_{ct} is consistent with the overpotential obtained, which is merely 5.44 ohm cm^2 for 20% RuO$_2$/C followed by the 8.67 ohm cm^2, 11.68 ohm cm^2 and 14.75 ohm cm^2 R_{ct} values for ZnNi/NGr, p-NiSeNGr and ZnNiSe/NGr, respectively. Along with superior activity, p-NiSe/NGr catalyst also exhibited remarkable long-term stability during the continuous 10 h chronoamperometric analysis, maintaining a current density above 10 mA cm^{-2} throughout the test at an applied potential of 1.55 V *vs.* RHE (Figure 8d). Figure 8d also consists of the chronoamperometric stability plot for 20% RuO$_2$/C, presenting a continuous activity decrement, and retained mere ~50% activity after a 9 h experiment at 1.51 V *vs.* RHE.

3.3.2.2. Electrocatalytic performance toward hydrogen evolution reaction

According to the recent studies, similar to the active sites of hydrogenases, the cation sites of pyrite-type transition-metal dichalcogenides, *i.e.,* NiSe$_2$, have been suggested to be one of the most active centers towards HER. Moreover, Wang *et al.*[11] studied the role of elemental selenium towards HER, and through controlled experiments, they revealed that the excess of selenium in the NiSe$_2$ nanosheet surface acts as a promoter, facilitating the charge transfer on the surface to achieve efficient conversion of H$^+$ into H$_2$ bubbles. In addition to this, Liang *et al.*[38] investigated the mechanism of the HER on nickel by surface interrogation scanning electrochemical microscopy. On the basis of the combined analysis of the Tafel slope and surface hydrogen coverage, they suggested the rate determining step to be the adsorption of hydrogen (Volmer step) which is facilitated in the presence of the low-valence-state oxides of Ni compared to the metallic Ni. Hence, based on all these studies on selenides, it can be concluded

that the as-designed catalyst with $Ni_{1-x}Se$ phase along with the traces of NiO_x and elemental selenium could act as a good hydrogen evolution catalyst.
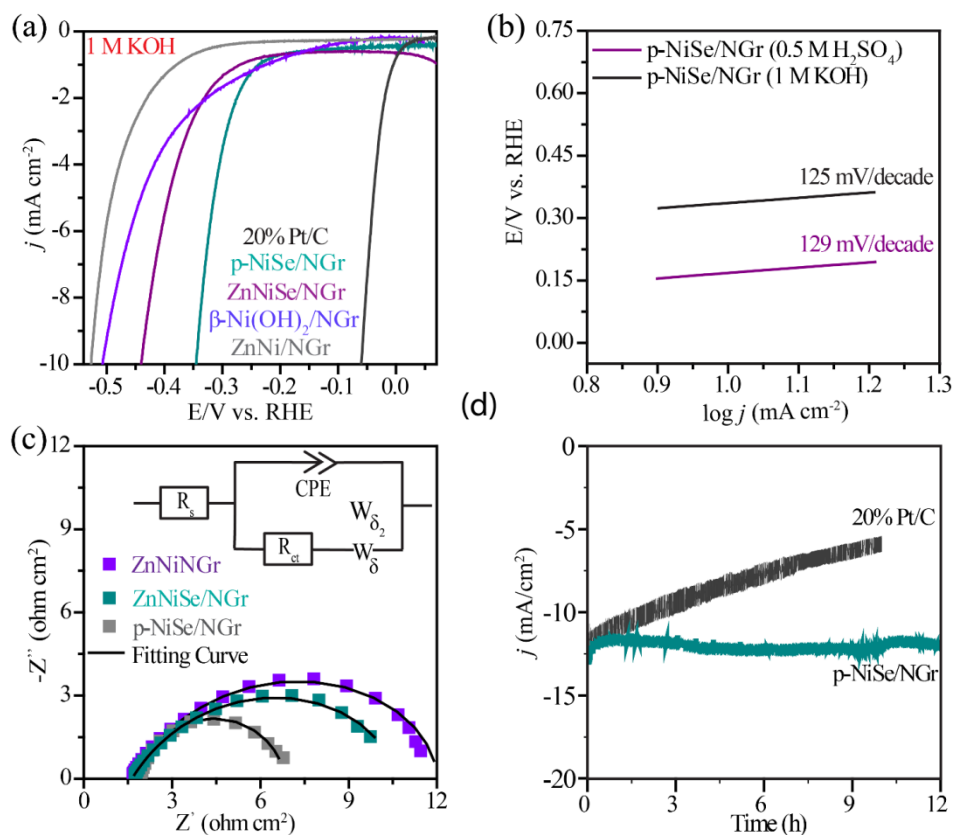
Figure 9. Comparative: (a) HER polarization curves recorded at 10 mV s^{-1} in N_2 saturated 1 M KOH, (b) the Tafel slopes corresponding to the conditions depicted in (a), (c) fitted Faradaic impedance spectra in Nyquist form (inset shows the equivalent circuit used), (d) chronoamperometric stability response of for 12 h in 1 M KOH.

Hence as a proof of concept study, herein, we have also studied the HER performance of our catalyst in alkaline electrolytes *via* linear sweep voltammetry (LSV) under N_2 atmosphere employing the rotating disk electrode (RDE) technique. Figure 9a illustrates the comparative HER polarization curves, recorded at a sweep rate of 10 mV s^{-1} on the reversible hydrogen electrode (RHE) scale. In 1 M KOH, our main catalyst, *i.e.,* p-NiSe/NGr, shows 276 mV negative potential shift to derive a current density of 10 mA cm^{-2} from the benchmark 20% Pt/C. For comparison, the HER performance of the other controlled samples was also studied in alkaline medium. Compared to ZnNi/NGr and β-Ni(OH)$_2$/NGr, ZnNiSe/NGr showed better HER

performance, indicating that the mere selenium presence in the system without any specific selenide phase has a positive impact on the HER performance (Figure 9a). However, ZnNiSe/NGr shows a 100 mV higher η_{10} value than that of p-NiSe/NGr in alkaline medium, indicating that a specific nickel selenide phase along with the open-edge structure plays a crucial role in improving the HER kinetics. With respect to the commercial catalyst employed, ZnNiSe/NGr, β-Ni(OH)$_2$/NGr and ZnNi/NGr exhibit η_{10} value of 380 mV, 447 mV, and 467 mV, respectively.

After the activity measurement, HER kinetics of the catalysts was studied through Tafel analysis. Comparative Tafel plots of p-NiSe/NGr and 20% Pt/C are presented in Figure 9b. In alkaline medium, p-NiSe/NGr showed a Tafel slope value of 125 mV decade^{-1} which is slightly higher than the value of 90 mV decade^{-1} for 20% Pt/C; however, this value is quite lower than the previous reports on the NiSe-based HER catalysts.[22,23] These Tafel slope values for both the aforementioned catalysts reveal that a Volmer-Heyrovsky pathway is probably controling the reaction rate.[39–42] The comparative reaction kinetics of all the controlled samples were also studied through Faradaic impedance measurement and a smaller charge transfer resistance (R_{ct}) of 4.89 ohm cm^2 for p-NiSe/NGr than those of ZnNiSe/NGr (8.0 ohm cm^2) and ZnNi/NGr (9.78 ohm cm^2), indicates improved electronic conductivity of p-NiSe/NGr due to specific selenization process (Figure 9c). The reliability of the catalysts was comparatively demonstrated through chronoamperometric analysis in 1 M KOH. p-NiSe/NGr at an applied voltage of 0.38 V maintained a current density of 12 mA cm^{-2} throughout the experiment with a negligible decrement in the current density even after 12 h of continuous operation (Figure 9d). However, 20% Pt/C at an applied potential of 0.060 V *vs*. RHE displays continual activity decay with only ~50% activity retention after 10 h of the test. In this way, our catalyst not only shows good activity but also high level of stability which is, in fact, far better than that of the benchmark Pt/C.

Hence, the p-NiSe/NGr, bearing porous, thin hexagonal open structure not only provides accessible active centers but also improves the diffusion of ionic species and thus allows the efficient utilization of active sites with consistent performance during the prolonged electrochemical analysis. Next, the Faradaic efficiency of the prepared catalyst toward hydrogen generation is determined by comparing the theoretical amount of H$_2$ produced with the experimental value obtained from the gas chromatography quantification.[43] The product gas

evolved was quantified by sampling out the product from an air-tight electrochemical cell after applying a current density of 5 mA cm^{-2} for 15 minutes whereas the theoretical value was calculated from the total charge passed, using Faraday's law (Equation 1). As illustrated in Figure 10a, the measured quantity of gas matches well with the theoretical value showing ~96.4% Faradaic efficiency (Equation 2).

Faradaic efficiency calculation for HER using Gas chromatography: Theoretically, the amount of product gas evolved was determined using Faraday's law[44]:

$$\text{Number of moles generated} = \frac{\text{Charge passed (C)}}{\text{Fraday Constant} \times \text{electron transferred per } H_2 \text{molecule}} \qquad (1)$$

On calculation, the number of moles of the product gas evolved was found to be 1.63 μmol.

$$\text{Faradaic efficiency } (\varepsilon) = \frac{\text{amount of product gas quantified from GC}}{\text{theoretical value determined from Faraday's law}} \times 100 \qquad (2)$$

3.3.2.3. Alkaline water electrolysis

The ability of our newly developed bifunctional catalyst to augment the overall water splitting was proved by fabricating and testing an alkaline water electrolyzer in 1 M KOH. The cathode and anode of the electrolyzer were prepared by coating the p-NiSe/NGr on carbon cloth (1×4 cm^2) of 1 cm^2 area with a mass loading of 1 mg cm^{-2} and is designated as (p-NiSe/NGr)-CC. For comparison, a controlled alkaline electrolyzer using the benchmark 20% Pt/C (as a cathode) and 20% RuO$_2$/C (as an anode) was also fabricated with the same loading of 1 mg cm^{-2} over CC and designated as (Pt/C)-CC∥(RuO$_2$/C)-CC. Figure 10b represents the comparative LSV polarization curves for complete water electrolysis at a scan rate of 10 mV s^{-1} in 1 M KOH. The LSV curves for (p-NiSe/NGr)-CC and (Pt/C)-CC∥(RuO$_2$/C)-CC showed that voltage of 1.60 V and 1.62 V were sufficient to generate 5 mA cm^{-2} current density toward the complete water electrolysis using our catalyst system and the benchmark system, respectively. In addition, (p-NiSe/NGr)-CC and (Pt/C)-CC∥(RuO$_2$/C)-CC achieved the current density of 10 mA cm^{-2} at a voltage of 1.69 V and 1.70 V, respectively.
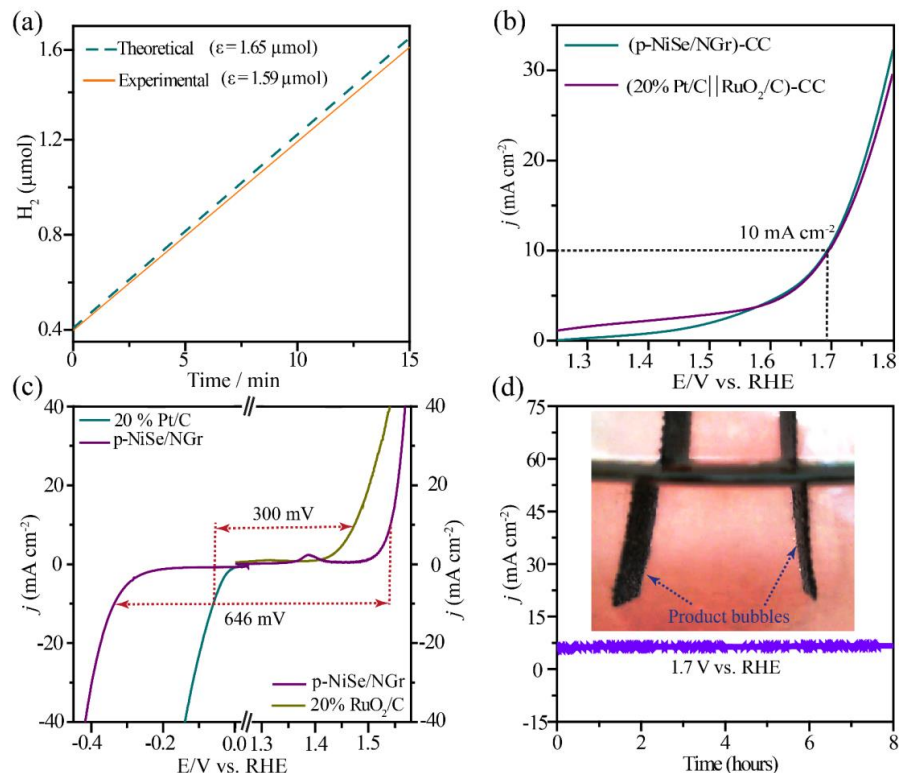
Figure 10. (a) Comparative plots for the experimentally and theoretically generated moles of H_2 at a constant current density of 5 mA cm^{-2} for 15 minutes, (b) comparative polarization curves of the whole-cell water electrolysis in 1 M KOH at a scan rate of 10 mV s^{-1}, (c) comparative and combined HER and OER polarization curves at 10 mV s^{-1} of p-NiSe/NGr, 20% Pt/C and 20% RuO_2/C, (d) chronoamperometric stability test for the whole-cell water electrolysis in 1 M KOH (inset shows the picture captured during the electrolysis showing the product bubbles attached to the catalyst-coated carbon cloth).

Noticeably, the whole-cell performance of the commercial catalyst-based electrolyzer ((Pt/C)-CC∥(RuO₂/C)-CC) is found to be lower than their respective half-cell performances, *i.e.,* the overpotential obtained for the full water electrolysis is found to be higher than the overpotential sum of 20% Pt/C towards HER and 20% RuO_2/C towards OER (Figure 10c). Whereas, in the case of (p-NiSe/NGr)-CC, the overall water electrolysis performance is found to be improved to a reasonable extent from their respective half-cell reaction performances, as are comparatively illustrated in Figure 10c. It was difficult to ascertain the exact reason for such an interesting finding; however, a probable reason for this anomaly could be the formation of electrocatalytically active species through the counter redox reactions occurring at the Ni centers

of p-NiSe/NGr during the two-electrode reactions. In our catalyst architecture, the H_2 production involves water reduction followed by $Ni(OH)_2$ oxidation to the OER-active NiOOH phase ($Ni(OH)_2 \rightarrow NiOOH$), facilitating the counter water oxidation reaction to evolve O_2 which is followed by the back reduction of NiOOH to lower oxidation state Ni moieties, *i.e.,* $Ni(OH)_2$ that is having better water reduction potential.[45-47] In sharp contrast, the $(Pt/C)-CC \parallel (RuO_2/C)-CC$ electrolyzer system is a hybrid system where the two electrode catalysts show poor performance towards their counter electrode reactions, and hence show no such type of synergy that can mutually improve the overall electrolyzer performance.
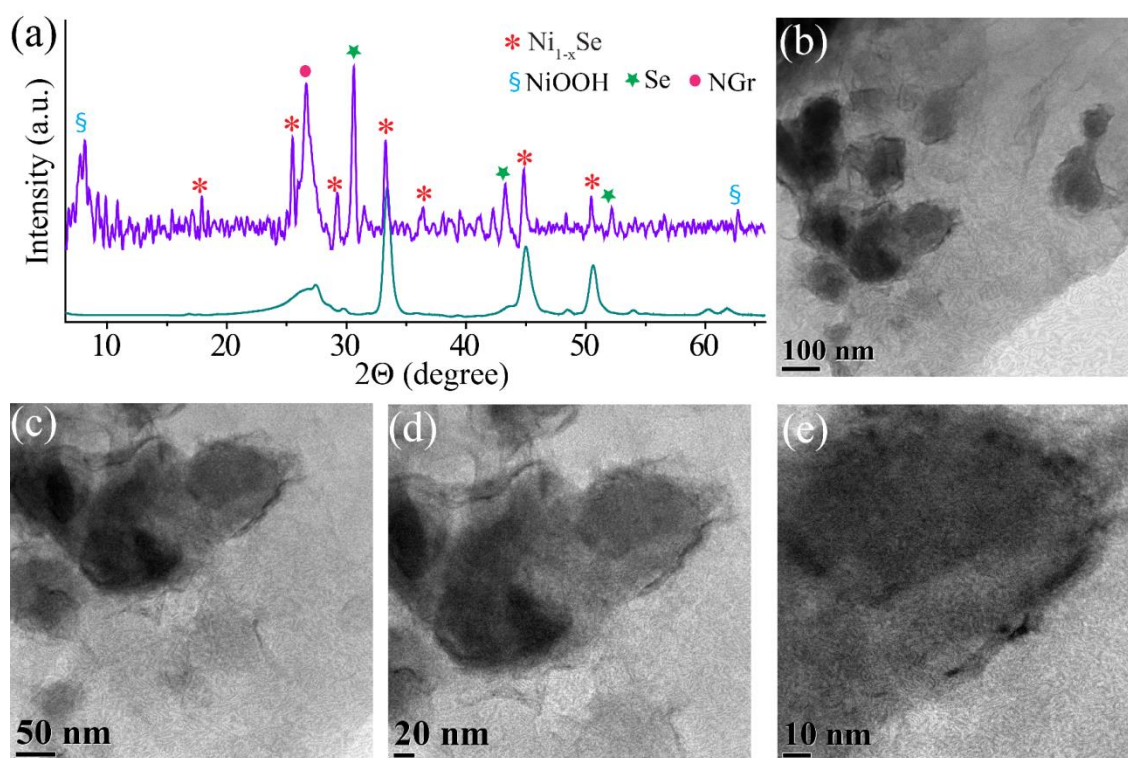
Figure 11. (a) Comparative XRD patterns of p-NiSe/NGr before and after the water electrolysis stability test, (b), (c), (d) and (e) are the TEM images of p-NiSe/NGr after the water electrolysis stability test at different magnifications representing the agglomeration, distortion as well as connection between the nearby hexagonal selenide nanoplates.

The stability test for (p-NiSe/NGr)-CC-based electrolyzer was performed through the chronoamperometry technique for 8 h at 1.7 V showing that a current density above 5 mA cm^{-2} was maintained throughout the analysis (Figure 10d). After the whole-cell electrolysis stability

study, the XRD pattern of p-NiSe/NGr confirmed the presence of nickel in various chemical environments such as the OER active NiOOH phase that can generate during the water reduction reaction and the exposure of metallic Se, indispensable in facilitating the charge transfer during HER (Figure 11a).[11] Interestingly, the post stability TEM images showed agglomeration, distortion as well as connection between the nearby hexagonal selenide nanoplates (Figure 11b and 11c). The TEM images also gave clear evidence for the formation of amorphous layers over the selenides, which could probably be the α-Ni(OH)$_2$/NiOOH moieties (Figure 11d and 11e).

3.4. Conclusion

In this study, we synthesized nickel selenide-N-doped graphene nanocomposite using ZnNi-LDH/NGr as a precursor resulting in the formation of porous hexagonal nickel selenide nanoplates. These unique structural features that contain crystalline monoclinic nickel selenide phases along with amorphous NiO$_x$ and metallic selenium embedded in the NGr matrix endowed our catalyst system with short charge transport distances, abundant exposed active centers, improved mass transfer properties and high structural stability against agglomeration, resulting in the good activity as well as stability towards whole-cell water electrolysis in alkaline medium. The results indicate that nickel selenide designed with an open and porous structure holds significant promise for the rational design of non-precious bifunctional electrocatalysts for overall water splitting.

3.5. References

1   M. T. M. Koper, *Nat. Chem.,* 2013, **5**, 255–256.
2   B. Obama, *Science,* 2017, **355**, 126–129.
3   Z. W. Seh, J. Kibsgaard, C. F. Dickens, I. Chorkendorff, J. K. Nørskov, T. F. Jaramillo, *Science,* 2017, **355**.
4   V. M. Dhavale, S. K. Singh, A. Nadeema, S. S. Gaikwad, S. Kurungot, *Nanoscale,* 2015, **7**, 20117–20125.
5   S. M. Unni, S. N. Bhange, B. Anothumakkool, S. Kurungot, *ChemPlusChem,* 2013, **78**, 1296–1303.
6   J. W. D. Ng, Y. Gorlin, T. Hatsukade, T. F. Jaramillo, *Adv. Energy Mater,.* 2013, **3**, 1545–1550.
7   X. Li, X. Hao, A. Abudula, G. Guan, *J. Mater. Chem. A,* **2016**, *4*, 11973–12000.
8   J. W. D. Ng, T. R. Hellstern, J. Kibsgaard, A. C. Hinckley, J. D. Benck, T. F. Jaramillo, *ChemSusChem,* 2015, **8**, 3512–3519.
9   N. Cheng, S. Stambula, D. Wang, M. N. Banis, J. Liu, A. Riese, B. Xiao, R. Li, T.-K. Sham, L.-M. Liu, G. A. Botton, X. Sun, *Nat. Commun.,* 2016, **7**, 13638–13646.
10   A. T. Swesi, J. Masud, M. Nath, *Energy Environ. Sci.,* 2016, **9**, 1771–1782.
11   F. Wang, Y. Li, T. A. Shifa, K. Liu, F. Wang, Z. Wang, P. Xu, Q. Wang, J. He, *Angew. Chem. Int. Ed.,* 2016, **55**, 6919–6924.
12   X. Li, G.-Q. Han, Y.-R. Liu, B. Dong, W.-H. Hu, X. Shang, Y.-M. Chai, C.-G. Liu, *ACS Appl. Mater. Interfaces,* 2016, **8**, 20057–20066.
13   N.-T. Suen, S.-F. Hung, Q. Quan, N. Zhang, Y.-J. Xu, H. M. Chen, *Chem. Soc. Rev.,* 2017, **46**, 337–365.
14   D. Liu, Q. Lu, Y. Luo, X. Sun, A. M. Asiri, *Nanoscale,* 2015, **7**, 15122–15126.

15   H. Liang, L. Li, F. Meng, L. Dang, J. Zhuo, A. Forticaux, Z. Wang, S. Jin, *Chem. Mater.,* 2015, **27**, 5702–5711.
16   F. Ming, H. Liang, H. Shi, X. Xu, G. Mei, Z. Wang, *J. Mater. Chem. A,* 2016, **4**, 15148–15155.
17   B. You, N. Jiang, M. Sheng, S. Gul, J. Yano, Y. Sun, *Chem. Mater.,* 2015, **27**, 7636–7642.
18   M. Gao, W. Sheng, Z. Zhuang, Q. Fang, S. Gu, J. Jiang, Y. Yan, *J. Am. Chem. Soc.,* 2014, **136**, 7077–7084.
19   J. Ren, M. Antonietti, T.-P. Fellinger, *Adv. Energy Mater.,* 2015, **5**, 1401660.
20   Y. Yang, H. Fei, G. Ruan, C. Xiang, J. M. Tour, *ACS Nano,* 2014, **8**, 9518–9523.
21   H. Li, S. Chen, H. Lin, X. Xu, H. Yang, L. Song, X. Wang, *Small,* 2017, **13**, 1701487.
22   X. Li, L. Zhang, M. Huang, S. Wang, X. Li, H. Zhu, *J. Mater. Chem. A,* 2016, **4**, 14789–14795.
23   I. H. Kwak, H. S. Im, D. M. Jang, Y. W. Kim, K. Park, Y. R. Lim, E. H. Cha, J. Park, *ACS Appl. Mater. Interfaces,* 2016, **8**, 5327–5334.
24   D. C. Marcano, D. V. Kosynkin, J. M. Berlin, A. Sinitskii, Z. Sun, A. Slesarev, L. B. Alemany, W. Lu and J. M. Tour, *ACS Nano*, 2010, **4**, 4806-4814.
25   N. Ayasha, V. M. Dhavale, S. Kurungot, *Nanoscale,* 2017, **9**, 12590–12600.
26   B. Hu, S.-F. Chen, S.-J. Liu, Q.-S. Wu, W.-T. Yao, S.-H. Yu, *Chem. Eur. J.,* 2008, **14**, 8928–8938.
27   X. Wang, J. Hu, W. Liu, G. Wang, J. An, J. Lian, *J. Mater. Chem. A,* 2015, **3**, 23333–233344.
28   D. S. Hall, D. J. Lockwood, C. Bock, B. R. MacDougall, *P ROY SOC A-MATH PHY,* 2015, **471.**
29   U. Subbarao, V. S. Marakatti, M. K. Amshumali, B. Loukya, D. K. Singh, R. Datta, S. C. Peter, *J. Solid State Chem.,* 2016, **244**, 84–92.
30   S. Kukunuri, M. R. Krishnan, S. Sampath, *Phys. Chem. Chem. Phys.,* 2015, **17**, 23448–23459.
31   Z. Zafar, Z. H. Ni, X. Wu, Z. X. Shi, H. Y. Nan, J. Bai, L. T. Sun, *Carbon,* 2013, **61**, 57–62.
32   D. S. Hall, D. J. Lockwood, S. Poirier, C. Bock, B. R. MacDougall, *J. Phys. Chem. A,* 2012, **116**, 6771–6784.
33   X. Xu, F. Song, X. Hu, *Nat. Commun.,* 2016, **7**, 12324.
34   W. Liu, C. Lu, X. Wang, K. Liang, B. K. Tay, *J. Mater. Chem. A,* 2015, **3**, 624–633.
35   W. Chen, Y. Liu, Y. Li, J. Sun, Y. Qui, C. Liu, G. Zhou, Y. Cui, *Nano Lett.,* 2016, **16**, 7588–7596.
36   C. Tang, N. Cheng, Z. Pu, W. Xing, X. Sun, *Angew. Chem. Int. Ed.,* 2015, **54***, 9351–9355.
37   R. Bose, V. R. Jothi, D. B. Velusamy, P. Arunkumar, S. C. Yi, *Part. Part. Syst. Charact.,* 2018, **1800135**.
38   Z. Liang, H. S. Ahn, A. J. Bard, *J. Am. Chem. Soc.,* 2017, **139**, 4854–4858.
39   J. Durst, A. Siebel, C. Simon, F. Hasche, J. Herranz, H. A. Gasteiger, *Energy Environ. Sci.,* 2014, **7**, 2255–2260.
40   M. Zeng, Y. Li, *J. Mater. Chem. A,* 2015, **3**, 14942–14962.
41   M. Gong, W. Zhou, M.-C. Tsai, J. Zhou, M. Guan, M.-C. Lin, B. Zhang, Y. Hu, D.-Y. Wang, J. Yang, S. J. Pennycook, B.-J. Hwang, H. Dai, *Nat. Commun.,* 2014, **5**, 4695.
42   H. Jin, J. Wang, D. Su, Z. Wei, Z. Pang, Y. Wang, *J. Am. Chem. Soc.,* 2015, **137**, 2688–2694.
43   C. C. L. McCrory, S. Jung, I. M. Ferrer, S. M. Chatman, J. C. Peters, T. F. Jaramillo, *J. Am. Chem. Soc.,* 2015, **137**, 4347–4357.
44   B. Anothumakkool, A. Torris A T, S. N. Bhange, M. V. Badiger, S. Kurungot, *Nanoscale,* 2014**, 6**, 5944–5952.
45   L. Chen, X. Dong, Y. Wang, Y. Xia, *Nat. Commun.,* 2016, **7**, 11741.
46   N. Danilovic, R. Subbaraman, D. Strmcnik, K.-C. Chang,; A. P. Paulikas, V. R. Stamenkovic, N. M. Markovic, *Angew. Chem. Int. Ed.,* 2012, **51**, 12495–12498.
47   L. Trotochaud, S. L. Young, J. K. Ranney, S. W. Boettcher, *J. Am. Chem. Soc.,* 2014, **136**, 6744–6753.

Chapter 4

[MoS$_4$]$^{2-}$-Intercalated NiCo Layered Double Hydroxide Nanospikes/Ni Foam to Generate Cheaper H$_2$ Directly from Urea-Rich Wastewater*

This chapter describes a strategy of substituting the energy-uphill water oxidation with readily oxidizable urea-rich urine to construct a ground-breaking bridge, combining the energy-efficient hydrogen generation and environmental protection. Designing of a robust multifunctional electrocatalyst is desirable for the widespread implementation of this waste to fuel technology. In this context, here, we propose a simple tuning of the electrocatalytically favorable characteristics of NiCo LDH by introducing [MoS$_4$]$^{2-}$ in its interlayer space. This insertion induces overall electronic structure tuning of the hydroxide layers in such a way that, the designed catalyst exhibits favorable kinetics toward all the required reactions of hydrogen generation. This is why, our homemade catalyst, when utilized both as a cathode and anode to fabricate a urea electrolyzer, it requires a mere ~1.37 V cell potential to generate sufficient H$_2$ by reaching the benchmark 10 mA cm^{-2} in 1 M KOH/0.33 M urea. Other indispensable reason of selecting [MoS$_4$]$^{2-}$ is its high-valent nature making the catalyst highly selective and insensitive to common catalyst-poisoning toxins of urine. This is experimentally supported by performing the real urine electrolysis, where our catalyst shows similar performance to that of synthetic urea, offering its industrial value.
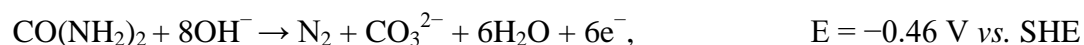
_____
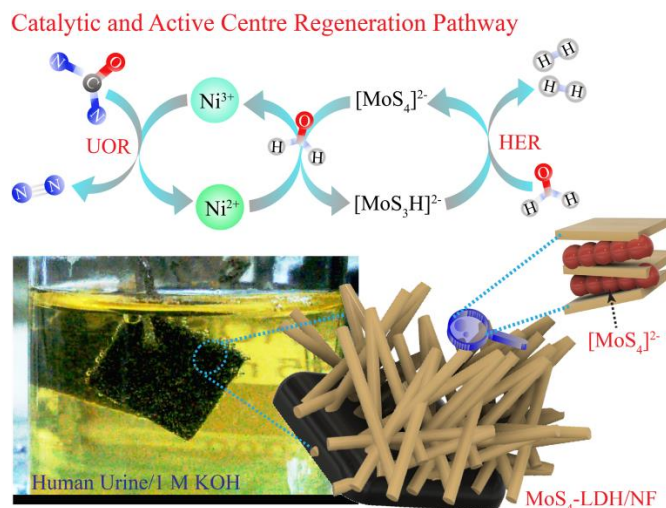
4.1. Introduction

A switch from today's hydrocarbon economy to hydrogen economy, having highest gravimetric energy density (~140 MJ/Kg), has gained sufficient momentum in recent years to mitigate the issues associated with the current energy scenario.[1,2] This transition, however, depends upon our efforts of providing cheaper and renewable source of hydrogen and the best solution is water.[3,4,5] However, poor energy efficiency of this process, owing to the sluggish water oxidation (WOR) kinetics[4,6,7] as well as its poisoning effect on H_2-generating half-cell[8,9], is hampering its widespread application. Among various efforts, replacing the energy-uphill water oxidation half-cell with readily oxidizable molecules, *e.g.,* alcohols,[10,11] hydrazine,[12] urea[13,14] *etc.,* has emerged as one of the potential substitutes to make the H_2 production energy-efficient. Among which, the urea oxidation (UOR) not only makes the H_2 production energy-efficient but also allows the denitrification of urea-rich wastewater, which otherwise naturally hydrolyzes into pollutants such as ammonia and nitrates, creating adverse health issues and water reservoir eutrophication.[13,14] In addition, urea electrolysis provides one of the ways to deal with the competing oxygen reduction reaction during hydrogen generation to improve the energy efficiency of the process. [8,9] It also offers one of the potential ways to avoid the mixing of two explosive product gases of water electrolysis, *i.e.,* H_2 and O_2.[15] Most importantly, urea electrolysis in alkaline medium, thermodynamically shifts the potential from 1.23 V to a mere 0.37 V, theoretically generating 70% cheaper hydrogen.[14] Hence, urea can be a promising hydrogen carrier in the development of sustainable hydrogen economy.

In spite of a number of factors in favor of replacing WOR with UOR, challenges lie in the complexity of the six-electron transferred urea oxidation, undergoing sluggish kinetics and restricting its widespread implementation.[16,17,18] On the basis of the available literatures, in alkaline medium, urea electrolysis takes place as follows:[14,16]
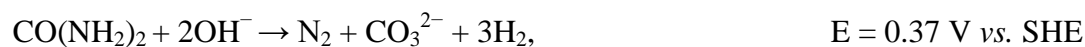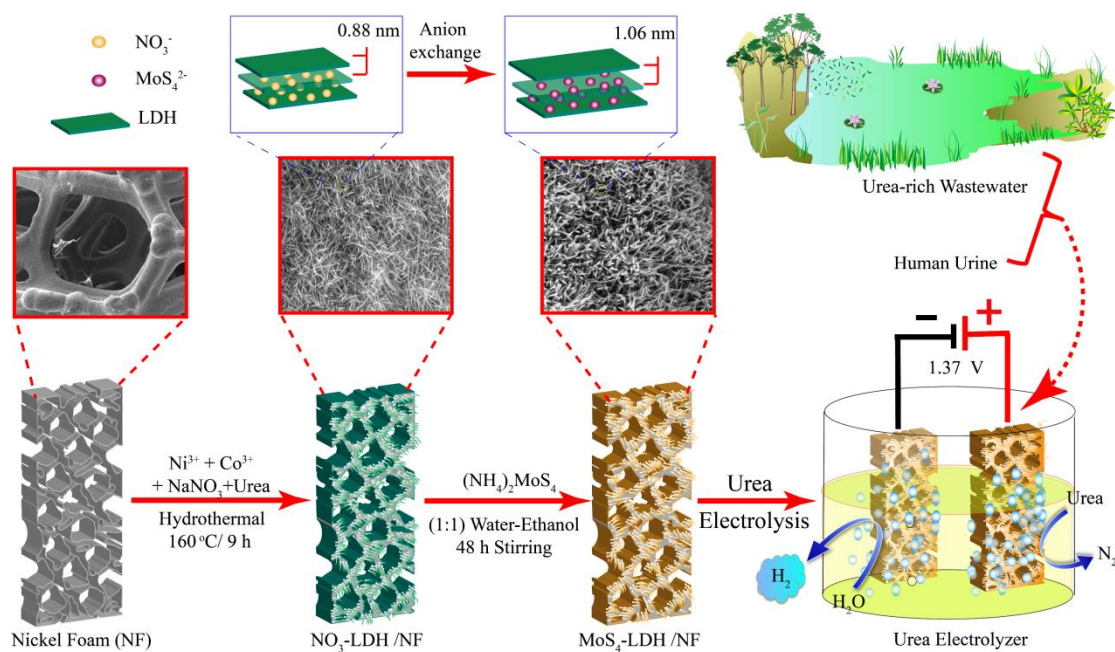
Anode:

$$CO(NH_2)_2 + 8OH^- \rightarrow N_2 + CO_3^{2-} + 6H_2O + 6e^-, \qquad E = -0.46 \text{ V } vs. \text{ SHE}$$

Cathode:

$$6H_2O + 6e^- \rightarrow 3H_2 + 6OH^-, \qquad E = -0.83 \text{ V } vs. \text{ SHE}$$

Overall:

$$CO(NH_2)_2 + 2OH^- \rightarrow N_2 + CO_3^{2-} + 3H_2, \qquad E = 0.37 \text{ V } vs. \text{ SHE}$$

Scheme 1. Representation of the steps involved in the synthesis of MoS$_4$-LDH/NF and the schematic illustration of our waste to fuel generation strategy.

Although UOR can be efficiently catalyzed by Pt- and Rh-based catalysts, their high cost and scarcity make the process impractical.[14] Considering this, the designing of an ideal catalyst, composed of least-toxic, earth-abundant elements, economical to manufacture and electrochemically stable, is crucial. In this context, a number of efforts have been directed, such as NiCo compounds,[18] 2D MnO$_2$ crystals,[19] Ni(OH)$_2$ nanostructures,[17,20] and NiMo-based nanostructures[21,22]. In all these cases, UOR is found to decrease the overall energy consumption of H$_2$ generation as compared to that of WOR. However, none of these catalysts has been demonstrated to utilize real urine directly for H$_2$ generation, the ultimate mandate to commercialize this waste to fuel technology. The probable reason for this limitation is their poor selectivity as well as instability in presence of common catalyst inhibitors of urine, *e.g.,* CO, proteins, creatinine, phosphates, and so forth.[23] Hence, it is of paramount to design a catalyst providing good selectivity as well as reasonable activity toward urea/urine electrolysis along with remarkable durability. In this context, Dey's group, in one of their works, demonstrated the unprecedented role of ammonium tetrathiomolybdate (ATTM) toward catalyzing highly selective H$^+$ reduction while maintaining the long-term catalytic efficiency even in presence of common catalyst inhibitors, e.g., CO, S^{2-}/HS of natural water bodies.[9] Keeping this finding into account, we thought of incorporating [MoS$_4$]$^{2-}$ anion with WOR/UOR-active materials to design a multifunctional robust catalyst for H$_2$ generation directly from real urine. Among the various WOR/UOR active materials, layered double hydroxides (LDHs) are found to best fulfill the requirement of designing such kind of electrocatalysts,

owing to their tunable structure, chemical environment and electronic properties.[24,25,26,27,28] For instance, α-Ni(OH)$_2$ and its oxidized form, *i.e.,* γ-NiOOH, are the building blocks of the Ni-based LDHs,[25] and have shown outstanding role toward catalyzing the two half-cell reactions of water electrolysis.[29,30,31] For example, Subbaraman *et al.*[32] corroborate the essential OH-acceptor role of the Ni(OH)$_2$ moieties over Pt sites toward improving the HER kinetics of Pt in alkaline medium. In addition, WOR-promoting role of γ-NiOOH[30] and other (oxy)hydroxides (*e.g.,* NiFe (oxy)hydroxides[33], CoFe(oxy)hydroxides[34] *etc.*) are well documented. In spite of that, the essential role of Ni(OH)$_2$/NiOOH toward urea/urine oxidation is thoroughly investigated by Bryan *et al.*[14]

Thus, our strategy for the [MoS$_4$]$^{2-}$ intercalation in the NiCo-LDH interslab may full-fill the requirement of an ideal catalyst to boost up the overall urea/urine electrolysis *via* an efficient catalytic interface generated between the interlayer [MoS$_4$]$^{2-}$ moieties and LDH. The obtained catalyst showed efficient performance toward the all required reactions of hydrogen generation in alkaline medium. The fabricated whole-cell urea electrolysis device required a mere 1.37 V to generate sufficient amount of H$_2$ by achieving the benchmark 10 mA cm^{-2} current density. Interestingly, our catalyst works just as well with real urine, representing the proficiency of the catalyst system towards the utilization of waste for generating useful fuel.

4.2. Experimental Section

4.2.1. Synthesis of NO$_3$-intercalated NiCo-LDH/NF: The NO$_3$-intercalated NiCo-LDH nanospike arrays were directly grown over the nickel foam (NF, in all the upcoming sections) by a single-step hydrothermal method in presence of excess NaNO$_3$ (Scheme 1). The NF was first cleaned by 3 M HCl solution, water, and ethanol. The synthesis procedure involves the dissolution of 1 mmol of Ni(NO$_3$)$_2$·6H$_2$O and 2 mmol of Co(NO$_3$)$_2$·6H$_2$O in 100 mL DI-water; subsequently, urea was added in a molar ratio of 1:5 of the metal ions to urea. Afterward, NaNO$_3$ was added to the above solution in the ratio of 1:2 of the metal ions to NaNO$_3$ and the solution mixture was transferred into a Teflon lined stainless steel autoclave. 6 pieces of cleaned NFs (1 × 2 cm^2) were immersed into the reaction solution and heated at 170 ^{o}C for 12 h. After the 12 h reaction, the autoclave was allowed to cool down naturally and the as-modified NFs were washed *via* bath sonication for 10 min using ethanol-water mixture. Finally, the sample was dried at 60 ^{o}C for 8 h and denoted as NO$_3$-LDH/NF in all the upcoming sections. The mass loading of NO$_3$-LDH-nanospikes over NF was found to be ~1 mg/cm^2 as determined by weighing the NF before and after the hydrothermal treatment. The powdered NO$_3$-LDH was synthesized by adopting the same above-mentioned procedure without adding any NF.

4.2.2. Conversion of NO_3^- to $[MoS_4]^{2-}$-intercalated NiCo-LDH/NF: The NO_3^- to $[MoS_4]^{2-}$ anion exchange was performed by adopting ethanol-assisted approach to effectively minimize the carbonate contamination from the atmosphere and promote the anion exchange. Typically, all 6 pieces of the as-grown NO_3-LDH/NF were immersed in degassed ethanol/water binary solution (1:1 v/v) containing 100 mg of ammonium tetrathiomolybdate (ATTM). After purging with N_2, the vessel was tightly sealed and kept for stirring for 48 h at room temperature. Afterward, the material was washed thoroughly with ethanol/water mixture *via* 10 min bath sonication and dried at 60 ^{o}C for 8 h (the sample is denoted as MoS_4-LDH/NF in all the upcoming sections). Lastly, any change in the mass loading of NO_3-LDH/NF after anion exchange was determined by weighing the MoS_4-LDH/NF and found on an average a little increment in the mass loading from ~1 to ~1.2 mg cm^2.

4.2.3. Synthesis of (CO_3^{2-})-intercalated NiCo-LDH: The carbonate-intercalated NiCo-LDH (CO_3-LDH) was synthesized by adopting the same method as applied for the synthesis of NO_3-LDH, just by replacing the nitrate metal salts with chloride salts and without adding any $NaNO_3$. All the unsupported catalyst is synthesized without immersing NF into the reaction solution.

4.3.   Results and discussion

4.3.1. Structure and Morphology of the Catalyst

One-dimensional solid nanospike networks of $[MoS_4]^{2-}$-intercalated NiCo-LDHs were directly grown over conducting nickel foam by following a simple two-step synthesis process (Scheme 1).

4.3.1.1. X-ray diffraction analysis

First of all, to confirm the LDH formation as well as NO_3^{2-} insertion, the X-ray diffraction analysis (XRD) was performed. Owing to the strong XRD diffraction peaks from the NF substrate, the (*00l*) planes of LDH may get suppressed and indistinguishable. Due to this reason, the XRD pattern was first analyzed on powdered NO_3-LDH, which shows well-defined (003) and (006) LDH planes (Figure 1a). The center of the (003) plane gave a d-spacing value of 0.88 nm, confirming the successful formation of the NO_3-intercalated NiCo-LDH.[24,35] Later on, for assuring the NO_3-LDH growth over NF, XRD pattern was also performed on NO_3-LDH/NF, exhibiting ill-defined all (*00l*) planes of LDH over NF (Figure 1b). Although the intercalation-deciding (003) plane showed diminished intensity, the position of the (006) plane matches well with that of the unsupported system, affirming the successful growth of NO_3-LDH over NF. After confirming the NO_3-LDH formation, both unsupported and NF-supported sample

were subjected to ethanol-assisted $[MoS_4]^{2-}$ anion exchange process in degassed ethanol-water mixture (1:1, volume ratio) with constant 48 h stirring at ambient atmosphere.

Figure 1a also comprises the XRD pattern of the powdered MoS_4-LDH, depicting a clear increment of the (003) basal spacing from 0.88 nm to 1.06 nm, owing to the expansion of the NiCo-LDH unit cell along the c-axis.[36,37] The XRD analysis when extended on MoS_4-LDH/NF, showed poorly-defined (*00l*) planes due to the increased amorphousness after the anion exchange process (Figure 1b). In fact, the (003) plane gets totally unresolved. Nevertheless, the lower 2 theta value shift of the other Bragg reflections, *i.e.,* the (006), (101) and (015) planes, clearly indicates the introduction of larger $[MoS_4]^{2-}$ moieties in the LDH interslab.[36] Figure 1a also comprises the XRD pattern of the carbonate intercalated-LDHs having a d-spacing of 0.74 nm. It is synthesized using chloride metal salts with no $NaNO_3$ (abbreviated as CO_3-LDH).[38] The intention to show the comparative XRD analysis of NO_3-LDH and CO_3-LDH is to support our efforts of minimizing the number of synthesis steps by synthesizing direct NO_3^--intercalated LDHs which otherwise needs an extra step *via* NO_3^- anions exchange from CO_3-LDH. [24,36]
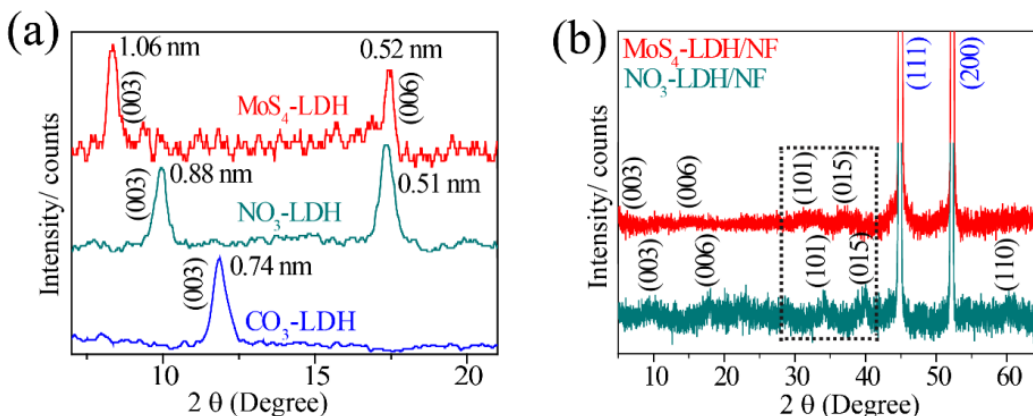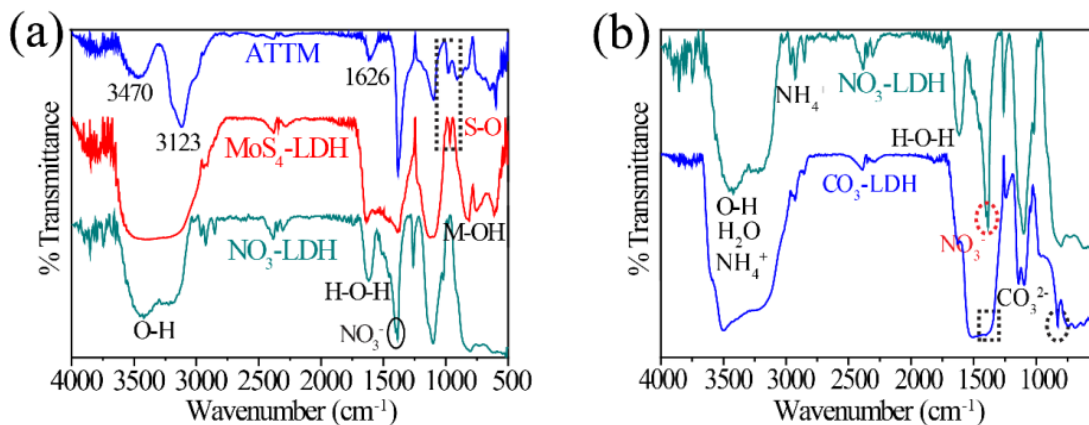

Figure 1. Comparative XRD patterns: (a) powdered samples and (b) the Ni foam-supported samples.

4.3.1.2. Fourier-transform infrared spectroscopy analysis

To verify the types of the anion existing in the LDH interlayer, IR spectroscopy analysis was performed on the powdered samples. For NO_3-LDH, the strong band appearing at 1384 cm^{-1} corresponds to the interlayer NO_3^- ions (Figure 2a).[37] To further support the major intercalated species as NO_3^- anions, FTIR analysis was extended on CO_3-LDH (Figure 2b). In case of CO_3-LDHs, the broad band starting near 1365 cm^{-1} unlike the sharper NO_3^- band affirms the success of our synthesis strategy.[38] After the $[MoS_4]^{2-}$ anion exchange process, the NO_3^- band is found to get merged with the ATTM absorption bands, suggesting almost-complete exchange (Figure 2a). Moreover, a weak band positioned at ~984

cm^{-1} is encountered in both ATTM and MoS_4-LDH, corresponding to the characteristic S-O absorption band, probably resulting from the slow oxidation at the sulfur centers.[39] Furthermore, the increased broadness of the –OH band after the anion exchange, supports the XRD finding of the increased interslab space, incorporating excess amount of interlayer water molecules.

Figure 2. Comparative FTIR data: (a) and (b) are the comparative FTIR patterns for the powdered samples.

## 4.3.1.3. Field-emission scanning electron microscopy analysis

The adopted hydrothermal growth of NO_3-LDH over the Ni foam resulted into the formation of dense, vertically grown nanospikes-like structure with quite good uniformity in size and diameter. Such a growth pattern is first examined through field-emission scanning electron microscopy (FE-SEM). Figure 3a displays the vertically-grown NO_3-LDH-nanospikes over NF which can be clearly differentiated from the bare NF (inset of Figure 3a). The higher magnification image further clarifies the vertical growth of nanospikes (Figure 3b) as compared to the smooth surface of bare NF (inset of Figure 3b). As visible from Figure 3c, the anion-exchange process does not alter the morphology much, except little increased amorphousness and hence thickness of the nanospikes. Figure 3d is the higher-magnification SEM image of MoS_4-LDH/NF, representing the loose nanospikes-texture and open spaces between the neighboring nanospikes. Such kind of designed catalyst texture can effectively facilitate the electrolyte-infiltrations for the maximum utilization of engraved active sites to boost-up the overall electrochemical performance.
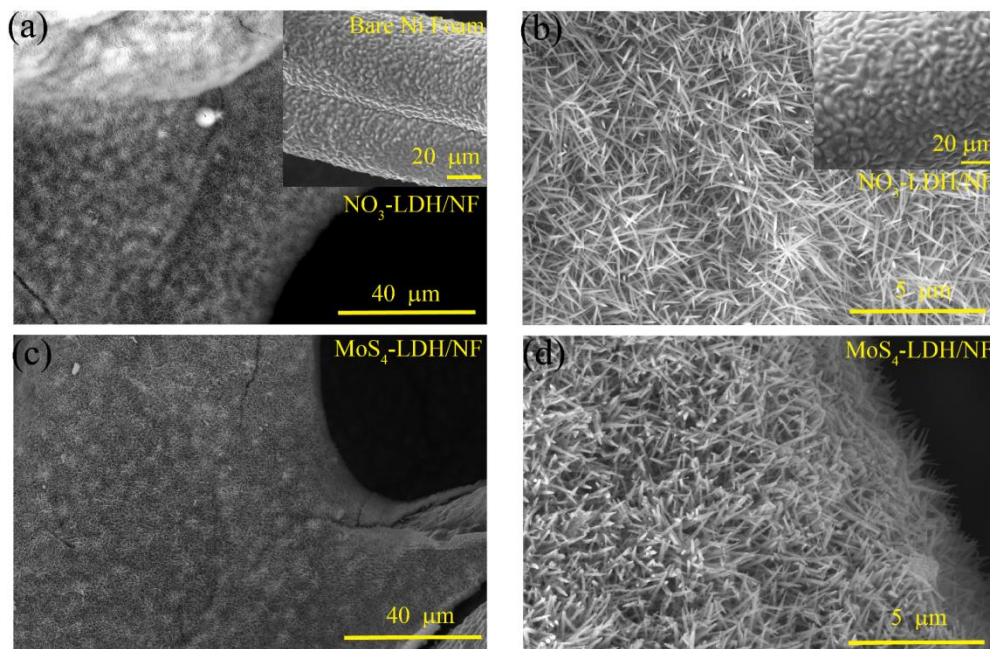
Figure 3. FESEM images: (a) and (b) represent the low and high magnification images of NO$_3$-LDH/NF, and (c) and (d) display the low and high magnification images for MoS$_4$-LDH/NF. The inset images in panel (a) and (b) represent the SEM images of the bare Ni foam at two different magnifications.

4.3.1.4. Transmission electron microscopy analysis

The transmission electron microscopy (TEM) analysis relocates the one-dimensional nanospikes-like morphology in both NO$_3$-LDH (Figure 4a) and MoS$_4$-LDH (Figure 4b) with the diameter ranging from 50-70 nm. The higher magnification TEM image of NO$_3$-LDH (Figure 4c) identifies a d-spacing of 0.88 nm. However, in case of MoS$_4$-LDH, owing to the highly amorphous and hydrated surface texture, the burning of sample from the high energy electron beam is encountered. This is why, high-resolution TEM analysis was employed to identify the d-spacing. As depicted in Figure 4d, the MoS$_4$-LDH nanospikes show expansion of the lattice fringes to ~1.05 nm, supporting the XRD findings as illustrated in Figure 1a. The selected area electron diffraction (SAED) pattern of MoS$_4$-LDH, captured on a single nanospike, exhibits a spot electron diffraction pattern, illustrating the single crystalline nature of MoS$_4$-LDH (Figure 4e). Figures 4f to 4j represent the high-angle annular dark-field-scanning transmission electron microscopy (HAADF-STEM) image and the energy-dispersive X-ray (EDX) mappings for all the elements. The EDX mappings depict the uniform distribution of molybdenum and sulfur along with Ni and Co all over the MoS$_4$-LDH nanospikes, suggesting the successful anion-exchange process.
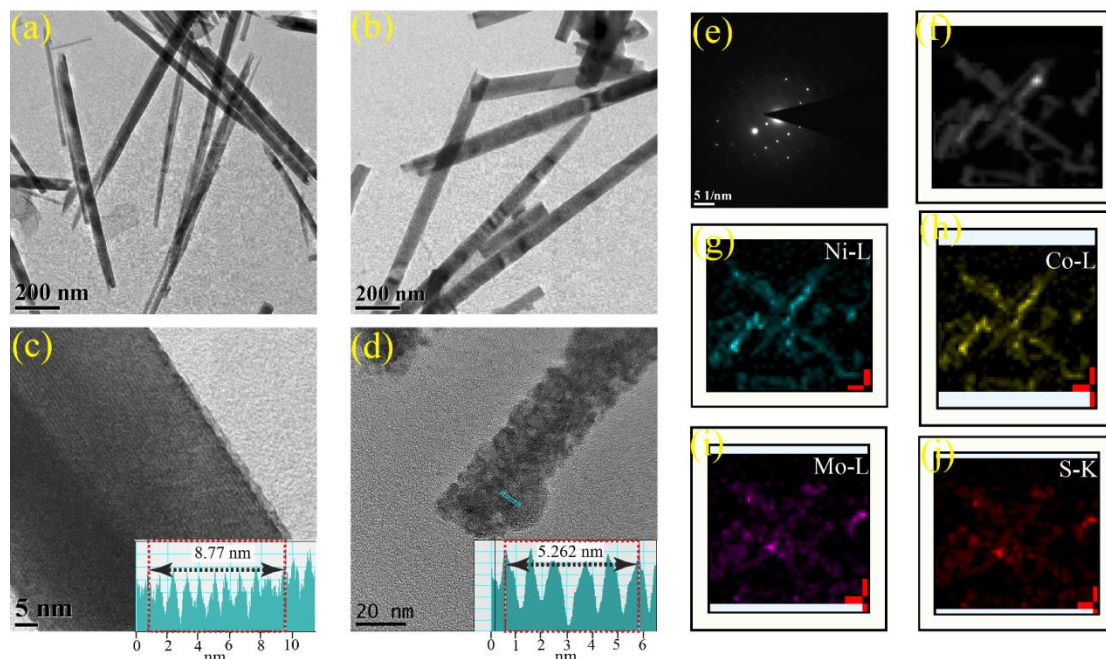
Figure 4. TEM images: (a) NO_3-LDH and (b) MoS_4-LDH nanospikes, (c) higher magnification TEM image of NO_3-LDH nanospike representing the lattice fringes where the inset shows the d-spacing profile, (d) HRTEM image of MoS_4-LDH nanospike showing the lattice fringes and the inset shows the d-spacing profile, image (e) represents the SAED pattern on a single MoS_4-LDH nanospike, panels (f) to (j) represent the HAADF-STEM image and the energy-dispersive X-ray (EDX) mappings corresponding to the different elements.

4.3.1.5. X-ray photoelectron spectroscopy analysis

To further identify the interlayer composition of all the synthesized samples as well as to support the FTIR and XRD findings for the incorporated anions, X-ray photoelectron spectroscopy (XPS) analysis was performed. First of all, adventitious carbon signals of all the controlled samples were comparatively analyzed. Figure 5a illustrates that as compared to CO_3-LDH, there is no additional higher binding energy carbonate (292.3 eV) signal[40] both in the case of NO_3-LDH and MoS_4-LDH. This indicates the success of our anion intercalation process which is further elaborated by analyzing the XPS spectra in the N 1s region (Figure 5b). The N 1s spectrum of NO_3-LDH clearly identifies the characteristic NO_3^- peak centered at 408.20 eV as the interlayer species[28] (Figure 5b). In contrast, the deconvoluted N 1s core level of MoS_4-LDH shows a broad peak, resulting from the merging of the Mo $3p_{3/2}$ peak and the N 1s signal of NH_4^+ centered at 395.52 eV and 399.21 eV, respectively, along with a small peak at 404.25 eV attributable to the remnant nitrite[9] (Figure 5b).
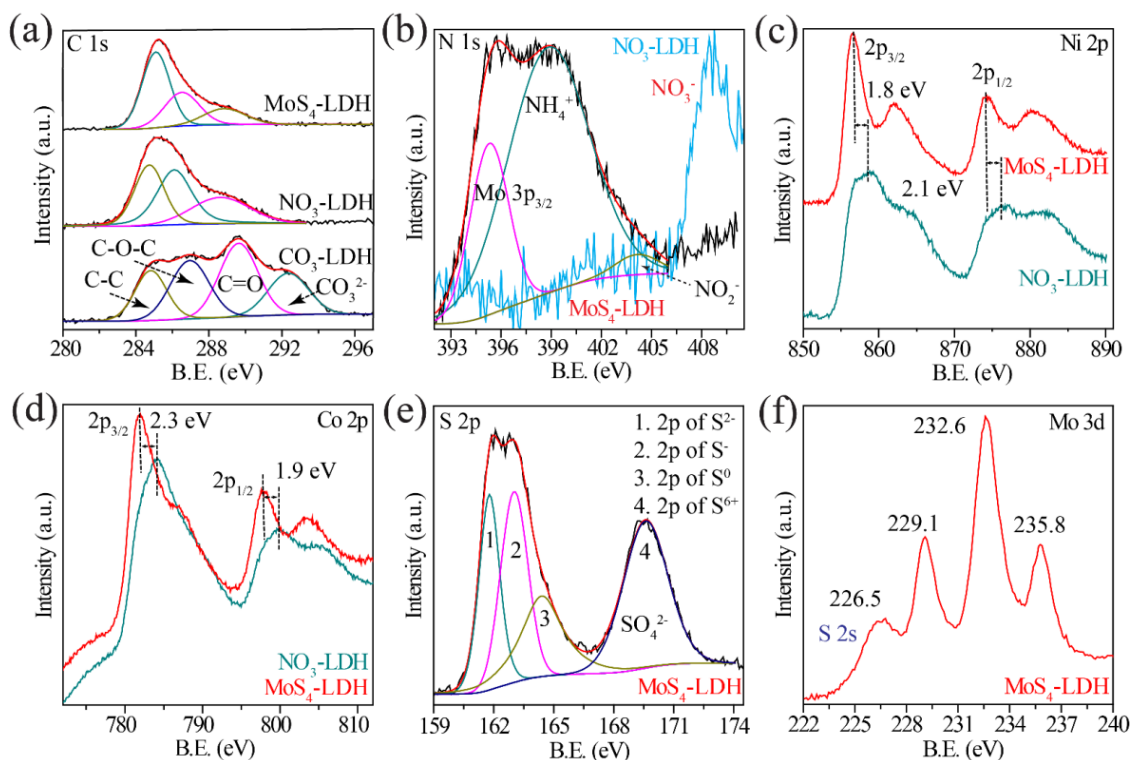
Figure 5. XPS analysis: (a) comparative XPS analysis in the C 1s core level region, (b) the N 1s core level spectra of NO_3-LDH and MoS_4-LDH, (c) and (d) are the comparative Ni 2p and Co 2p spectra, respectively, (e) and (f) are the S 2p and Mo 3d core level spectra of MoS_4-LDH, respectively.

Recently, the effect of intercalated anions on the water oxidation activity was investigated by Zhou *et al.*[27] and Hunter *et al.*[28] *via* detailed electrochemical and XPS characterizations combined with DFT calculations. In these studies, they emphasized that the interlayer anions play key roles toward tuning the electrocatalytic performances of LDHs. In addition, Zeng *et al*. studied the role of interlayer anion toward improving the urea oxidation reaction kinetics.[41] In line with this, we employed a detailed XPS analysis to probe the change in the electronic structure and coordination environment of the metal ions of the LDH with the $[MoS_4]^{2-}$ introduction as well as its role toward the tuning of the electrochemical performance. Figure 5c and 5d provide the comparative Ni 2p and Co 2p spectra of NO_3-LDH and MoS_4-LDH, respectively (powdered sample is examined to avoid any electronic contribution from NF). The lower Ni 2p binding energy shift, as well as, the sharpness of the two spin-orbit doublets after the anion exchange can be concluded as the partial charge transfer from the intercalated $[MoS_4]^{2-}$, leading

to a lower Ni valence state throughout the catalyst. The Co sites show similar trend to the Ni ones, further supporting our claim of electronic structure modification *via* the $[MoS_4]^{2-}$ anions intercalation. In addition, the XPS analysis of MoS_4-LDH in the S 2p region depicts broader peak in the 161–165 eV range, along with the SO_4^{2-} peak (169.60 eV) arising from the moisture sensitivity of the $[MoS_4]^{2-}$ moieties (Figure 5e).[42,37] The broader peak when deconvoluted shows that, along with S^{2-} of $[MoS_4]^{2-}$ anions, partial oxidation at S^{2-} centers to S^- and S^0 is encoutntered.[42,43,44] Such kind of oxidation can be attributed to the extension of sulfur coordination environment toward the metal hydroxide layer, further supporting our claim of partial charge transfer. To analyze the stability of $[MoS_4]^{2-}$ moieties in the LDH gallery, XPS analysis was examined in the Mo 3d region as well. Figure 5f depicts a doublet at 232.58 eV (Mo $3d_{3/2}$) and 229.07 eV (Mo $3d_{5/2}$), originating from the spin-orbit coupling of the Mo^{6+} 3d orbital.[37] Another peak at 235.77 eV corresponds to the octahedral configuration of Mo^{6+} ions.[45] In addition, the weak peak at 226.53 eV is suggestive to be the signature of the S 2s energy of $[MoS_4]^{2-}$ moieties.[37] Hence, the XPS study in the Mo 3d core region demonstrates a typical $[MoS_4]^{2-}$ anion feature, suggesting the protective role of LDH toward moisture-sensitive $[MoS_4]^{2-}$ moieties. A slight shift in binding energy is consistent with the mutual interactions between the metal hydroxide layers and the $[MoS_4]^{2-}$ moieties. Thus, these XPS data support the intercalation as well as stability of $[MoS_4]^{2-}$ anions in the NiCo-LDH interslab space along with their electronic coupling with the metal hydroxide layers probably *via* $M(HO)_2$–S–Mo linkage (M = Ni, Co).

4.3.2. Electrochemical analysis

Hence, the as-proven electronic coupling induces stabilization of the metal hydroxide sites to a lower valence-state. Such kind of hydroxide sites have shown significant contribution to improve the HER kinetics by facilitating the rate-determining water dissociation step as justified by Liang *et al.*[46] In addition, such kind of synergy is also proven to stabilize the high-valence M states when charged,[27] *i.e.,* to MOOH (M = Ni, Co), active sites of water/urea oxidation reaction (WOR/UOR). To support the XPS findings of electronic structure modification and its effect on the electrochemical performance, cyclic voltammetry analysis was performed in the redox region. Figure 6 represents the comparative cyclic voltammogram (CV) of NO_3-LDH/NF and MoS_4-LDH/NF in the redox potential region. The comparative CVs exhibit a negative cathodic redox peak potential shift after $[MoS_4]^{2-}$ anion exchange,

suggesting the role of the intercalated anions toward facilitating the active oxyhydroxide species formation. In addition, the increased area under the cathodic curve is directly associated with the increased interlayer space. It, subsequently, facilitates excess electrolyte infiltrations and hence involvement of more number of active M sites. Altogether, the detailed XPS and CV analyses rationalize that the designed catalyst offers a valuable strategy to efficiently catalyzing the electrochemical reactions involved in the energy-efficient hydrogen generation. To test its proficiency, the designed catalyst is first examined toward the half-cell reactions, *i.e.,* urea oxidation reaction (UOR), water oxidation reaction (WOR), and hydrogen evolution reaction (HER). Afterward, the whole-cell water, urea and urine electrolysis was performed by fabricating the two-electrode device, as described in the upcoming sections.
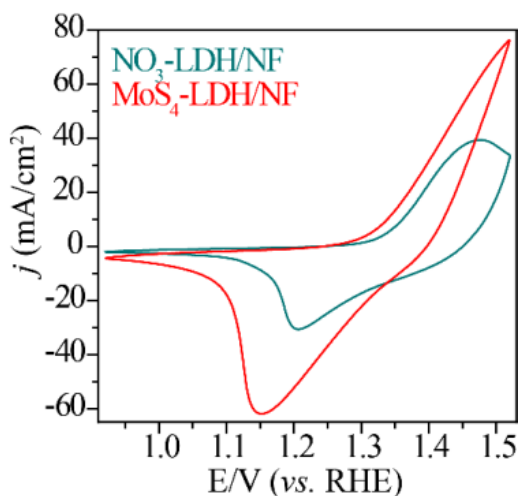

Figure 6. Comparative cyclic voltammograms in N_2 saturated 1 M KOH.

4.3.2.1. Electrocatalytic performance towards UOR and WOR

We first evaluated the electrocatalytic urea oxidation (UOR) and water oxidation (WOR) reaction performance in 1 M KOH with and without 0.33 M urea, respectively. Figure 7a represents the comparative UOR (solid line curves) and WOR (dashed line curves) linear sweep voltammograms (LSV) for NO_3-LDH/NF and MoS_4-LDH/NF. The comparative WOR polarization curves show that the anion exchange process induced negative anodic redox ($Ni(OH)_2 \rightarrow NiOOH$) peak shift from 1.45 V to 1.42 V *vs.* RHE, hence, facilitating the $Ni(OH)_2 \rightarrow NiOOH$ transition, leading to improved WOR performance. Of note, the $Ni(OH)_2 \rightarrow NiOOH$ oxidation onset potential and the UOR onset potential

overlap (inset of Figure 7a). This observation emphasizes that UOR onset and the Ni^{2+} to Ni^{3+} redox transition onset shares the same potential. This gives a strong evidence of the Ni^{3+} to be the active centers for urea oxidation. After the anion exchange, UOR is found to improve by 20 mV and requires only 1.34 V *vs.* RHE to reach the benchmark 10 mA cm^{-2}. The activity tuning of $[MoS_4]^{2-}$ intercalation is found to be more pronounced at higher current densities. Therefore, MoS_4-LDH/NF requires only 1.37 V and 1.40 V *vs.* RHE to reach 40 and 80 mA cm^{-2}, respectively, as compared to 1.40 V and 1.44 V *vs.* RHE required for NO_3-LDH/NF to reach the same current density (Figure 7b). It is important to note that, NO_3-LDH/NF itself showed comparative performance to the best yet reported literatures on UOR.[19,21,22, 47] And, our unique anion-exchange strategy further surpasses the UOR performance of most of the noble and non-noble metal-based catalysts. For comparison, UOR is also catalyzed using bare NF, and commercial 20% RuO_2/C-NF (1.0 mg cm^{-2}). The commercial catalyst shows far inferior activity, displaying 100 mV positive potential shift (1.458 V) from MoS_4-LDH/NF to reach 30 mA cm^{-2} (Figure 7b).
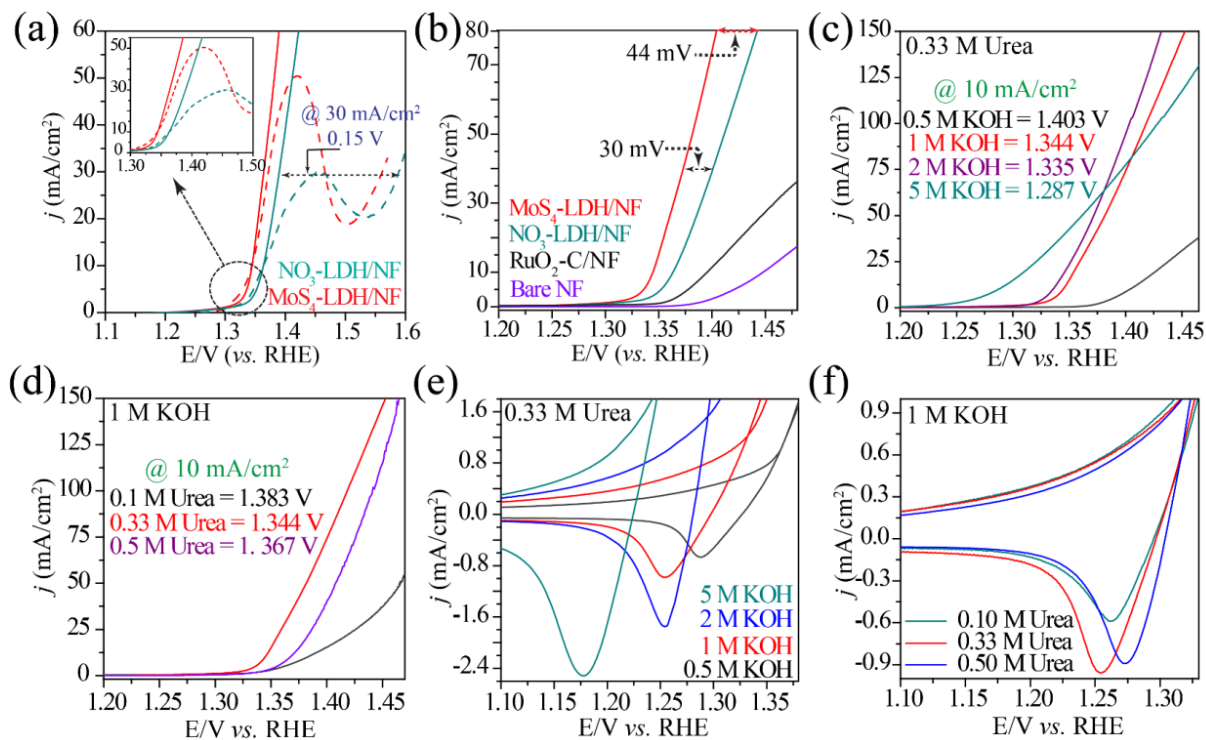
Figure 7. Comparative electrochemical data: (a) UOR (solid lines) and WOR (dashed lines) polarization curves where the inset shows the polarization curve in the onset potential region, (b) polarization curves with controlled samples in 1 M KOH/0.33 M urea, (c) UOR LSV curves with varied

KOH concentration, (d) UOR LSV curves with varied urea concentration, (e) CV curves in the cathodic redox region with varied KOH concentration, (f) CV curves in the cathodic redox region with varied urea concentration.

We next turned to interrogate the outstanding urea oxidizing property of MoS_4-LDH/NF by varying the KOH concentration from 0.5 M to 5 M KOH with a constant urea concentration of 0.33 M. Figure 7c represents the comparative UOR LSV plots with varied KOH concentration, illustrating the direct dependence of UOR on the OH^- concentration. In fact, with 5 M KOH, our catalyst shows surprisingly enhanced performance and required only 1.29 V *vs.* RHE to generate benchmark 10 mA cm^{-2}. The UOR boosting characteristics of MoS_4-LDH/NF was also analyzed by varying the urea concentration from 0.1 M to 0.5 M while keeping the KOH concentration constant (1 M KOH). Figure 7d represents that there is a sufficient performance improvement from 0.10 M to 0.33 M urea concentration. However, going from 0.33 M to 0.50 M urea, our catalyst exhibits unexpected behavior, depicting decreased UOR performance. To find out the underlying reasons that govern the observed anomalous behavior of our catalyst with varied urea concentration, CVs are analyzed comparatively. Figure 7e consists of the cathodic peak portion of the CV curves in varied KOH concentration having a constant urea concentration of 0.33 M. The comparative CV curves reveal that the cathodic redox peak potential and the current are KOH concentration dependent. As the concentration of OH^- ions increases, cathodic redox peak potential shifts negatively, illustrating the facilitated redox transition and hence improved urea oxidation. However, in case of increasing the urea concentration with constant 1 M KOH, the oxyhydroxide formation is limited by the OH^- concentration, restricting the complete oxidation of excess urea. Owing to the partial oxidation, the excess urea, as proposed by Daramola *et al.*[48] and Guo *et al.*[16], may generate plenty of catalyst poisoning adsorbed cyanate and carbonate intermediates. This is the reason, why the UOR performance decreased when the urea concentration is increased from 0.33 M to 0.5 M in 1 M KOH (Figure 7d). This anomalous behavior is also supported by comparative CV study, showing positive cathodic peak potential shift along with the decreased area under the curve as the urea concentration increased from 0.33 M to 0.5 M (Figure 7f). In this way, the comparative CV analyses corroborate 0.33 M urea as the ultimate concentration to achieve the maximum UOR performance.

Next to the activity, mechanistic insights into the catalytic process were accessed through the Tafel analysis from the polarization curves. Comparative Tafel analyses of UOR process revealed remarkably

faster reaction kinetics on MoS_4-LDH/NF and NO_3-LDH/NF as compared to the commercial catalyst (Figure 8a). One important reason of this finding is the *in situ* growth of the active material over the conductive NF substrate. This is in comparison to the *ex situ* coated 20% RuO_2/C over NF, experiencing increased potential drop. Interestingly, MoS_4-LDH/NF shows a Tafel slope value of only 29 mV dec^{-1} rise in current, which is substantially lower than the reported ones, further illustrating the importance of the electronic property tuning strategy *via* $[MoS_4]^{2-}$ anion exchange.[49,21] Next fundamental performance evaluation step for practical application is the long-term catalyzing stability of a material. Figure 8b represents the comparative chronopotentiometric stability test for UOR and OER at 10 mA cm^{-2}. In both the cases, our catalyst exhibited outstanding stability even after 24 h of the continuous catalysis.

4.3.2.2. Electrocatalytic performance towards HER

To overall improve the energy efficiency of the hydrogen generation process, it is also essential to boost up the other water reduction half-cell reaction of the electrolyzer, *i.e.,* HER, by employing a suitable
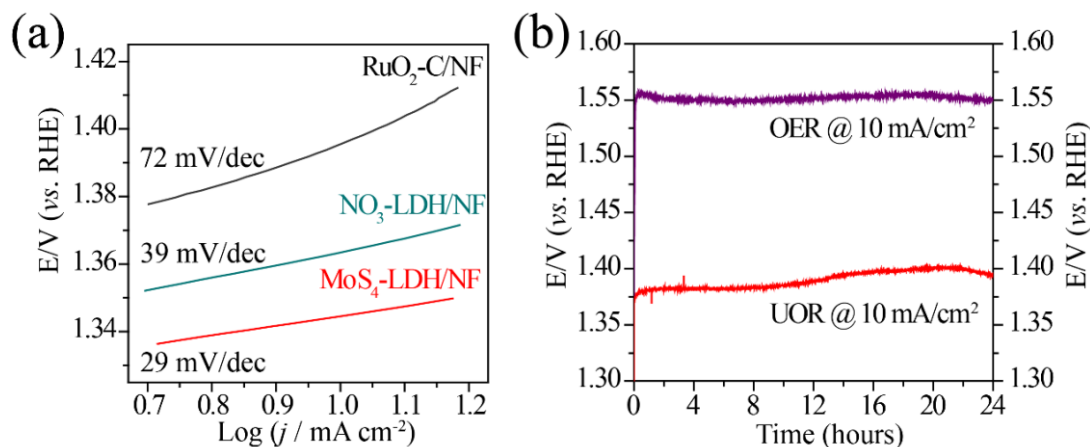
Figure 8. Comparative electrochemical data: (a) UOR Tafel plots, (b) UOR and OER chronopotentiometric stability test of MoS_4-LDH/NF.

catalyst. Here, the meaning of a suitable catalyst is not only limited to populate active centers but also to protect the active centers as well as to save the H^+ reducing electrons from the parallel competing oxygen reduction reaction. Intriguingly, our final catalyst, *i.e.,* MoS_4-LDH/NF, is designed in such a way that it contains the HER-selective $[MoS_4]^{2-}$ anions to improve the energy-efficiency of the H_2 generation process even in urine as well as other toxic environment.[9] Figure 9a represents the

comparative HER LSV curves of our designed materials with commercial 20% Pt-C/NF (1.0 mg cm^{-2}) in 1 M KOH. The comparative plots reveal that, MoS$_4$-LDH/NF and NO$_3$-LDH/NF exhibit a mere 91 mV and 140 mV negative potential shifts, respectively, *w.r.t.* 20% Pt-C/NF to reach the benchmark 10 mA cm^{-2}. This potential gap further reduces at higher current densities (*i.e.,* above 20 mA cm^{-2}), illustrating the electronic structure tuning of the designed catalyst.
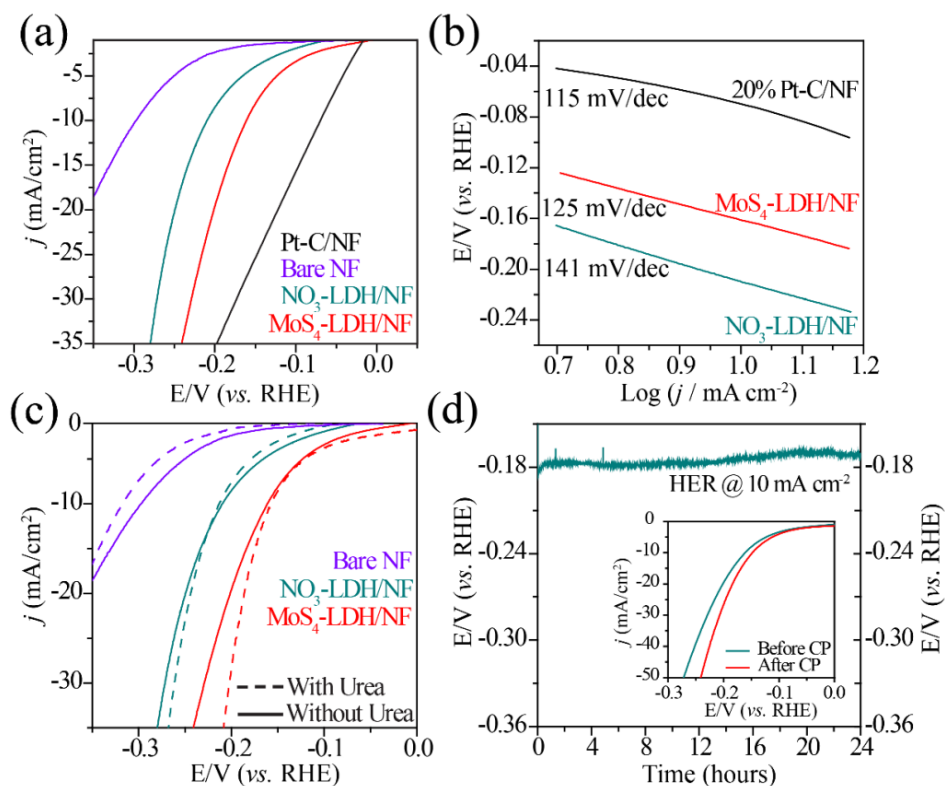
Figure 9. Comparative: (a) HER polarization curves, (b) HER Tafel plots, and (c) HER polarization curves in presence and absence of 0.33 M urea. (d) HER chronopotentiometric stability test of MoS$_4$-LDH/NF where the inset shows the LSV curves before and after the stability test.

The electronic structure tuning was further examined by employing Tafel analysis. And, MoS$_4$-LDH/NF shows a Tafel slope value of 125 mV dec^{-1} as compared to 115 mV dec^{-1} for 20% Pt/C (Figure 9b). Of note, a slope value of >120 mV dec^{-1} is generally associated with a ligand-based mechanism rather than metal hydride-based mechanism to catalyze HER.[9,50,51] And, the importance of a ligand-based mechanism is to make the catalyst effective both in oxic environment as well as in presence of foreign species, *e.g.,* urea. The reason why MoS$_4$-LDH/NF follows a ligand-based mechanism is the strong H$^+$ accepting power of [MoS$_4$]$^{2-}$ *via* thio groups, providing reasonable activity as well as stability even in

the presence of catalyst poisons. In support of this claim, HER is performed with 0.33 M urea/1 M KOH. As shown in Figure 9c, MoS_4-LDH/NF does not show any negative impact of urea on HER, further guaranteeing its attracting H_2 generating property in the urea electrolyzer. Next, to support catalyst robustness, long-term catalytic stability of MoS_4-LDH/NF was performed through time-dependent potential curve, depicting a steady-state performance even after 24 h continuous catalysis (Figure 9d).
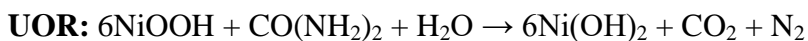
4.3.2.3. Possible reaction mechanism on MoS_4-LDH/NF

Now, based on all the above-mentioned half-cell electrochemical studies as well as in accordance with the reported reaction pathways, a plausible reaction mechanism is proposed. As we know, among the two-half cell reactions, the cathodic HER is found to follow the ligand-based mechanism. It starts *via* the reduction of $[MoS_4]^{2-}$ anions in aqueous environment to $[MoS_3SH]^{2-}$, owing to the strong H^+ accepting tendency of its thio groups.[9] It is then followed by the stabilization of the other water dissociation product, *i.e.,* OH^- over OH-acceptor $Ni(OH)_2$.[32] Subsequently, by evolving H_2, the $[MoS_3SH]^{2-}$ regenerates $[MoS_4]^{2-}$ and $Ni(OH)_2$ gets oxidized to NiOOH.[15] The NiOOH moieties, by catalyzing the other half-cell, *i.e.,* WOR/UOR, undergo cathodic reduction back to $Ni(OH)_2$.[15] This is the possible pathway through which all the H_2-electrolyzer reactions get boosted up synergistically *via* the catalytically-tuned MoS_4-LDH/NF. The as-hypothesized catalytic mechanism as well as catalyst regeneration is illustrated as follows:

Cathodic Reaction:

Volmer step: $[MoS_4]^{2-} + Ni(OH)_2 + H_2O + e^- \rightarrow [MoS_3SH]^{2-} + Ni(OH)_2–OH^-_{ad}$
Heyrovsky Step: $[MoS_3SH]^{2-} + H_2O + e^- \rightarrow [MoS_4]^{2-} + H_2 + OH^-$

Anodic Reaction:

Redox Reaction: $Ni(OH)_2–OH^-_{ad} \rightarrow NiOOH + H_2O + e^-$
**UOR:** $6NiOOH + CO(NH_2)_2 + H_2O \rightarrow 6Ni(OH)_2 + CO_2 + N_2$
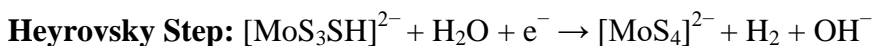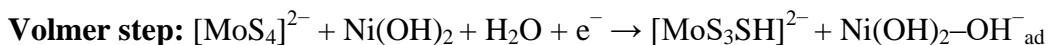
The above-mentioned reaction pathway can also be supported experimentally by examining the post-analyzed samples in Ni 2p region *via* XPS. The Ni 2p core level spectrum of post-HER sample displays

the emergence of an additional higher binding energy peak at 860.59 eV, corresponding to the Ni^{3+} species[6] (Figure 10).This additional peak emergence supports our as-proposed HER mechanism, where the catalyst undergoes $Ni(OH)_2 \rightarrow NiOOH$ transformation. In contrast, the Ni 2p core level of post-UOR sample shows similar binding energy to that of fresh MoS_4-LDH (Figure 5c), suggesting the back $NiOOH \rightarrow Ni(OH)_2$ transition during UOR (Figure 10). In this way, the Ni 2p core level XPS analysis of post-HER and post-UOR samples reveals quite good reversibility and hence robustness of the catalyst system.

4.3.2.4. Whole-cell Alkaline Urea Electrolysis

Taking the above mentioned superiorities into account, here, we have employed MoS_4-LDH/NF both as the cathode and anode to construct a two-electrode electrolyzer. Figure 11a illustrates the importance of urea electrolysis over water electrolysis schematically, which is proven experimentally in our work. Figure 11b represents the comparative LSV curves of whole-cell urea electrolysis tested in 1 M KOH/0.33 M urea. As expected, the MoS_4-LDH/NF-based couple (MoS_4-LDH/NF‖MoS_4-LDH/NF) outperformed the-state-of-art Pt-C/NF‖RuO_2-C/NF electrode pairs with a cell voltage of only 1.37 V as
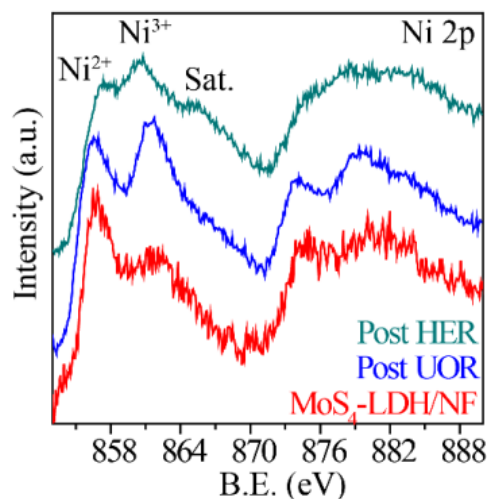
Figure 10. Comparative Ni 2p core level spectra of MoS_4-LDH/NF before and after the UOR and HER stability test.

compared to 1.485 V required for the commercial catalyst pair to deliver benchmark 10 mA cm^{-2}. (NO_3-LDH/NF‖NO_3-LDH/NF) and (bare NF‖bare NF)-based electrode pairs were also tested for urea

electrolysis, requiring 1.52 V and 1.73 V to deliver 10 mA cm^{-2}. These comparative results again suggest the remarkable role of $[MoS_4]^{2-}$ intercalation into NiCo-LDH interslab, leading to superb performance. Interestingly, when we switched from synthetic urea to direct human urine, our catalyst did not show much change in the performance and required 1.44 V cell voltage to deliver 10 mA cm^{-2} (Figure 11c). At higher current densities, our catalyst delivered similar performance to that of synthetic urea, supporting the suitability of our designed strategy for direct urine-based urea utilization toward useful fuel.
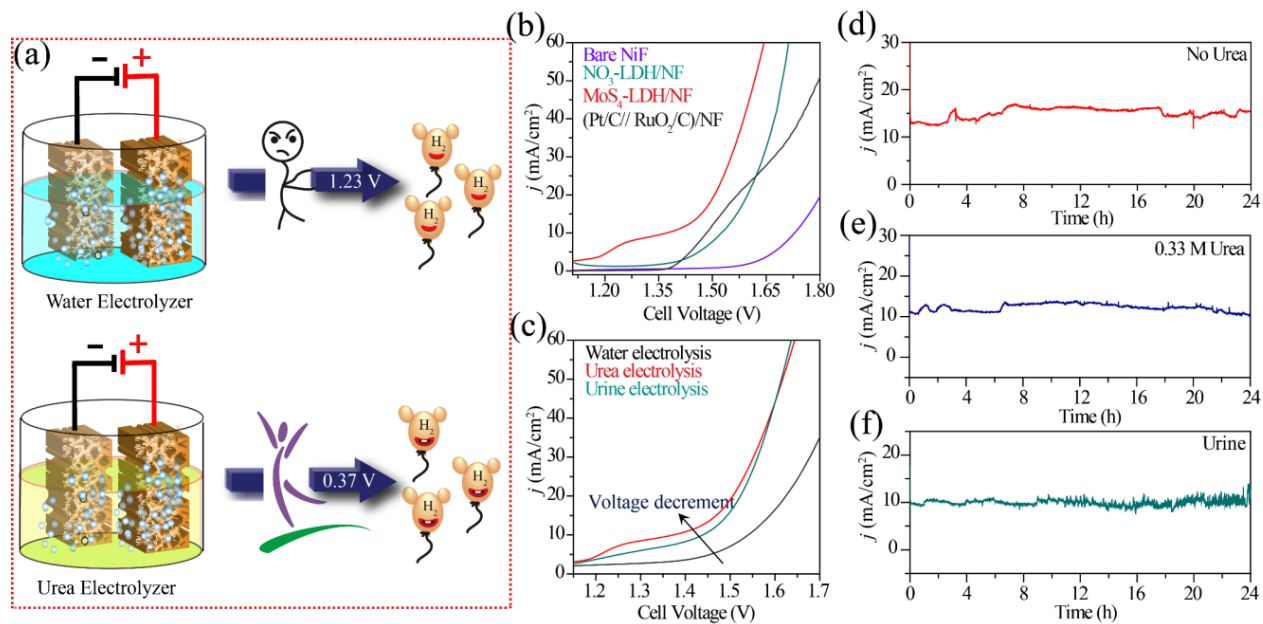
Figure 11. Whole-cell electrolysis: (a) schematic representation of the benefits of urea electrolysis over water electrolysis in alkaline medium, (b) comparative polarization curves of urea electrolysis with various electrodes employed in this study, (c) comparative LSV curves for water, urea and urine electrolysis of MoS$_4$-LDH/NF; chronoamperometric stability test recorded for (d) water electrolysis, (e) urea electrolysis, and (f) urine electrolysis. In all the urea electrolysis cases, 0.33 M urea was added. Urine electrolysis was performed by in 1 M KOH.

The proficiency of the designed catalyst is further proven through the long-term catalyzing capability with and without urea. Figure 11d and 11e represent the chronoamperometric durability test for MoS$_4$-LDH/NF without and with 0.33 M urea. In both the cases, the catalyst maintained current density above 10 mA cm^{-2} even after 24 h of continuous catalytic process with no apparent performance degradation.

To prove the viability of the designed catalyst in sewage water, the long-term catalytic efficiency was analyzed with the direct-urine electrolysis. Figure 11f depicts that while delivering a-steady-state current density of 10 mA cm^{-2} for continuous 24 h of operation, no obvious degradation and catalyst deactivation is encountered from the proteins and other catalyst poisons present. Most importantly, during all the mentioned durability tests, even after the consumption of urea in between the operation, no performance degradation is encountered, offering industrial interest in our catalyst. In this way, our designed catalyst gives a great promise of its implementation for the direct-sewage water utilization towards sustainable hydrogen generation and simultaneous sewage denitrification.

4.4.   Conclusion

To sum up, here, we have successfully grown the $[MoS_4]^{2-}$ anions-intercalated NiCo-LDH on the nickel foam *via* an energy-saving two-step process. XPS and electrochemical analyses revealed the potential role of $[MoS_4]^{2-}$ anion intercalation towards tuning the electronic structure of LDH and hence the electrochemical performance. The electrocatalytic activity of the designed heterostructures is attributed to several superiorities including: (i) the synergistic effect between the intercalated $[MoS_4]^{2-}$ and the positively charged NiCo-hydroxide layers reducing the internal potential drop, (ii) the abundant, uniformly distributed and exposed active sites of LDH, (iii) the plentiful hydrated LDH channels for the reaction species transportation, and (iv) 3D nanospike texture over the nickel foam further facilitating the electrolyte infiltrations and product gas transport. Here, we discovered that the designed catalyst works equally efficiently with the real urine, and delivered the constant performance for more than 24 h with no apparent deactivation. Hence, our designed catalyst illustrates the feasibility of the as-claimed inspiration for the anodic water oxidation substitution as well as waste water management. Lastly, the above-mentioned superiorities of our designed strategy place the obtained catalyst at the top of yet reported works towards its direct industrial implementation.

4.5.   References

1   J. O. Bockris, *Science*, 1972, **176**, 1323.
2   A. E. Cohen and K. F. Kerdahi, *J. AOAC Int.*, 1996, **79**, 858–860.
3   D. M. F. Santos, C. A. C. Sequeira and J. L. Figueiredo, *Quim. Nova*, 2013, **36**, 1176–1193.
4   A. Nadeema, P. S. Walko, R. N. Devi and S. Kurungot, *ACS Appl. Energy Mater.*, 2018, acsaem.8b01081.
5   L. Truong, S.-K. Jerng, S. B. Roy, J. H. Jeon, K. Kim, K. Akbar, Y. Yi and S.-H. Chun, *ACS Sustain. Chem. Eng.*, 2019, **7**, 4625–4630.

6   A. Nadeema, V. M. Dhavale and S. Kurungot, *Nanoscale*, 2017, **9**, 12590–12600.
7   M. Li, P. Zhang, R. Xie, Z. Hu, Z. Lu, L. Chen, L. Song, X. Xu, Y. Wu and X. Zhao, *J. Mater. Sci.*, 2019, **54**, 9034–9048.
8   E. E. Benn, B. Gaskey and J. D. Erlebacher, *J. Am. Chem. Soc.*, 2017, **139**, 3663–3668.
9   S. Chatterjee, K. Sengupta, S. Dey and A. Dey, *Inorg. Chem.*, 2013, **52**, 14168–14177.
10   T. Take, K. Tsurutani and M. Umeda, *J. Power Sources*, 2007, **164**, 9–16.
11   Y. X. Chen, A. Lavacchi, H. A. Miller, M. Bevilacqua, J. Filippi, M. Innocenti, A. Marchionni, W. Oberhauser, L. Wang and F. Vizza, *Nat. Commun.*, 2014, **5**, 4036.
12   J. Y. Zhang, X. Tian, T. He, S. Zaman, M. Miao, Y. Yan, K. Qi, Z. Dong, H. Liu and B. Y. Xia, *J. Mater. Chem. A*, 2018, **6**, 15653–15658.
13   W. Xu, Z. Wu and S. Tao, *Energy Technol.*, 2016, **4**, 1329–1337.
14   B. K. Boggs, R. L. King and G. G. Botte, *Chem. Commun.*, 2009, 4859–4861.
15   L. Chen, X. Dong, Y. Wang and Y. Xia, *Nat. Commun.*, 2016, **7**, 11741.
16   F. Guo, K. Ye, M. Du, X. Huang, K. Cheng, G. Wang and D. Cao, *Electrochim. Acta*, 2016, **210**, 474–482.
17   R. K. Singh and A. Schechter, *Electrochim. Acta*, 2018, **278**, 405–411.
18   G. Wang and Z. Wen, *Nanoscale*, 2018, **10**, 21087.
19   S. Chen, J. Duan, A. Vasileff and S. Z. Qiao, *Angew. Chemie - Int. Ed.*, 2016, **55**, 3804–3808.
20   X. Zhu, X. Dou, J. Dai, X. An, Y. Guo, L. Zhang, S. Tao, J. Zhao, W. Chu, X. C. Zeng, C. Wu and Y. Xie, *Angew. Chemie Int. Ed.*, 2016, **55**, 12465–12469.
21   F. Li, J. Chen, D. Zhang, W. F. Fu, Y. Chen, Z. Wen and X. J. Lv, *Chem. Commun.*, 2018, **54**, 5181–5184.
22   Z. Y. Yu, C. C. Lang, M. R. Gao, Y. Chen, Q. Q. Fu, Y. Duan and S. H. Yu, *Energy Environ. Sci.*, 2018, **11**, 1890–1897.
23   A. Schranck, R. Marks, E. Yates and K. Doudrick, *Environ. Sci. Technol.*, 2018, **52**, 8638–8648.
24   L. Ma, Q. Wang, S. M. Islam, Y. Liu, S. Ma and M. G. Kanatzidis, *J. Am. Chem. Soc.*, 2016, **138**, 2858–2866.
25   D. J. Lockwood, D. S. Hall, C. Bock and B. R. Macdougall, *Proc. R. Soc. London, Ser. A,* 2015, **471**, 20140792.
26   G. Fan, F. Li, D. G. Evans and X. Duan, *Chem. Soc. Rev.*, 2014, **43**, 7040–7066.
27   D. Zhou, Z. Cai, Y. Bi, W. Tian, M. Luo, Q. Zhang, Q. Xie, J. Wang, Y. Li, Y. Kuang, X. Duan, M. Bajdich, S. Siahrostami and X. Sun, *Nano Res.*, 2018, **11**, 1358–1368.
28   B. M. Hunter, W. Hieringer, J. R. Winkler, H. B. Gray and A. M. Müller, *Energy Environ. Sci.*, 2016, **9**, 1734–1743.
29   Y. Jin, S. Huang, X. Yue, H. Du and P. K. Shen, *ACS Catal.*, 2018, **8**, 2359–2363.
30   M. Gao, W. Sheng, Z. Zhuang, Q. Fang, S. Gu, J. Jiang and Y. Yan, *J. Am. Chem. Soc.*, 2014, **136**, 7077–7084.
31   B. J. Trzešniewski, O. Diaz-Morales, D. A. Vermaas, A. Longo, W. Bras, M. T. M. Koper and W. A. Smith, *J. Am. Chem. Soc.*, 2015, **137**, 15112–15121.
32   R. Subbaraman, D. Tripkovic, D. Strmcnik, K. C. Chang, M. Uchimura, A. P. Paulikas, V. Stamenkovic and N. M. Markovic, *Science* 2011, **334**, 1256–1260.
33   L. Trotochaud, S. L. Young, J. K. Ranney and S. W. Boettcher, *J. Am. Chem. Soc.*, 2014, **136**, 6744–6753.
34   M. S. Burke, M. G. Kast, L. Trotochaud, A. M. Smith and S. W. Boettcher, *J. Am. Chem. Soc.*, 2015, **137**, 3638–3648.
35   A. Inayat, M. Klumpp and W. Schwieger, *Appl. Clay Sci.*, 2011, **51**, 452–459.
36   L. Ma, S. M. Islam, C. Xiao, J. Zhao, H. Liu, M. Yuan, G. Sun, H. Li, S. Ma and M. G. Kanatzidis, *J. Am. Chem. Soc.*, 2017, **139**, 12745–12757.
37   L. Ma, S. M. Islam, H. Liu, J. Zhao, G. Sun, H. Li, S. Ma and M. G. Kanatzidis, *Chem. Mater.*, 2017, **29**, 3274–3284.
38   X. Ma, R. Dang, J. Liu, J. Li, Y. Kang, Y. Gong, Z. Zhang and Y. Ma, *Compos. Interfaces*, 2016, **23**, 51–63.
39   L. Dang, H. Liang, J. Zhuo, B. K. Lamb, H. Sheng, Y. Yang and S. Jin, *Chem. Mater.*, 2018, **30**, 4321–4330.
40   D. Puentes-Camacho, E. F Velázquez, D. E Rodríguez-Félix, M. Castillo-Ortega, R. R Sotelo-Mundo and T. del Castillo-Castro *Adv. Nat. Sci Nanosci. Nanotechnol*, 2017, **8**, 045011−045018.
41   M. Zeng, J. Wu, Z. Li, H. Wu, J. Wang, H. Wang, L. He and X. Yang, *ACS Sustain. Chem. Eng.*, 2019, **7**, 4777–4783.
42   Z. Chen, A. Jawad, Z. Liao, Z. Zhou, A. Khan, T. Wang, J. Ifthikar, A. Shahzad and Z. Chen, *ACS Appl. Mater. Interfaces*, 2017, **9**, 28451–28463.
43   L. Hang, T. Zhang, Y. Sun, D. Men, X. Lyu, Q. Zhang, W. Cai and Y. Li, *J. Mater. Chem. A*, 2018, **6**, 19555–19562.
44   J. Wang, Z. Li, N. Hu, L. Liu, C. Huang, Q. Yang, Y. Wang, Y. Suo, T. Wang and J. Wang, *J. Mater. Chem. A*, 2017, **5**, 22506–22511.
45   W. Wang, L. Yang, F. Qu, Z. Liu, G. Du, A. M. Asiri, Y. Yao, L. Chen and X. Sun, *J. Mater. Chem. A*, 2017, **5**, 16585–16589.
46   Z. Liang, H. S. Ahn and A. J. Bard, *J. Am. Chem. Soc.*, 2017, **139**, 4854–4858.
47   C. Xiao, S. Li, X. Zhang and D. R. MacFarlane, *J. Mater. Chem. A*, 2017, **5**, 7825–7832.
48   D. A. Daramola, D. Singh and G. G. Botte, *J. Phys. Chem. A*, 2010, **114**, 11513–11521.
49   D. Liu, T. Liu, L. Zhang, F. Qu, G. Du, A. M. Asiri and X. Sun, *J. Mater. Chem. A*, 2017, **5**, 3208–3213.
50   A. B. Laursen, S. Kegnæs, S. Dahl and I. Chorkendorff, *Energy Environ. Sci.*, 2012, **5**, 5577.
51   J. Bonde, P. G. Moses, T. F. Jaramillo, J. K. Nørskov and I. Chorkendorff, *Faraday Discuss.*, 2009, **140**, 219–231.
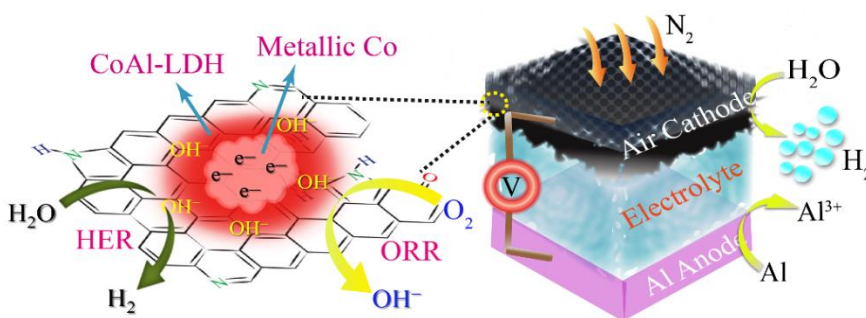
Chapter 5

Co@CoAl-LDH/NG Composite-Catalyzed Dual-Mode Al-Based Battery for Simultaneous H₂ Production and Electricity Generation*

In this chapter we propose the fabrication and demonstration of a dual-mode Al-based battery to generate H_2 and electricity simultaneously. However, to improve the overall energy-efficiency of the device, development of a robust bifunctional catalyst is required, which can catalyze both O_2 Reduction Reaction (ORR) as well as H_2O reduction (Hydrogen Evolution Reaction, HER). Taking this into account, here we tuned the physicochemical property of LDH and synthesized a bifunctional Co@CoAl-LDH/NGr electrocatalyst to catalyze both the ORR and HER. The designed catalyst was thoroughly characterized by employing various material characterization techniques, *e.g.,* X-ray diffraction analysis, high-resolution transmission electron microscopy, X-ray photoelectron spectroscopy, *etc.* The homemade catalyst when employed as the cathode both in the presence and absence of O_2, it worked quite efficiently and performed comparable to the commercial Pt-based catalyst. In dual-mode Al-based battery, at a discharge current density of 5 mA cm^{-2}, the catalyst-coated cathode exhibited an average voltage of ~0.95 V both in the presence and absence of O_2. The H_2 generated was quantified with gas chromatography.

*The content of this chapter is under publication.

5.1. Introduction

Ever depleting fossil fuel reservoirs and their adverse environmental impact have compelled the scientific society to look for the alternate energy options.[1,2] Following this, numerous renewable energy sources have been discovered as well as harvesters have been built to harvest any possible form of natural energy, for instance, wind, solar, and geothermal energy.[3,4] However, most of these alternate energy sources suffer from their intermittency and localized nature.[5] In this context, electrochemistry bestows us various promising ways of storing as well as transporting this irregular and localized form of energy, for example, in the electrochemical form of batteries, supercapacitors, and hydrogen.[4,6] Among which, renewable energy storage in the chemical form of H_2 *via* water splitting is found to be more appealing since the H_2 produced can be directly utilized in fuel cells for fulfilling further energy requirements in sustainable as well as eco-friendly manner.[1,7] Nevertheless, the high energy-intensive process of the electrochemical water splitting hinders its industrial implementation.[8] Hence, it is highly demanding to develop feasible and energy-saving water electrolyzers to utilize the intermittent renewable energy precisely as well as to reduce the H_2 generation capital cost.[9]

In this regard, tremendous efforts have been devoted for designing robust catalysts to boost-up the two half-cell reactions of water electrolyzer, *i.e.,* cathodic hydrogen evolution reaction (HER) and anodic water oxidation reaction (WOR).[10,11,12] Among which, owing to the sluggish four proton-coupled four-electron transfer process, WOR is found to be the overall energy efficiency deciding factor of the water electrolyzer.[13,14] That is why, replacing the energy-uphill water oxidation with readily oxidizable species, *e.g.,* alcohols[15], hydrazine[16], urea[17], have been proposed as an alternative strategy to facilitate the overall H_2 generation process. Very recently, our group has also contributed to generate low-cost H_2 by substituting the fresh water-based WOR with urine-sourced urea, directly.[18] Apart from this, several organic reactions are demonstrated to couple with HER for generating H_2 and value-added product simultaneously by directly harvesting the energy conversions involved.[19,20] Nevertheless, these approaches still need extra energy to drive H_2 generation from water. Considering this, in recent past, Yonggang group have proposed a very new-concept of Li-H_2O fuel cell for replacing WOR with electropositive metal, *i.e.,* Li, to not only contribute in reducing the energy requirement of H_2 production but also for the simultaneous electricity generation.[21,22] However, the proposed

concept suffered from the high cost of the separator, Li metal scarcity, as well as the use of organic electrolyte, which can further question the price and safety of the as-generated H_2. Following this, Cai *et al.* introduced a little modification by replacing Li with Zn for overcoming any negative impact of Li.[23] However, for reaching similar performance, neutralization energy harvesting concept was also introduced along with Zn oxidation. Despite a better approach, this work also suffers from the high-cost of the bipolar membrane as well as the corrosive nature of highly concentrated acid and alkaline electrolytes.

In this context, as a contribution in the direction of minimizing all the above-described limitations of energy-efficient H_2 generation; here we are extending the newly-developed approach by introducing the concept of Al-H_2O fuel cell. The motivation of the work was built from a novel method of hydrogen production *via* a self-sustained reaction between activated aluminum powder and water; as-proposed by Prof. Alon Gany and coworkers.[24] Here, they mentioned about the "energy bonus" of 17 kJ per gram of Al during the exothermic (Al + 3H_2O → Al(OH)$_3$ + 3/2 H_2) reaction. Thus, this energy bonus can be harvested simply by separating the involved reaction through electrochemistry into two half-cell reactions. The other superiorities of the as-proposed approach include: (1) its nearly uniform abundance throughout the world, (2) low cost, (3) high specific capacity, (4) suitability with aqueous electrolyte, (5) higher theoretical voltage of 1.48 V in Al-H_2O battery mode with 0.1 M KOH, (6) works efficiently even with a very low alkali concentration to avoid any safety issues. Thus, we believe that the proposed concept of Al-H_2O battery can overcome the till-date faced difficulties for implementing this newly-developed concept of simultaneous H_2 and electricity generation. Apart from this, the as-proposed concept can also take advantage of H_2 liberating during self-discharge, which otherwise is a big challenge to tackle for Al-air battery commercialization.

Scheme 1 illustrates the sketch of a dual-mode Al-based battery wherein the presence of O_2, the device works as an Al-air battery generating electricity (Scheme 1A) and in the absence of O_2, as an Al-H_2O fuel cell generating both H_2 and electricity (Scheme 1B). Here, the logic of demonstrating a dual-mode battery is to validate our as-proposed concept of Al-H_2O fuel cell. The battery schematic consists of three components, Al foil anode, bifunctional catalyst-coated cathode, and 0.1 M KOH as the electrolyte. Among which, designing of a low-cost robust bifun-
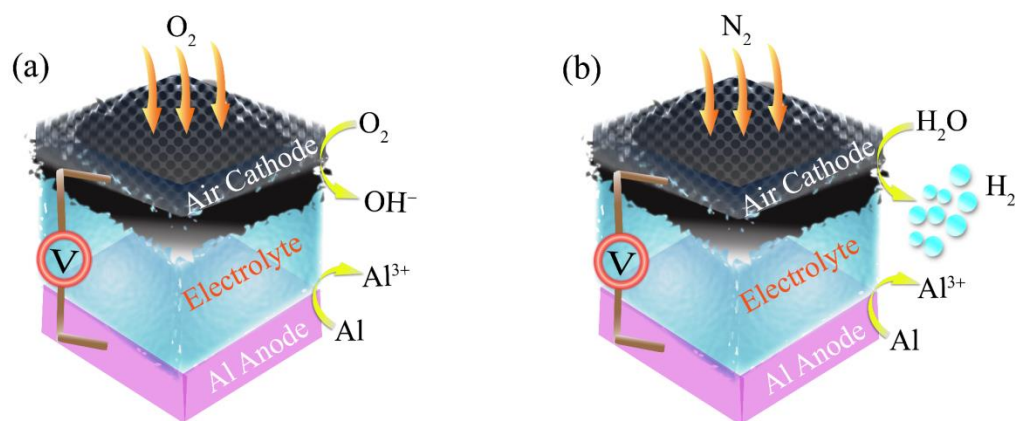
Scheme 1. Al-Based dual-mode battery illustrations: (A) in Al-O$_2$ mode, (B) in Al-H$_2$O mode.

-ctional catalyst is an important parameter to improve the overall energy-efficiency of the as-proposed pathway of H$_2$ generation. Here, the catalytic bifunctionality term stands for catalyzing oxygen reduction reaction (ORR) and hydrogen evolution reaction (HER) simultaneously. Noticeably, HER is our key focus, which in alkaline medium is controlled by the highly energy-intensive water dissociation step (Volmer step).[25] Hence, to facilitate the Volmer step, an optimal HER catalyst requires a synergistic involvement of the reactive H-stabilizing electron-rich metallic sites and hydroxyl-stabilizing hydroxide moieties.[26] Thus, we believe that the designed Co@CoAl-LDH nanostructures, having metallic Co-rich core and LDH-enriched shell, engraved in N-doped graphene (NG) can act as a robust HER electrocatalyst. Besides, the fine architectural designing of the electronically-rich metallic core and Al-enriched hydroxide shell can also bestow us good ORR activity. In line with the above discussion, here, our goals include the designing of a robust bifunctional catalyst, understanding the structure-property correlation, and validating the as-claimed superiorities of designed catalyst on device-level demonstrations *via* dual-mode Al-based battery analysis.

5.2. Experimental Section

5.2.1. Graphene oxide (GO) synthesis: All the chemical reagents were purchased and directly used without any further purification. GO was prepared by employing improved Hummer's method[27] from the commercially available graphite flakes by applying a harsh oxidizing treatment.
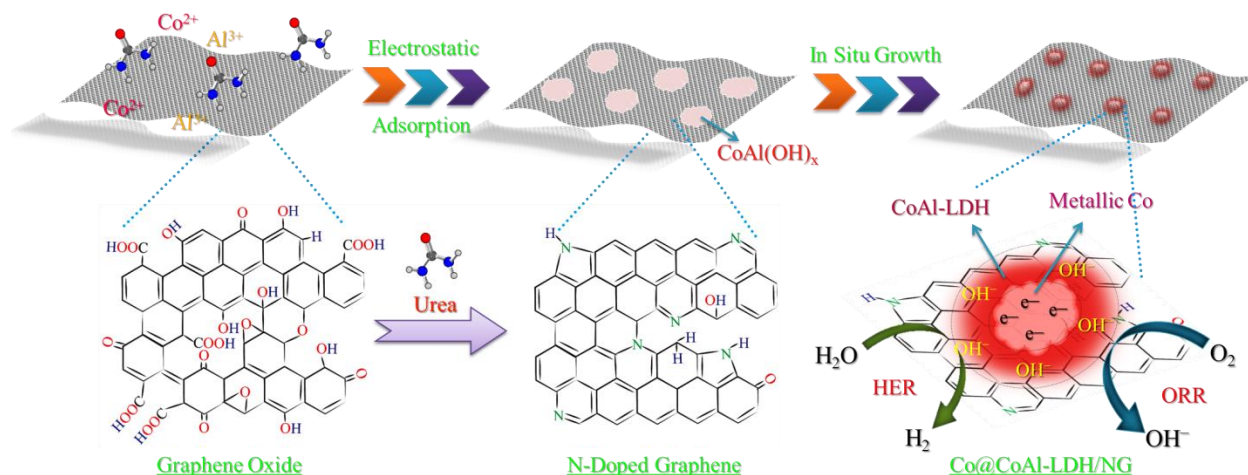
Scheme 2. Illustrations of the steps involved during the one-pot synthesis of Co@CoAl-LDH/NG.

5.2.2. Synthesis of N-doped graphene (NG): Here, NG was synthesized *via* a single-step low-temperature hydrothermal treatment. The procedure first involved the proper dispersion of the as-prepared GO in deionized water with 1 mg cm^{-2} concentration. This was achieved *via* overnight stirring followed by 2–3 h water-bath sonication. Afterwards, urea was added in adequate amount to the GO-water solution which was then poured in Teflon-lined autoclave by leaving ~20% empty space. Next, the stainless steel packed autoclave was kept in oven and heated to 180 $^{\circ}$C within a time period of one hour. The reaction temperature at 180 $^{\circ}$C was continued for next 12 h. Later on, the autoclave was allowed to cool down naturally. It was then followed by the sample washing with plenty of distilled water *via* filtration. Finally, the sample was kept for drying at 60 $^{\circ}$C for 8 h.

5.2.3. Synthesis of Co@CoAl/NG: The synthesis of evenly distributed Co@CoAl-layered double hydroxide core-shell structures over *in situ* generated N-doped graphene was realized in a one-pot and eco-friendly approach. The synthesis procedure followed the same steps as it was adopted for the NG synthesis. The only difference was the addition of metal salts along with urea. Here, the two metal salts, *i.e.,* Co(NO$_3$)$_2$·6H$_2$O and Al(NO$_3$)$_3$·9H$_2$O were added in 3:1 ratio. Amount of urea added was kept in 1:5 ratio to total metal salts. The composite was synthesized with a calculated metal loading of 30% *w.r.t.* graphene oxide.

5.2.4. Synthesis of Co(OH)$_x$/NG: Anchoring of cobalt hydroxides over NG was achieved by adding only cobalt salt and urea in 1:5 ratio without adding any Al salt. Other than this the synthesis procedure employed was same as it was for NG synthesis.

5.2.5. Synthesis of AlOOH/NG: AlOOH moieties growth over NG was achieved by following the same procedure as it was performed for Co(OH)$_x$/NG just by replacing Co salt with Al salt.

5.3. Results and discussion

5.3.1. Structure and Morphology of the Catalyst

This section deals with the synthesis and thorough material characterizations of the as-synthesized materials. All the employed samples are synthesized by adopting a single-step hydrothermal process at 180 ^{o}C for 12 h. As shown in Scheme 2, the anchoring of Co@CoAl-LDH core-shell nanostructures over N-doped graphene (abbreviated as Co@CoAl/NG) is primarily driven by the electrostatic interactions between the oxygen-containing functional groups of graphene oxide, urea and metal ions under the hydrothermal conditions. Interestingly, the as-employed urea as a precipitating agent also acted as N-dopant during the hydrothermal reduction of graphene oxide.
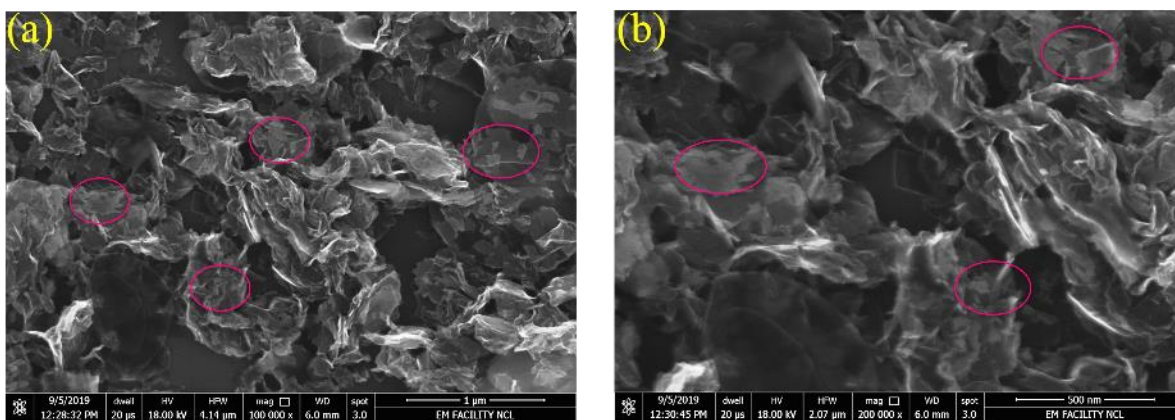

Figure 1. (a) and (b) are the FESEM images of Co@CoAl-LDH/NG.

5.3.1.1. Field-emission scanning electron microscopy analysis

The formation of Co@CoAl-LDH over the in situ generated N-doped graphene is first analyzed through field-emission scanning electron microscopy (FESEM). The bulk morphological investigation of Co@CoAl/NG through FESEM represents the dispersed NG sheets loaded with LDH patches (Figure 1). The loading of LDHs over NG was difficult to uniformly locate owing to the similar texture of both the components. However, the marked places showed the anchoring of discrete LDH patches over NG.

5.3.1.2. Transmission electron microscopy analysis

Subsequent to the confirmation of the LDH and NG composite formation, nanostructural investigations have been comparatively carried out on as-obtained materials *via* detailed transmission electron microscopy (TEM) analysis. From Figure 2a, it can be seen that the urea-assisted hydrothermal treatment of graphene oxide generated thin, transparent, corrugated, and
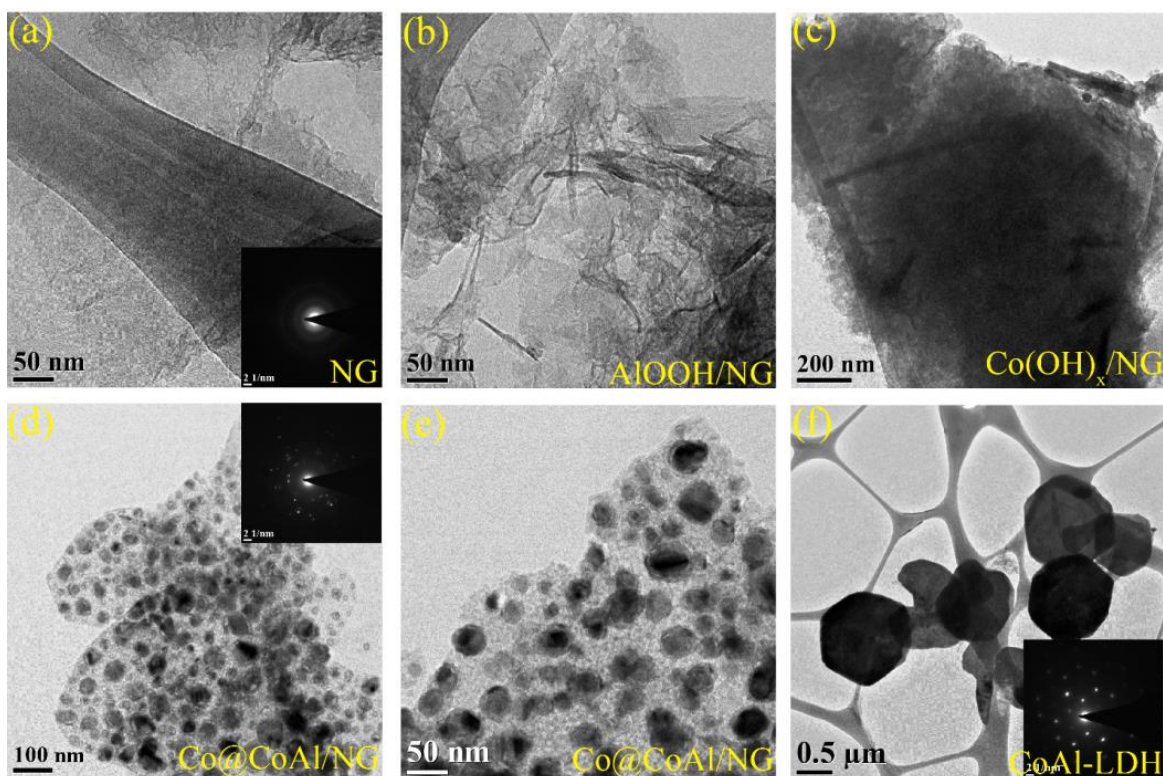
Figure 2. TEM analysis: (a) NG, (b) AlOOH/NG, (c) Co(OH)$_x$/NG, panels (d), (e) are the lower and higher magnification TEM image of Co@CoAl/NG, (f) TEM image of CoAl-LDH. Inset in panel (a), (d) and (f) represents their respective SAED pattern.

scrolled sheets of NG. Under similar reaction conditions, when aluminium salt is added in the Reaction mixture, it also generated indistinguishable thin and crumpled sheet-like structures over NG (Figure 2b). However, in place of Al, when cobalt salt is added, it resulted into thick patches over NG (Figure 2c). Furthermore, when both Al and Co salts are added along with urea in GO solution; it resulted in quite different morphology over NG. As depicted in Figure 2d, the resultant product consists of a nearly homogenous and dense distribution of spherical nanoparticles (NPs) over NG, ranging from 30-50 nm. Noticeably, the anchoring of NPs over NG has also prevented restacking and crumpling of NG (Figure 2d and 2e). For comparison, TEM analysis is also performed on unsupported CoAl-LDH, depicting thicker characteristic hexagonal platelets of LDH with an average size of 1 μm (Figure 2f).

Of note, unsupported LDHs show quite good structural disparity with that of the NG-supported system, which is believed to be due to the combined effect of GO as a substrate as well as its functionalities. In the absence of any support, LDH nucleation, as well as growth, follows a conventional LDH formation pathway.[28] However, in the presence of GO oxygen functionalities, metal ions get plenty of anchoring sites, and hence LDH growth starts in small patches instead of larger and thicker platelets. Inset in Figure 2a, 2d and 2f represents the selected area electron diffraction (SAED) pattern of NG, Co@CoAl/NG, and CoAl-LDH. The SAED pattern of both NG and CoAl-LDH represents single-crystalline nature whereas that of Co@CoAl/NG represents a polycrystalline phase owing to the formation of Co@CoAl-LDH and NG composite.

5.3.1.3. High-resolution transmission electron microscopy analysis

Next, to probe the nanostructural details of the anchored nanoparticles, high-resolution TEM (HRTEM) is performed. Figure 3a represents the HRTEM image of Co@CoAl/NG depicting core-shell type of texture of the spherical NPs. The image is further magnified to study the crystallographic nature of Co@CoAl/NG at the atomic scale. Figure 3b depicts the HRTEM image of a single core-shell nanoparticle along with the zoomed parts in different locations for d-spacing determination. From Figure 3b, it can be seen that as compared to the core, the shell shows broader lattice fringes. When analyzed, the zoomed part of the shell (Box 1) depicts a d-spacing value of ~0.27 nm corresponding to the (012) plane of LDH.[29,30] Nevertheless, the zoomed part near to core (Box 2 and 3) shows narrower fringes, with the d-spacings ranging

from 0.19 to 0.22 nm, particularly corresponding to the metallic core moieties.[31] However, from the crystallographic investigations, a clear cut phase differentiation cannot be made between the core and shell. Instead, the metallic phase is found to be randomly dispersed both in the core and shell having LDH-rich shell.
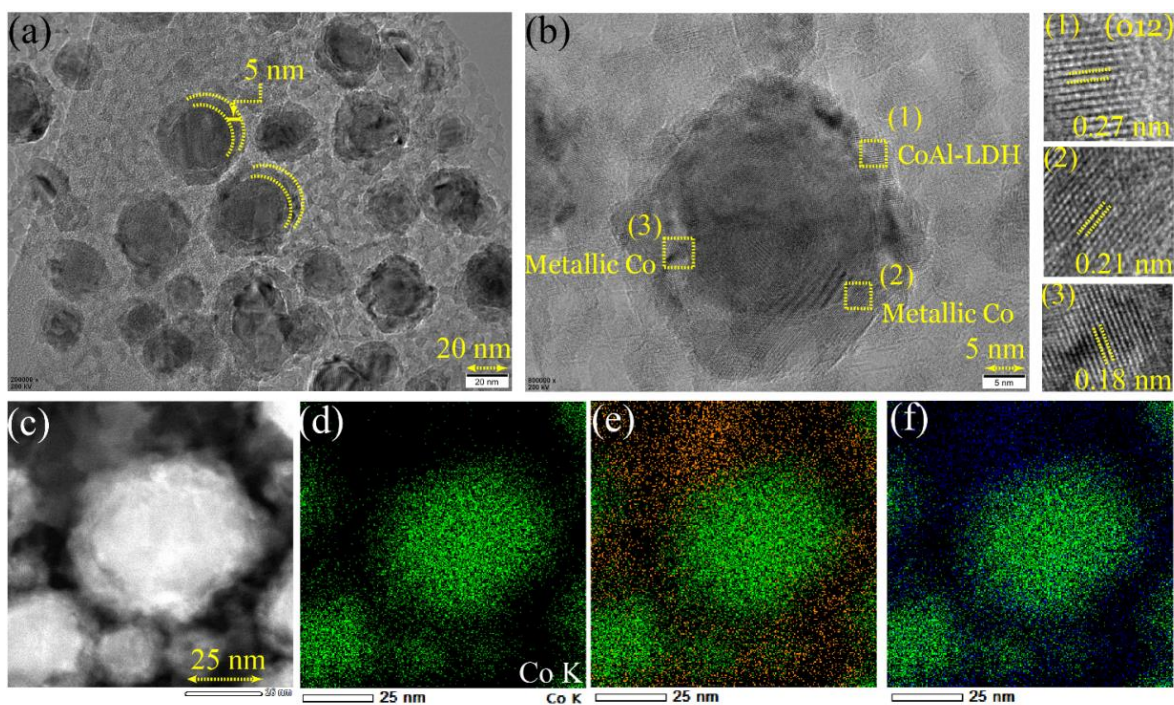

Figure 3. (a) HRTEM image of Co@CoAl/NG, (b) magnified HRTEM image along with the zoomed part in three box regions, (c) HAADF-STEM image, (d) HRTEM-elemental mapping image for Co K, (e) elemental overlapping image for Co and Al, (f) elemental overlapping image for Co and O.

To ascertain our claim regarding the crystallographic nature of core and shell, high angle annular dark-field scanning transmission electron microscopy (HAADF-STEM) was employed. The HAADF-STEM image illustrates the Z-contrast pattern of Co@CoAl/NG having comparatively brighter contrast (higher Z) in the core region, affirming the metallic nature of the core (Figure 3c). Whereas, the shell showed comparatively lighter contrast with diffused circular pattern, illustrating the hydroxide-enriched shell structure. Another invaluable technique to differentiate the chemical nature of the core and shell is the TEM-energy dispersive X-ray spectroscopy (TEM-EDS), providing the elemental distribution profile of the catalyst. Figure 3d represents the

elemental distribution profile for Co, having compact elemental distribution in the core area and scattered distribution in the shell region. To further clarify the elemental distribution of various elements on microscopic level and hence their chemical nature, the overlay distribution profile for Co/Al and Co/O is generated. Figure 3e represents the combined Co/Al elemental distribution profile, affirming the Co-rich core and Al-enriched shell. Interestingly, the Co/O combined elemental distribution profile reveals that the core is metallic with negligible oxygen whereas shell is made-up of oxygen containing moieties, *i.e.,* hydroxides (Figure 3f). Apart from the core-shell region, Al and oxygen are also found to be randomly distributed over NG, illustrating the presence of dispersed thin sheet-like moieties of Al-hydroxides, which may form under the adopted reaction conditions.

5.3.1.4. Probable synthesis mechanism

To understand the reason behind the structural and crystal phase anomaly observed in the presence and absence of GO, detailed synthesis mechanism, basically the dual role played by urea was analyzed. Urea actually can decompose in a very complex and sensitive manner depending upon the reaction conditions.[32] In general, thermal decomposition of urea is proposed to occur in the following manner;[32]

$$H_2N–CO–NH_2 + \Delta \rightarrow NH_4^+NCO^- \text{ (ammonium cyanate)}$$
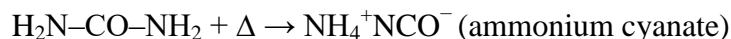
where, as-generated NH_4^+ may interact with the oxygen functionalities of GO and induce N-doping under the hydrothermal condition.[33] And, according to Mavis *et al.* the as-created cyanate moieties may first coordinate with the metal ions during the nucleation and growth of precipitates to generate metal–cyanate complexes in various geometries (N-bonded, O-bonded or bridge-bonded).[34] However, as the pH of the reaction solution rises, these weakly bonded metal–cyanate complexes gradually decompose and transform into hydroxides.[34] In the meantime, the remnant cyanate moieties along with water and carbonate species can get intercalated into the interlayer space. Despite the hydroxide growth, these metal–cyanate complexes, basically the N-bonded ones which dominates in the initial stages, may help to introduce M–N bonding in the product precipitates.[31] As examined earlier, the generated M–N bonding moieties eventually get decompose during the course of the reaction and create metallic nanostructures.[31] Hence, these

earlier studies can help us to easily explain the chemistry behind the as-observed disparity in the growth pattern in the presence and absence of GO. Actually, in the presence of GO with similar urea concentration, some of the urea may get involved in N-doping and decompose differently, hence, the average urea concentration required for LDH formation may fall. Moreover, in the presence of GO the pH of the water will be slightly acidic, which eventually leads to lower overall pH as compared to the one in the absence of GO. Hence, we believe that with comparatively lower pH, all the metal–cyanate complexes may not be able to transform into hydroxides. It is when some of the metal–cyanate complexes may get the chance to eventually transform into metallic moieties. Notwithstanding, the peripheral metal-cyanate complexes can easily get a good exposure of OH$^-$ to convert into the hydroxides, assisting the LDH shell growth.

5.3.1.5. X-ray photoelectron spectroscopy analysis

To study the invaluable role of the urea-assisted hydrothermal treatment toward both GO reduction, as well as N-doping in the as-generated graphene, a detailed X-ray photoelectron spectroscopy analysis, is performed. Figure 4a represents the comparative C 1s spectrum of GO and Co@CoAl/NG, where, as compared to two the intense peaks in GO, Co@CoAl/NG show only one intense peak. Moreover, the deconvoluted spectra of Co@CoAl/NG shows intense fitted C=C sub-peak at ~284.5 eV, illustrating the success of the hydrothermal treatment toward reducing the oxygen functionalities of GO to generate the honeycomb lattice of graphene.[35] Reduction of GO oxygen functionalities can also be supported by the diminished intensity of the fitted sub-peaks corresponding to C–O (~287.3–288.0 eV) and O–C=O (~290.5 eV) of Co@CoAl/NG and NG (Figure 3a).[35] Next, to support our claim of the metal–cyanate complex formation as well as N-doping *via* urea-sourced hydrothermal treatment, XPS analysis was carried out in N 1s core level region. Figure 4b represents the deconvoluted N 1s spectra of Co@CoAl/NG, affirming the N-doping *via* various types of N-functionalities created in the carbon lattice, *i.e.,* pyridinic (~398–399 eV), pyrrolic (~400 eV), quaternary (~401 eV) and N-oxides (~405 eV).[35,33] To ascertain the formation of the metal–cyanate complexes during the LDH formation, Figure 4b also consists of the deconvoluted N 1s peak for CoAl-LDH. As compared to Co@CoAl/NG, CoAl-LDH shows a single broader peak near 401.5 eV,

corresponding to the remnant metal–cyanate complexes.[31] Hence, from the comparative XPS spectra in Figure 4b, one can conclude that in the case of Co@CoAl/NG, the peak for metal–cyanate complexes must be merged with that of quaternary N functionalities.
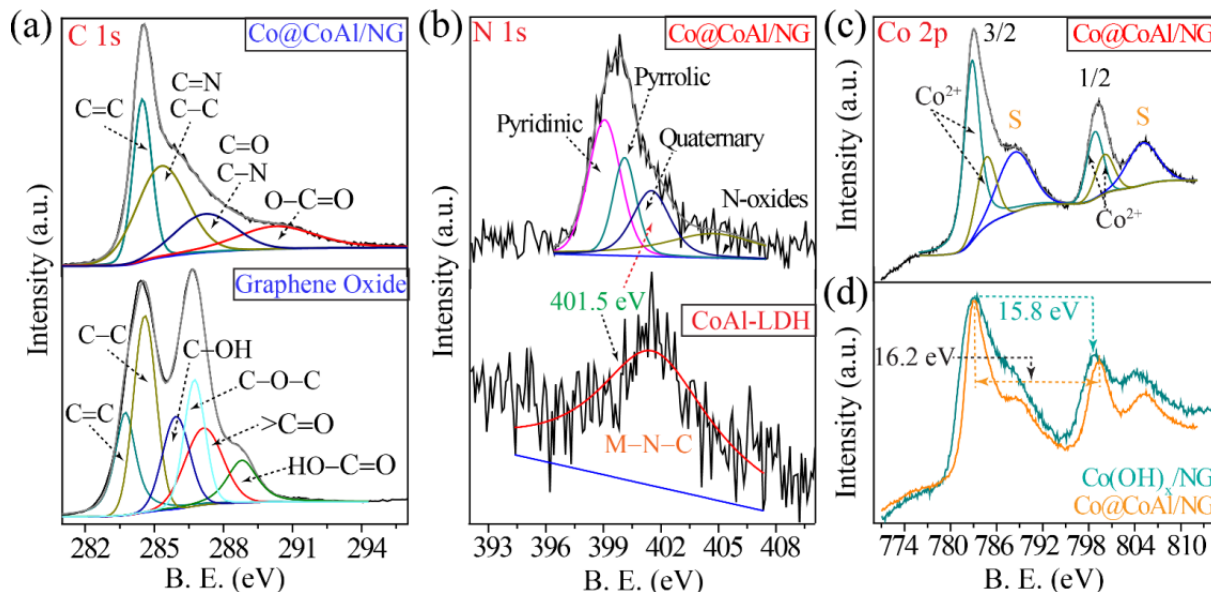
Figure 4. Comparative XPS analysis: (a) deconvoluted C 1s spectra of graphene oxide and Co@CoAl/NG, (b) deconvoluted N 1s spectra of CoAl-LDH and Co@CoAl/NG, (c) deconvoluted Co 2p spectra of Co@CoAl/NG, (d) Co 2p spectra of Co(OH)$_x$/NG and Co@CoAl/NG depicting the peak splitting values.

Next, for the elucidation of the chemical nature of Co as well as to prove the presence of metallic component in the catalyst system, comparative Co 2p core level study is performed for various synthesized samples. Figure 4c represents the deconvoluted Co 2p core-level spectra for Co@CoAl/NG, comprising two 2p$_{3/2}$ (782.9 eV and 784.7 eV) and two 2p$_{1/2}$ (798.8 eV and 800.2 eV) sub-peaks affirming that Co is present in +2 oxidation state.[36] However, to ascertain the presence of metallic Co, comparable Co 2p core level is analyzed for Co@CoAl/NG and Co(OH)$_x$/NG. As depicted in Figure 4d, Co@CoAl/NG shows higher spin-orbit splitting value (ΔE) of 16.2 eV as compared to 15.8 eV for Co(OH)$_x$/NG. This larger peak splitting value of 16.2 eV is a good indication for having a fraction of metallic character in Co@CoAl/NG along with the Co^{2+} states.[37] To further support our claim of metal–cyanate complex formation as well as its decomposition to metallic moieties, relative Co 2p core level is analyzed for Co@CoAl/NG

and unsupported CoAl-LDH. As depicted in Figure 5a, the two Co 2p core-level spectra show similar peak pattern as well as energy splitting value of ~16.2 eV corresponding to the presence of metallic moieties along with Co^{2+} state. Hence, XPS analysis has been found as an essential tool to detect the metallic moieties generated and supports our HRTEM findings. Next, to study the chemical nature of the Al present in our catalyst system, XPS peak is deconvoluted in the Al 2p region. As illustrated in Figure 5b, the Al 2p core level can be fitted in two sub-peaks corresponding to $Al(OH)_3$ and AlOOH with a binding energy of 74.3 eV and 75.7 eV, respectively.[38,39] The Al 2p illustrates that Al is present in +3 state with surface-enriched AlOOH phase.
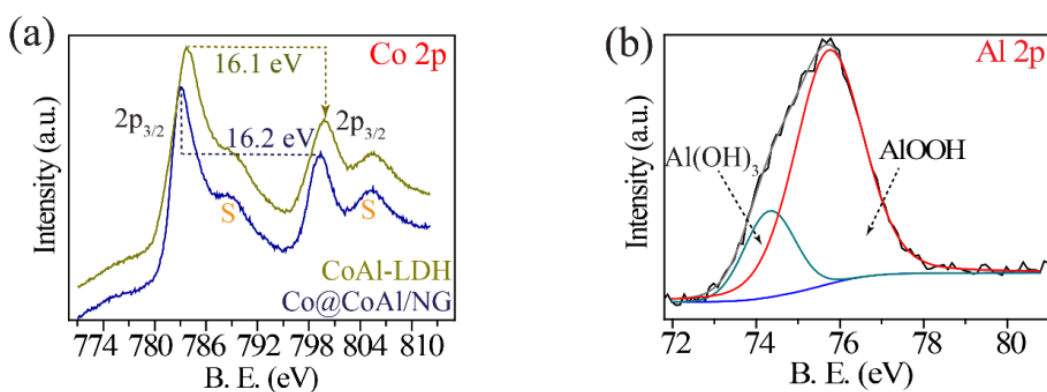

Figure 5. XPS analysis: (a) Comparative Co 2p XPS spectra of CoAl-LDH and Co@CoAl/NG, (b) deconvoluted Al 2p spectra of Co@CoAl/NG.

5.3.1.6. X-ray diffraction analysis

Subsequent to the morphological and surface electronic structure investigations, bulk phase and crystallinity of the as-synthesized materials were characterized through PXRD. The comparative PXRD pattern of GO and NG (Figure 6a) supports the XPS findings of the invaluable role of the hydrothermal treatment to reduce GO to N-doped graphene (NG) even at a temperature as low as 180 °C. As illustrated in Figure 6a, after the hydrothermal treatment, the (001) peak of GO located at ~9.9° disappears, while a broad diffraction peak at about 25.5° corresponding to (002) plane of reduced graphene oxide emerges.[33] Figure 6b illustrates the comparative X-ray diffraction pattern of unsupported CoAl-LDH and NG supported Co@CoAl-LDH, depicting the presence of hydrotalcite-like characteristic (00*l*) planes of layered double hydroxide (ICDD card

no. 00-38-0715).[14,40] However, Co@CoAl/NG does not show any metallic cobalt signature. In addition to the LDH diffraction planes, Co@CoAl/NG comprises characteristics (002) plane of NG, affirming the *in situ* growth of Co@CoAl over NG. XRD analysis is also extended on Co(OH)$_x$/NG and AlOOH/NG. Noticeably, Co(OH)$_x$/NG is found to exhibit similar peak pattern to that of LDH, demonstrating that the adopted synthesis conditions lead to the formation of layered α-cobalt hydroxide (Figure 6c). However, the diffraction pattern of AlOOH/NG showed apparent phase disparity and confirmed the formation of pseudo-boehmite phase (Figure 6d) under the adopted reaction conditions.[41]
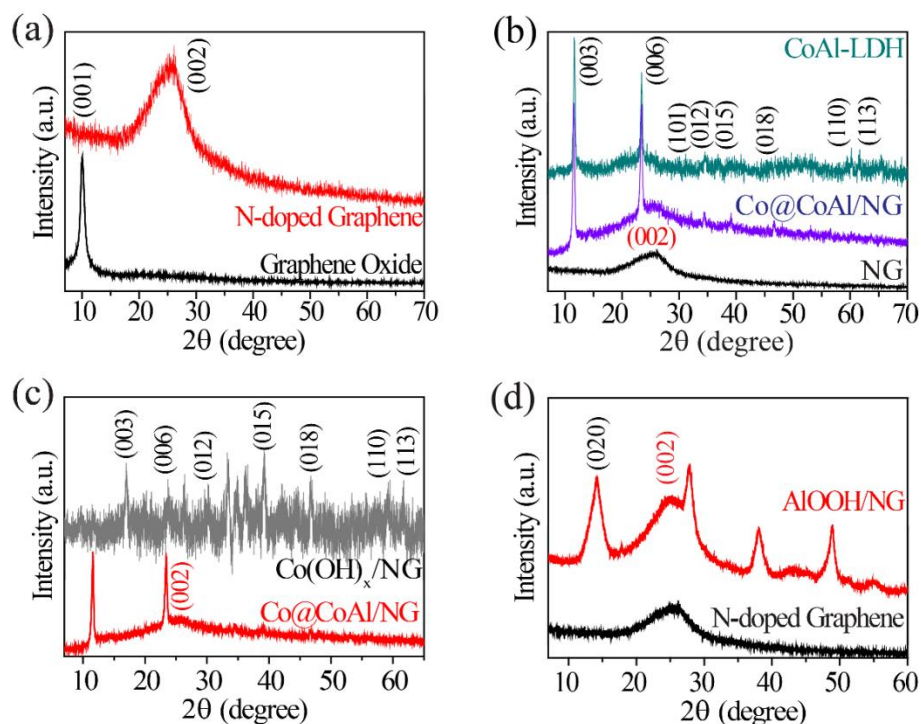
Figure 6. Comparative PXRD analysis: (a) GO and N-doped graphene, (b) CoAl-LDH and Co@CoAl/NG, (c) Co(OH)$_X$/NG and Co@CoAl/NG, (d) NG and AlOOH/NG.

5.3.1.7. Raman analysis

Next, to the crystal phase identification, Raman analysis is employed to study the defects and dopant characteristics induced during the *in situ* GO reduction and N-doping. Raman spectra of GO, NG, and Co@CoAl/NG exhibit two prominent peaks at nearly similar positions of ~1333 and ~1600 cm^{-1}, corresponding to the D and G-band, respectively (Figure 7).[42] The intensity ratio of these two bands, *i.e.,* I$_D$/I$_G$, is used as an indicator of interpreting the defect disorder and

N-doping.[42] The I_D/I_G ratio obtained for NG and Co@CoAl/NG is found to be nearly similar (~1.16) and lower than that of GO (~1.20). These findings are consistent with the increased orderness in the graphene matrix after GO reduction.
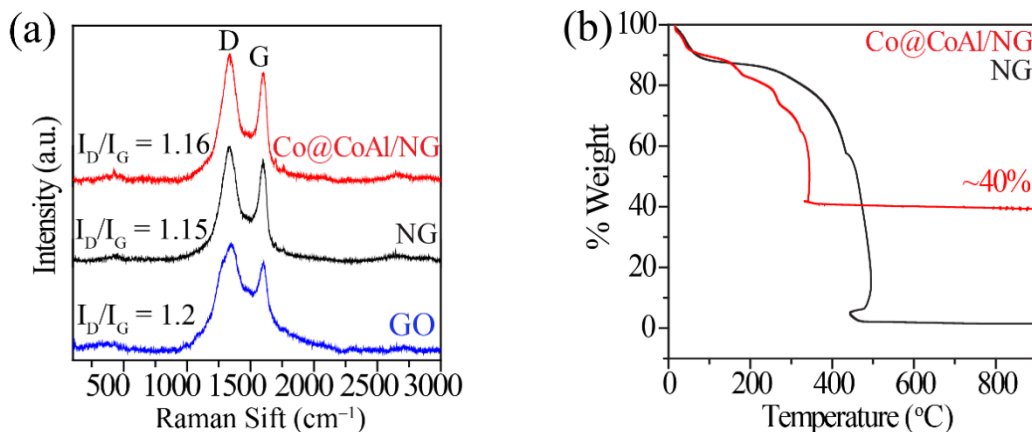
Figure 7. Comparative: (a) Raman spectra, (b) TGA plots.

5.3.1.8. Thermo-gravimetric analysis

Finally, the loading of Co@CoAl-LDH over NG is analyzed through thermo gravimetric analysis (TGA). Figure 8 represents the comparative TGA plots of Co@CoAl/NG and NG, representing approximately 35–40% loading of the active material over NG.

5.3.2. Electrochemical Analysis

Altogether, the HRTEM, XPS, and PXRD rationalize the success of our one-pot synthesis strategy of decorating Co@CoAl-LDH core-shell nanostructures over the *in situ* generated N-doped graphene. In a single-step hydrothermal treatment, reduction of GO to graphene, N-functionalities introduction, core-shell nanostructure growth, as well as their anchoring, was realized. Moreover, with this work, we were able to not only reduce the cost of material synthesis but also we chose cheaper as well as least-toxic metals, precipitating agent, and solvent. These catalyst designing superiorities now will be taken for their viability to translate into a robust bifunctional electrocatalyst. To distinguish the uniqueness of the designed catalyst from its unitary counterparts, the two half-cell reactions, *i.e.,* HER and ORR, are first tested. The best-performing catalyst is then employed to fabricate and test a home-made dual-mode Al-based battery.

5.3.2.1. Electrocatalytic HER performance

As compared to the proton-enriched acidic electrolyte, HER is relatively slower in an alkaline medium because of the poor availability of protons.[43] Hence, in the case of an alkaline medium, HER process requires an additional effort to obtain H^+ by water dissociation near to active centers.[25] In this context, an ideal HER catalyst should be heterostructured comprising of a combination of three catalytically essential components, *i.e.,* water dissociation component, proton reducing component and electronically conducting component. Considering this, herein, we offer a single-step catalyst designing strategy for the development of a robust electrocatalyst which can bestow us a fascinating synergistic interplay of the required components to boost-up the overall reaction process of alkaline HER.
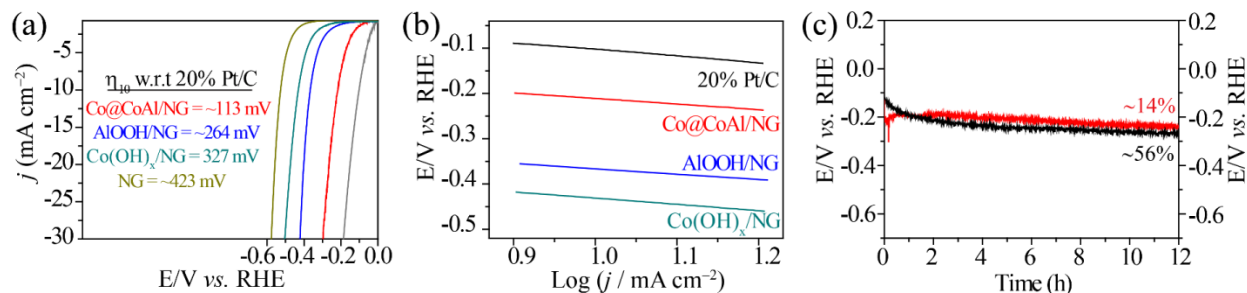
Figure 8. Comparative HER analysis: (a) LSV plots, (b) Tafel plots, (c) chronoamperometric (CP) stability test.

To access our catalytic designing viability, HER activity was first analyzed by employing a linear sweep voltammogram technique. Figure 9a represents the comparative HER polarization curves in alkaline medium where as compared to the commercial Pt/C, our catalyst required only 113 mV overpotential to reach the benchmark 10 mA cm^{-2}. As compared to the main catalyst, the unitary components, *i.e.,* Co(OH)$_x$/NGr and AlOOH/NGr show lower performances, further corroborating the crucial role played by the hybrid system to enhance the HER performance. Next to the activity, reaction kinetics, as well as the involved reaction mechanism on the designed catalysts, is accessed through Tafel analysis. As depicted in Figure 9b, the Tafel slope value for all the mentioned catalysts lies in the range of 110 to 140 mV dec^{-1}, emphasizing the role of the Volmer step involving water dissociation ($2H_2O + M + 2e^- \leftrightarrow 2M\text{-}H_{ad} + 2OH^-$) as the

rate-determining step.[25,26] Lastly, the electrocatalytic stability of the designed material is analyzed by performing chronopotentiometry at 10 mA cm^{-2}. Figure 9c displays the comparative chronopotentiometric stability test profile of Co@CoAl/NG and 20% Pt/C, depicting quite good catalytic stability with the designed catalyst as compared to the commercial catalyst. The commercial catalyst showed ~56% catalytic performance degradation after 12 h of continuous operation as compared to only ~14% degradation with the designed catalyst, illustrating outstanding catalytic stability toward hydrogen generation.

5.3.2.2. Electrocatalytic ORR performance

Next to the HER activity, ORR performance of the as-synthesized catalysts is comparatively analyzed. Figure 10a represents the comparative LSV plots from where one can see that as compared to the commercial Pt/C catalyst, our catalyst shows mere ~40 mV overpotential shift in the half-wave potential (E$_{1/2}$, voltage at the half of the total kinetic current) region. It is interesting to note that as compared to Co(OH)$_x$/NGr, AlOOH/NGr exhibited better performance in terms of E$_{1/2}$, supporting the crucial role played by poorly-explored Al moieties in the field of ORR electrocatalysis. It is one of the interesting findings of our work to introduce the cheaper as well as environmental-friendly metal like Al for catalyzing one of the most demanding reactions in the field of electrochemical power sources.
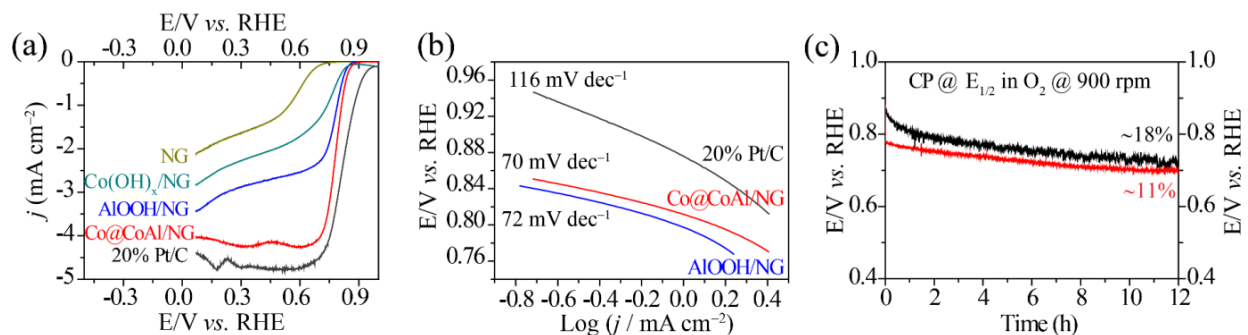

Figure 9. Comparative ORR analysis: (a) LSV plots, (b) Tafel plots, (c) chronoamperometric (CP) stability test.

Similar to HER, ORR reaction kinetics is also studied through Tafel analysis, and the comparative Tafel plots are given in Figure 10b. As depicted in panel 10b, reaction kinetics is

found to be better on the synthesized catalysts as compared to the reference sample which is consistent with the LSV feature in the onset region. Where, the reference sample is found to show higher voltage shift *w.r.t.* the per decade of current increment as compared to the designed catalysts. Next to the activity evaluation, electrochemical stability of Co@CoAl/NG toward ORR was comparatively analyzed with 20% Pt/C through chronopotentiometric (CP) stability test for 12 h in O_2 atmosphere with 900 rpm. Figure 10c represents the comparative CP plots, displaying better catalytic stability of Co@CoAl/NG with ~90% performance retention after 12 h of operation as compared to ~82% performance retention in the case of the commercial catalyst.
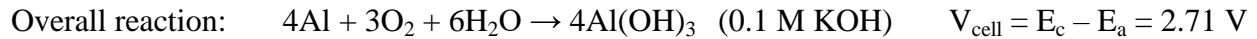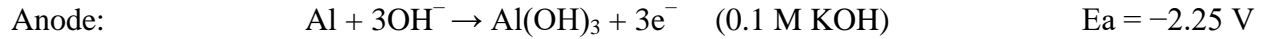
5.3.2.3. Dual-Mode Al-based Battery Performance Evaluations

Based on the half-cell performance results, Co@CoAl/NG is employed as a cathode to fabricate a dual-mode Al-based battery. As a reference performance indicator, another system based on the commercial Pt/C coated cathode is also employed. As it is already mentioned, the intention to introduce bifunctionality into the catalyst system as well as to demonstrate the dual-mode battery is for the validation of the newly developed strategy of harvesting the energy generated during the self-sustained Al-water reaction for H_2 production. Another interesting highlight of our work is that we have used a weak KOH concentration of 0.1 M KOH to avoid any spillage corrosion caused by the higher KOH concentration as well as to balance the kinetics of the two half-cell reactions. Since, as compared to the cathodic half-cell reactions (HER/ORR), Al oxidation rate will be much faster in higher KOH concentration.

Before going to the discussion on the obtained battery results, a brief reaction pathway on the two half-cell reactions in the two as-proposed battery modes is described. As illustrated in Figure 11a, during the Al-O_2 mode, on the anode side, the electropositive Al foil gets oxidize and the release electrons which travel through the outer circuit and generate electricity. These electrons then reach to the air-breathing cathode, where O_2 from the oxygen saturated electrolyte gets reduce to complete the circuit.

Hence, in the presence of O_2, the electrochemical reactions on each electrode can be described as follows:

Cathode: $\qquad\qquad O_2 + 2H_2O + 4e^- \rightarrow 4OH^-$ $\quad$ (0.1 M KOH) $\qquad\qquad$ Ec = 0.46 V

Anode: $Al + 3OH^- \rightarrow Al(OH)_3 + 3e^-$ (0.1 M KOH) $E_a = -2.25$ V

Overall reaction: $4Al + 3O_2 + 6H_2O \rightarrow 4Al(OH)_3$ (0.1 M KOH) $V_{cell} = E_c - E_a = 2.71$ V
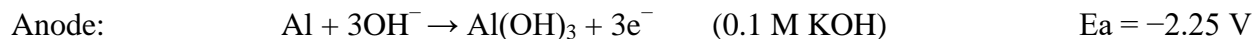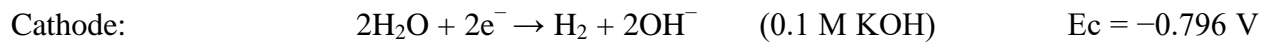
According to the above-mentioned mechanism, theoretically, the cell is able to offer an open circuit voltage (OCV) of 2.71 V; however, practically maximum achieved OCV lies in the range of ~1.4–1.6 V.

Similarly, in the case of the Al-H_2O mode (Figure 11b), the released electrons reach the cathode and in the absence of O_2 (*via* N_2 purging) reduce the H_2O in the vicinity and liberate H_2 to complete the circuit.

In the Al-H_2O mode, the two half-cell reactions can be described as follows:

Cathode: $2H_2O + 2e^- \rightarrow H_2 + 2OH^-$ (0.1 M KOH) $E_c = -0.796$ V
Anode: $Al + 3OH^- \rightarrow Al(OH)_3 + 3e^-$ (0.1 M KOH) $E_a = -2.25$ V

Overall reaction: $2Al + 6H_2O \rightarrow 3H_2 + 2Al(OH)_3$ (0.1 M KOH) $V_{cell} = E_c - E_a = 1.45$ V

Hence, in Al-H_2O mode the cell can theoretically generate a maximum OCV of 1.45 V.

In spite of the theoretical OCV of 2.71 V, practically in Al-O_2 mode with 0.1 M KOH, the maximum achieved OCV for Co@CoAl/NG is found to be ~1.33 V which is somewhat lesser than that of Pt/C, *i.e.,* ~1.5 V. Nevertheless, the obtained OCV is found to be sufficient to represent the feasibility of the designed catalyst-coated cathode for the Al-O_2 battery. With the obtained OCV values, the fabricated cells are first discharged at 5 mA cm^{-2} in Al-O_2 mode and the comparative discharge profile of the catalyst with the commercial catalyst is given in Figure 11c. Although Pt/C showed higher voltage throughout the discharging process, discharge time for the designed catalyst is observed to be longer, probably owing to the similar polarizability of the two half-cell reactions with Co@CoAl/NG-coated cathode. It is reflected into higher specific capacity (~657 mAh g^{-1}) value for the designed catalyst as compared to that of commercial catalyst (492 mAh g^{-1}).

After the Al-O_2 mode demonstration, the device is reconstructed in the Al-H_2O mode by removing any dissolved O_2 *via* N_2 purging. This resulted into the lowering of the observed cell voltage, *i.e.,* ~1.3 V and ~1.24 V with Pt/C- and Co@CoAl/NG-coated cathode, respectively. This voltage decrement is obvious owing to the lower theoretical voltage of 1.48 V for Al-H_2O mode. It is interesting to note that, in the case of the Al-O_2 mode, there is a huge cell voltage gap between the theoretical and practically obtained value, primarily due to the self-corrosion issue. Nevertheless, in the case of the Al-H_2O fuel cell, this potential gap is comparatively low, verifying the better energy efficiency of the Al-H_2O mode over the Al-O_2 mode, in fact it can also take the benefit of H_2 generating during the self-corrosion and store it. Hence, with the above mentioned superiorities, the Al-H_2O fuel cell is first discharged at 5 mA cm^{-2} current drag, illustrating the similar discharge pattern (Figure 11d) as it is observed in the Al-O_2 mode. Hence, the observed trend emphasizes the importance of our designed catalyst over the commercial catalyst to achieve higher discharge capacity.
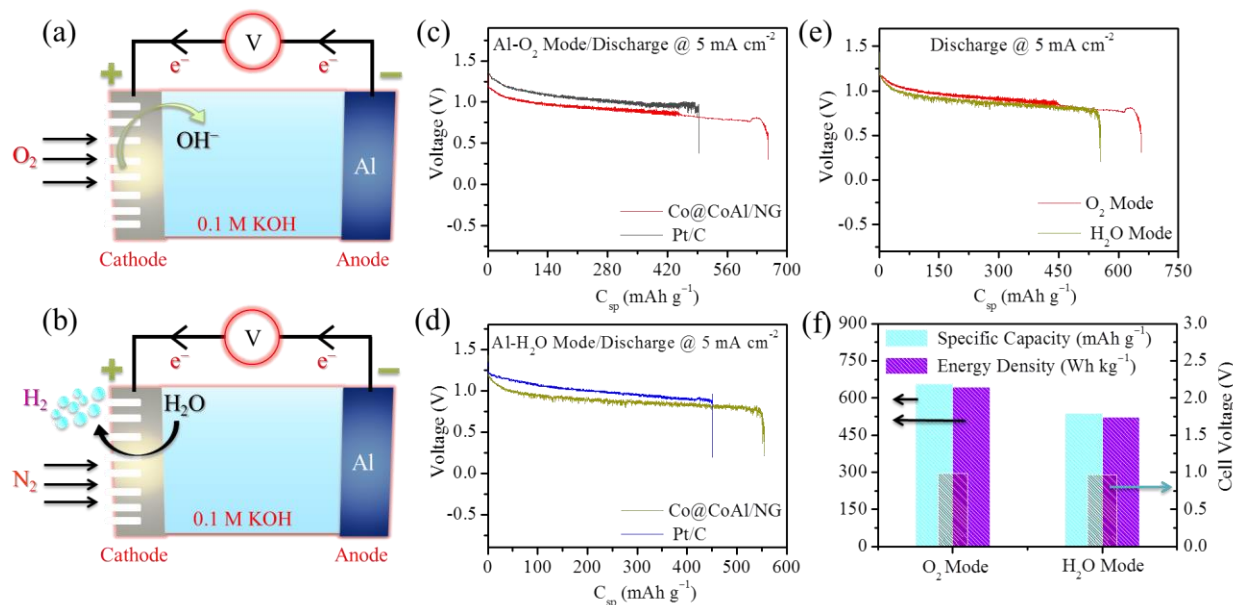
**Figure 10.** Schematic illustrations: (a) Al-O_2 mode (b) Al-H_2O mode. Comparative galvanostatic discharge profile @ 5 mA cm^{-2}: (c) Al-O_2 mode (d) Al-H_2O mode. (e) Comparative galvanostatic discharge profile for Co@CoAl/NG in Al-O_2 and Al-H_2O mode, (f) comparative specific capacity, energy density and average voltage panels for Co@CoAl/NG @ 5 mA cm^{-2} in Al-O_2 and Al-H_2O mode.

With the Al-H$_2$O mode at a discharge current drag of 5 mA cm^{-2}, our catalyst delivered a specific capacity of ~538 mAh g^{-1} which is comparable to that of the Al-O$_2$ mode (Figure 11f). Hence, the achieved Al-H$_2$O mode performance highlights the importance of our newly-proposed concept of harvesting the electrochemical energy from the exothermic water-aluminium reaction. The observed performance in the Al-H$_2$O mode is comparatively tabulated with the similar reported devices as Table 1. The tabulated results show the superiorities of our as-developed device over previously designed devices both in terms of performance and energy efficiency.

Table 1. Performance comparison of our as-proposed Al-H$_2$O fuel cell with the reported Li- H$_2$O and Zn- H$_2$O cells:

Device Type	Open Circuit Voltage (V)	Average Cell Voltage (V) @ 5 mA cm^{-2}	Energy Efficiency (%)	Reference
Al-H$_2$O	~1.24	~0.95	~77	Present Work
Li-H$_2$O	~2.2	~1.25	~57	[22]
Zn-H$_2$O	~0.4	~0.35	~87	[22]

Subsequent to the successful validation of the as-proposed concept of simultaneous H$_2$ and electricity generation, the device is also fabricated with the laboratory-waste aluminium. The composition of both the battery-grade and waste aluminium is accessed through SEM-EDS and given as Figure 12a and Figure 12b, respectively. Where, the SEM-EDS profile for battery-grade Al showed the presence of 100% Al with no impurity, whereas the waste-Al showed the presence of ~27% Al, ~27% carbon and ~41% oxygen, as the major components. With the above two Al-grade foils, the device is galvanostatically discharged in Al-H$_2$O mode at 5 mA cm^{-2} current density. As depicted in Figure 12a, even with lower Al composition, surprisingly, the waste-Al-based device show better performance to that of the system based on the pure Al. This could be likely attributable to the slower corrosion rate of Al in the waste-Al as compared to that
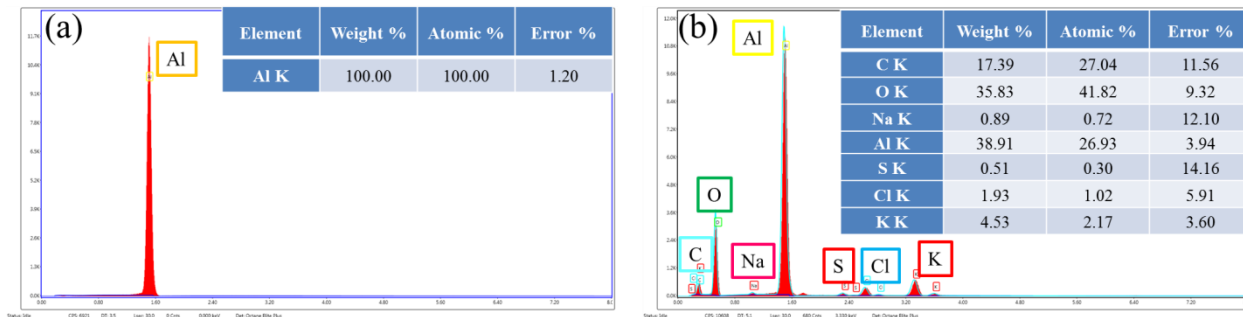
Figure 11. SEM-EDS spectrum: (a) Battery-grade aluminium, (b) laboratory-waste Al.

with pure Al foil. However, with this work our intention is not to explore the effect of any alloying agent on the performance, but only the utilization of the laboratory waste for useful purpose. In addition, comparatively flatter discharge profile with waste Al allowed us to demonstrate the device even at higher current drag. Figure 12b represents the comparative discharge profile of the waste Al-based device at 10 mA cm^{-2} current drag in both the Al-H$_2$O mode and Al-O$_2$ mode. It manifests that the waste-Al based anode is able to sustain in fact higher current drag in both the battery mode and showed quiet stable discharge plateau. The voltage obtained as well as the life of battery is found to be lesser in the Al-H$_2$O mode which is obvious since more amount of the generated energy will be utilized to liberate H$_2$ at higher current density *via* the H$_2$O reduction. The corresponding specific capacity, energy density and average cell voltage of the Al-based battery in the two adopted modes at a current drag of 10 mA cm^{-2} are comparatively illustrated in Figure 12c.

Next to the device-level performance demonstration, gas chromatography analysis was employed to practically detect the product generating. Figure 12d represents the graph representing the comparative amount of the hydrogen generated before and during the 15 minute discharge at 5 mA cm^{-2} drag current with battery-grade and waste Al. As can be seen from the right Y-axis of the plot, both before and after the discharge test, amount of H$_2$ generated is higher with the battery-grade Al as compared to waste Al. This higher amount of H$_2$ detected with the battery-grade Al suggests the higher self-corrosion rate as compared to the waste Al which is already observed in the previous sections. Notwithstanding, this study shows the additional advantage of our as-proposed concept to collect as well as utilize the valuable H$_2$ evolving through the unavoidable self-corrosion which otherwise left unutilized during the Al-air battery technology.
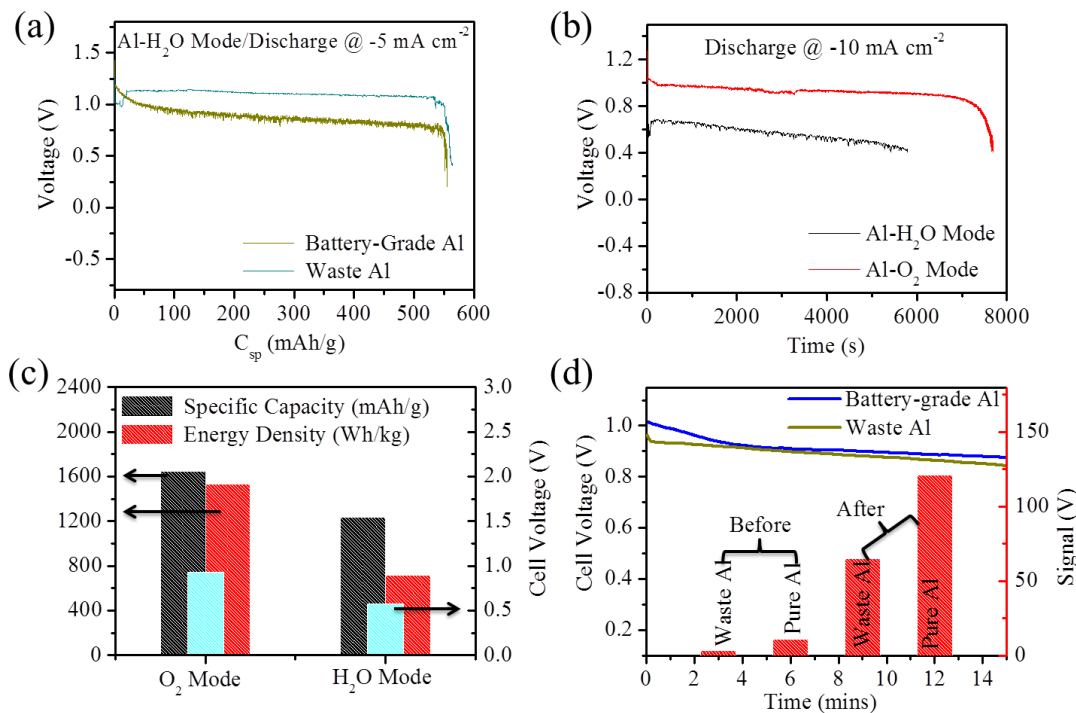
Figure 12. (a) Comparative galvanostatic discharge profile of Co@CoAl/NG with battery-grade and waste Al @ 5 mA cm^{-2} in Al-H$_2$O Mode. Comparative (b) discharge plateau and (c) specific capacity, energy density and average cell voltage representation of Co@CoAl/NG with waste Al @ 10 mA cm^{-2} in Al-O$_2$ and Al-H$_2$O Mode. (d) Comparative GC analysis data for H$_2$ detection as well as quantification with battery-grade and waste Al-based Al-H$_2$O device discharged at 5 mA cm^{-2} for 15 minutes.

5.4. Conclusion

In summary, herein, we have developed a unique concept to both generate H$_2$ as well as harvest the energy liberated during the exothermic Al-H$_2$O reaction of H$_2$ production. The as-proposed concept of simultaneous H$_2$ and electricity generation was also able to address the issues associated with the previously developed Li-H$_2$O and alkaline-acid Zn-H$_2$O fuel cell in terms of safety and price. The chosen metal, *i.e.,* Al is proven to be the perfect metal both in terms of its abundance as well as energy density. In addition to this, we also developed a bifunctional electrocatalyst which showed impressive performance toward catalyzing the cathodic half-cell reactions in the two as-projected battery modes. The designing of a core-shell structure resulted into the synergistic interplay between the electron-rich metallic core and hydroxyl-enriched shell

to boost-up the HER and ORR reaction kinetics. Furthermore, when employed in device, our catalyst performed equally efficiently to that of the commercial Pt-based catalyst. In this way, our as-developed concept as well as catalyst designing strategy may help to provide a new direction both for the emergence of new energy-efficient H_2 generation strategies as well as for the low-cost proficient catalyst designing.

5.5. References

1   I. Staffell, D. Scamman, A. V. Abad, P. Balcombe, P. E. Dodds, P. Ekins, N. Shah and K. R. Ward, *Energy Environ. Sci.*, 2018, **12**, 463.
2   K. W. A. Guy, *Process Saf. Environ. Prot.*, 2000, **78**, 324–327.
3   B. Obama, *Science,* 2017, **355**, 126–129.
4   Z. W. She, J. Kibsgaard, C. F. Dickens, I. Chorkendorff, J. K. Nørskov and T. F. Jaramillo, *Science,* 2017, **355**, 146–157.
5   J. O. Bockris, *Science*, 1972, **176**, 1323.
6   M. R. Lukatskaya, B. Dunn and Y. Gogotsi, *Nat. Commun.*, 2016, **7**, 1–13.
7   J. A. Turner, *Science*, 2004, **305**, 972–974.
8   D. M. F. Santos, C. A. C. Sequeira and J. L. Figueiredo, *Quim. Nova*, 2013, **36**, 1176–1193.
9   Y. X. Chen, A. Lavacchi, H. A. Miller, M. Bevilacqua, J. Filippi, M. Innocenti, A. Marchionni, W. Oberhauser, L. Wang and F. Vizza, *Nat. Commun.*, 2014, **5**, 4036.
10   H. Jin, J. Joo, N. K. Chaudhari, S. Choi and K. Lee, *ChemElectroChem*, 2019, **6**, 3244–3253.
11   Y. Yan, B. Y. Xia, B. Zhao and X. Wang, *J. Mater. Chem. A*, 2016, **4**, 17587–17603.
12   M. I. Jamesh, *J. Power Sources*, 2016, 333, 213–236.
13   W. Zhang and K. Zhou, *Small*, 2017, **13**, 1–18.
14   A. Nadeema, V. M. Dhavale and S. Kurungot, *Nanoscale*, 2017, **9**, 12590–12600.
15   T. Take, K. Tsurutani and M. Umeda, *J. Power Sources*, 2007, **164**, 9–16.
16   J. Y. Zhang, X. Tian, T. He, S. Zaman, M. Miao, Y. Yan, K. Qi, Z. Dong, H. Liu and B. Y. Xia, *J. Mater. Chem. A*, 2018, **6**, 15653–15658.
17   B. K. Boggs, R. L. King and G. G. Botte, *Chem. Commun.*, 2009, 4859–4861.
18   A. Nadeema, V. Kashyap, R. Gururaj and S. Kurungot, *ACS Appl. Mater. Interfaces*, 2019, **11**, 25917-25927.
19   Y. Huang, X. Chong, C. Liu, Y. Liang and B. Zhang, *Angew. Chemie - Int. Ed.*, 2018, **57**, 13163–13166.
20   J. Jiang, M. Chang and P. Pan, *Environ. Sci. Technol.*, 2008, **42**, 3059–3063.
21   Z. Guo, Y. Wang, Y. Song, C. Li, X. Su, Y. Wang, W. Bin Cai and Y. Xia, *ACS Energy Lett.*, 2017, **2**, 36–44.
22   Y. Wang, L. Chen, X. Yu, Y. Wang and G. Zheng, *Adv. Energy Mater.*, 2017, **7**, 1–7.
23   P. Cai, Y. Li, G. Wang and Z. Wen, *Angew. Chemie - Int. Ed.*, 2018, **57**, 3910–3915.
24   V. Rosenband and A. Gany, *Int. J. Hydrogen Energy*, 2010, **35**, 10898–10904.
25   R. Subbaraman, D. Tripkovic, D. Strmcnik, K. C. Chang, M. Uchimura, A. P. Paulikas, V. Stamenkovic and N. M. Markovic, *Science,* 2011, **334**, 1256–1260.
26   Z. Liang, H. S. Ahn and A. J. Bard, *J. Am. Chem. Soc.*, 2017, **139**, 4854–4858.
27   D. C. Marcano, D. V. Kosynkin, J. M. Berlin, A. Sinitskii, Z. Sun, A. S. Slesarev, L. B. Alemany, W. Lu and J. M. Tour, *ACS Nano*, 2018, **12**, 2078–2078.
28   Z.-H. Liu, Z. Yang, K. Ooi, T. Wang, Z. Wang, X. Tang, L. Fan and Y. Han, *Chem. Mater.*, 2007, **20**, 360–363.
29   Z. Wang, P. Fang, P. Kumar, W. Wang, B. Liu, J. Li, Z. Wang, P. Fang, P. Kumar, W. Wang, B. Liu and J. Li, *Nanomaterials*, 2019, **9**, 807.
30   S. Kumar, L. J. Durndell, J. C. Manayil, M. A. Isaacs, C. M. A. Parlett, S. Karthikeyan, R.E. Douthwaite, B. Coulson, K. Wilson, Prof. A.F. Lee, *Part. Part. Syst. Charact.*, 2018, **35**, 1700317.
31   X. Ge, C. D. Gu, X. L. Wang and J. P. Tu, *Chem. Commun.*, 2015, **51**, 1004–1007.
32   P. M. Schaber, J. Colson, S. Higgins, D. Thielen, B. Anspach and J. Brauer, *Thermochim. Acta*, 2004, **424**, 131–142.
33   Y. Chen, B. Xie, Y. Ren, M. Yu, Y. Qu, T. Xie, Y. Zhang and Y. Wu, *Nanoscale Res. Lett.*, 2014, **9**, 1–8.
34   B. Mavis and M. Akinc, *Chem. Mater.* **2006**, *18*, 5317-5325.
35   L. Sun, L. Wang, C. Tian, T. Tan, Y. Xie, K. Shi, M. Li and H. Fu, *RSC Adv.*, 2012, **2**, 4498–4506.
36   Y. Han, S. Axnanda, E. J. Crumlin, R. Chang, B. Mao, Z. Hussain, P. N. Ross, Y. Li and Z. Liu, *J. Phys. Chem. B*, 2018, **122**, 666–671.
37   P. Bazylewski, D. W. Boukhvalov, A. I. Kukharenko, E. Z. Kurmaev, A. Hunt, A. Moewes, Y. H. Lee, S. O. Cholakh and G. S. Chang, *RSC Adv.* 2015, **5**, 75600-75606.

38   C. S. Maldonado, J. R. De la Rosa, C. J. Lucio-Ortiz, A. Hernández-Ramírez, F. F. Castillón Barraza and J. S. Valente, *Materials (Basel).*, 2014, **7**, 2062–2086.

39   X-ray   Photoelectron   Spectroscopy   (XPS)   Reference   Pages: Aluminum, http://www.xpsfitting.com/2008/09/aluminum.html, (accessed 7 August 2019).

40   A. Nadeema, P. S. Walko, R. N. Devi and S. Kurungot, *ACS Appl. Energy Mater.*, 2018, **1**, 5500–5510.

41   P. de S. Santos, A. C. V. Coelho, H. de S. Santos and P. K. Kiyohara, *Mater. Res.*, 2010, **12**, 437–445.

42   Z. Zafar, Z. H. Ni, X. Wu, Z. X. Shi, H. Y. Nan, J. Bai and L. T. Sun, *Carbon N. Y.*, 2013, **61**, 57–62.

43   M. Zeng and Y. Li, *J. Mater. Chem. A*, 2015, **3**, 14942–14962.

Chapter 6

Summary and Future Prospects

This chapter summarizes the significant observations and outcomes of the each working chapter of the present thesis. The chapter starts with a brief introductory paragraph of the work focus along with the strategy which we have adopted to align all the working chapters. Afterward, a brief overview and key points of all the working chapters are summed up one by one. The last part is dedicated to the future scope of the ideas and approach adopted in this dissertation toward the other electrochemical systems, for example, CO_2 reduction reaction, H_2O_2 production reaction, batteries and fuel cells.

6.1. Summary of the working chapters

The primary target of this dissertation is to develop various synthesis protocols and strategies to tune the electrocatalytic properties of layered double hydroxides (LDHs). This thesis also adopted various possible strategies to generate energy-efficient hydrogen from water. This dissertation begins with the introductory overview of the current status of hydrogen economy and the importance of LDHs toward one of the promising electrochemical device. Thesis is then followed by 4 working chapters. The major accomplishments in all the working chapters can be summarized as follows:

6.1.1. ϒ-NiOOH-Enriched NiZn Double Hydroxide Nanosheets/Nitrogen-Doped Graphene Composite for Catalysing the Water Oxidation Half-Cell

This working chapter focuses on catalyzing only the water oxidation half-cell (WOR) since the overall energy efficiency of water-sourced H_2 generation is controlled by WOR. This work contributes in replacing the high-cost Ir/Ru-based electrocatalysts with a low-cost earth-abundant material. The catalyst designing involved a single-pot solvothermal synthesis of thin-layered WOR-active ϒ-NiOOH enriched NiZn-LDHs anchored over N-doped graphene (NiZn-LDH/NGr). The LDH formation, it's anchoring as well as final loading over NGr was characterized well with the help of XRD, Raman, BET and TGA. The morphological

investigations were performed through FESEM and TEM analyses. The surface chemical state and bonding structure of the designed catalyst were thoroughly studied with the help of detailed XPS analysis. Finally, the catalytic activity of the designed material was investigated through a set of electrochemical techniques including, CV, LSV, chronoamperometry, *etc.* The designed catalyst required a mere 290 mV overpotential to reach 10 mA cm^{-2} with a small Tafel slope of 44 mV decade^{-1}, surpassing the commercial catalyst performance.

6.1.2. NiZn Double Hydroxide-Derived Nickel Selenide/Nitrogen-Doped Graphene Composite to Catalyze the Overall Water Electrolysis

Water electrolysis involves two half-cell reactions, *i.e.*, water oxidation reaction (WOR) and hydrogen evolution reaction (HER). Being kinetically sluggish, both the reactions require robust catalyst to improve the energy-efficiency of the H$_2$ generation process. In spite of designing two different materials for catalyzing the two half-cell reactions, designing of a bifunctional catalyst can further save both the cost as well as time. Hence, the targeted goal of this chapter is to contribute in replacing the high-cost Pt/Ru/Ir-based catalysts with a bifunctional catalyst system based on readily available low-cost metals. The work adopts a self-templating approach for the designing of porous, edge-site-rich hybrid nanomaterial *via* the selective etching of layered double hydroxide precursors that contain an amphoteric metal by alkali treatment followed by vapour phase selenization. The formation of p-NiSe/NGr was first confirmed through XRD. The porosity generated in the material after selective Zn etching was confirmed through BET pore-size distribution analysis. Thorough morphological investigations were performed through FESEM and TEM analyses, presenting hexagonal patches of nickel selenides over NGr. After the extensive material characterizations, the catalyst was taken for electrochemical analysis in N$_2$ saturated 1 M KOH. Toward WOR, the catalyst demonstrated a low overpotential of ~311 mV to achieve the benchmark 10 mA cm^{-2} water oxidation current density. The as-designed catalyst with monoclinic Ni$_{1-x}$Se phase along with the traces of NiO$_x$ and elemental selenium was also employed for catalyzing HER, where our catalyst showed only 276 mV voltage shift from commercial catalyst to reach the benchmark 10 mA cm^{-2} in 1 M KOH. By employing p-NiSe/NGr both as a cathode and anode, when an alkaline water electrolyzer was fabricated, it enabled a high-performing overall water splitting with a low overpotential of 460 mV from the theoretical voltage of 1.23 V to generate sufficient amounts of H$_2$ and O$_2$ by achieving a current

density of 10 mA cm^{-2}. Interestingly, our catalyst performed equally efficiently to the commercial catalyst-based water electrolyzer, illustrating its industrial importance. Moreover, the designed catalyst has displayed outstanding electrochemical stability toward all the employed reactions which are found to be far better than the commercial catalyst in 1 M KOH.

6.1.3. $[MoS_4]^{2-}$-Intercalated NiCo Layered Double Hydroxide Nanospikes/Ni Foam to Generate Cheaper H$_2$ Directly from Urea-Rich Wastewater

With this chapter our aim was to further improve the energy-efficiency of the H$_2$ generation process, and hence to contribute toward reducing the per kg H$_2$ cost. For improving the energy-efficiency, this chapter describes a strategy of substituting the energy-uphill water oxidation half-cell with readily oxidizable waste urea. Considering this, the strategy is also extended with urea-enriched real urine to construct a ground-breaking bridge, combining the energy-efficient hydrogen generation and environmental protection. However, for realizing this approach, the designing of a robust multifunctional electrocatalyst was indeed essential. In this context, here, we proposed a simple tuning of the electrocatalytically favorable characteristics of NiCo LDH by introducing $[MoS_4]^{2-}$ in its interlayer space. The $[MoS_4]^{2-}$ insertion induced overall electronic structure tuning of the hydroxide layers in such a way that, the designed catalyst exhibited favorable kinetics toward all the required reactions of hydrogen generation. The NiCo LDH growth over Ni foam as well as $[MoS_4]^{2-}$ interslab insertion (MoS$_4$-LDH/NF) was extensively characterized with the help of XRD, FTIR, FESEM, TEM and XPS. The NF-supported catalyst was then utilized for various electrochemical analyses. For urea oxidation, the designed catalyst required only 1.34 V *vs*. RHE to reach the benchmark 10 mA cm^{-2}. For HER, the catalyst required a mere 91 mV overpotential *w.r.t.* commercial Pt/C catalyst to reach the 10 mA cm^{-2}. Finally, we employed MoS$_4$-LDH/NF both as the cathode and anode to construct a two-electrode electrolyzer taking 0.33 M synthetic urea in 1 M KOH. As compared to the commercial catalyst-based urea electrolyzer (~1.48 V), the MoS$_4$-LDH/NF-based electrolyzer required only ~1.37 V voltage to achieve the benchmark current density of 10 mA cm^{-2}. When employed real urine with 1 M KOH, our homemade electrolyzer showed a mere 70 mV overpotential from urea electrolysis (1.44 V cell voltage) to deliver 10 mA cm^{-2}. Along with excellent activity, the designed catalyst exhibited outstanding stability toward all the required reactions even with real urine.

6.1.4. Co@CoAl-LDH/NGr-Catalysed Dual-Mode Al-Based Battery for Low-Cost H_2 Production and Electricity Generation

With this work, our aim was not only to replace the energy-consuming water oxidation with readily oxidizable species but also to generate electricity. The motivation of the work was built from a novel method of hydrogen production *via* a self-sustained reaction between activated aluminum powder and water, as-proposed by Prof. Alon Gany and co-workers. Here, they mentioned about the "energy bonus" of 17 kJ per gram of Al during the exothermic (Al + 3H_2O $\rightarrow$ Al(OH)$_3$ + 3/2 H_2) reaction. Thus, this energy bonus can be harvested simply by separating the involved reaction through the electrochemistry into two half-cell reactions. Hence, in this chapter, we proposed the fabrication and demonstration of a dual-mode Al-based battery to generate H_2 and electricity simultaneously. Here, the logic of demonstrating a dual-mode battery is to validate our as-proposed concept of Al-H_2O fuel cell. However, to improve the overall energy-efficiency of the device, development of a robust bifunctional catalyst was required, which can catalyze both O_2 reduction reaction (ORR) as well as H_2O reduction (hydrogen evolution reaction, HER). In this context, we believed that the designing of Co@CoAl-LDH nanostructures, having metallic Co-rich core and LDH-enriched shell, engraved in N-doped graphene (NG) can act as a robust HER electrocatalyst. Besides HER, the fine architectural designing of the electronically-rich metallic core and Al-enriched hydroxide shell is believed to bestow good ORR activity. The catalyst (Co@CoAl/NG) was synthesized by adopting a single-step hydrothermal process at 180 ^{o}C for 12 h. The synthesized material was characterized well with the help of FESEM, TEM, HRTEM, XPS and XRD. After thorough material characterizations, the catalyst was taken for electrochemical analysis. In 1 M KOH, as compared to the commercial Pt/C, our catalyst required only 113 mV overpotential to reach the benchmark current density of 10 mA cm^{-2} along with ~80% catalytic activity retention after 12 h of continuous performance evaluation. Toward ORR, as compared to the commercial catalyst, our homemade catalyst showed a mere ~40 mV overpotential shift in the half-wave potential ($E_{1/2}$, voltage at the half of the total kinetic current) region, illustrating good ORR catalytic activity. The designed catalyst when employed as the cathode in dual-mode Al-based battery both in presence and absence of O_2, it worked quite efficiently and performed comparable to the similar devices based on the commercial Pt-based catalyst. At a discharge current density of 5 mA cm^{-2}, the catalyst exhibited an average voltage of ~0.95 V both in presence and absence of O_2.

6.2. Future prospects

The present dissertation has wide potential impact in both the fundamentals as well as applied research in various electrochemical energy conversions owing to the unique physicochemical property tuning of the materials and methodologies employed during the PhD tenure. Based on the aforementioned key aspects of the work carried out, it can be seen that the knowledge gained covers a vast area ranging from nanomaterials synthesis to the learning of extensive material characterization techniques to the structure-property tuning of materials for various electrocatalytic applications. Major focus of the present thesis includes the physicochemical property tuning of the layered double hydroxides for catalyzing various electrochemical reactions involved in the energy-efficient hydrogen generation.

Though the presented research activities are restricted on the electrochemical hydrogen generation, the knowledge gained during the research tenure can be employed for various other emerging electrochemical conversions of interest, e.g., CO_2 reduction reaction, H_2O_2 production reaction, N_2 reduction reaction etc. In addition to this, the LDHs tunings can also be extended on designing bifunctional catalysts for oxygen reduction reaction and oxygen evolution reaction which are the key reactions for rechargeable metal-air batteries.

As discussed in the Section 1.9. of Chapter 1, LDHs provide a wide scope of their property tuning which can be further explored in designing robust electrocatalysts. Apart from this, owing to its tunable interlayer space, the experience gained during the PhD tenure for the LDH property tuning can also be taken for developing charge storage materials for various electrochemical energy devices, e.g., supercapacitors and metal-ion batteries.

List of Publications

1. Vishal Mahesh Dhavale[#], Santosh K Singh[#], **Ayasha Nadeema[#]**, Sachin S Gaikwad And Sreekumar Kurungot, *Nanocrystalline Fe-Fe₂O₃ Particle-Deposited N-doped Graphene as an Activity Modulated Pt-Free Electrocatalyst for Oxygen Reduction Reaction*, *Nanoscale*, **2015**, *7*, 20117 – 20125. **(# these authors contributed equally)**

2. **Ayasha Nadeema**, Vishal M. Dhavale, and Sreekumar Kurungot, *NiZn Double Hydroxide Nanosheet-Anchored Nitrogen-doped Graphene Enriched with ϒ-NiOOH Phase as an Activity Modulated Water Oxidation Electrocatalyst*, *Nanoscale*, **2017**, *9*, 12590 - 12600.

3. **Ayasha Nadeema**, Priyanka S. Walko, R. Nandini Devi, *and* Sreekumar Kurungot, *Alkaline Water Electrolysis by NiZn Double Hydroxide-Derived Porous Nickel Selenide/Nitrogen-doped graphene composite*, *ACS Appl. Energy Mater.* **2018**, *1,* 5500–5510.

4. **Ayasha Nadeema**, Varchaswal Kashyap, Rakshitha Gururaj, and Sreekumar Kurungot; *[MoS₄]²⁻-Intercalated NiCo Layered Double Hydroxide Nanospikes: An Efficiently Synergized Material for Urine to Direct H₂ Generation*, *ACS Appl. Mater. Interfaces* **2019**, *11*, 25917-25927.

5. Shilpa Nagaraju, **Ayasha Nadeema**, Sreekumar Kurungot**,** *Glycine Induced Electrodeposition of Nanostructured Cobalt Hydroxide: A Bifunctional Catalyst for Overall Water-Splitting*, **Under Revision.**

6. **Ayasha Nadeema**, Geeta Pandurang Kharabe, Dibya Prakash Biswal, and Sreekumar Kurungot, *Co@CoAl-LDH/NG composite-Catalyzed Dual-Mode Al-Based Battery for Simultaneous H₂ Production and Electricity Generation*, **Communicated.**

7. Narugopal Manna, **Ayasha Nadeema,** Santosh k. Singh, Sreekumar Kurungot, *NiFe Layered double hydroxide-Decorated N-Doped Entangled-Graphene Framework: A Robust Water Oxidation Electrocatalyst,* **Communicated.**

Erratum